Dynamics of driven optomechanical systems near the semiclassical limit

I n a u g u r a l d i s s e r t a t i o n

zur

Erlangung des akademischen Grades eines

Doktors der Naturwissenschaften
(Dr. rer. nat.)

der

Mathematisch-Naturwissenschaftlichen Fakultät

der

Universität Greifswald

vorgelegt von

Christian Wurl (geb. Schulz)

geboren am 26. Oktober 1989

in Neubrandenburg

Greifswald, 10. Dezember 2018

Dekan:	Prof. Dr. Werner Weitschies
1. Gutachter:	Prof. Dr. Holger Fehske
2. Gutachter:	Prof. Dr. Martin Holthaus
Tag der Disputation:	12. April 2019

Contents

1 Summary

1.1 Introduction

Optomechanical systems describe the interaction between light and matter. The generic model of cavity optomechanics is a light field in a cavity that consists of a fixed mirror and a mechanical oscillator [1]. In the standard Hamiltonian description a single quantized mode of the electromagnetic field is coupled via radiation pressure to the vibrational mode of the mechanical oscillator [2, 3]. Radiation pressure causes a displacement of the oscillator, but the position of the oscillator also determines the radiation pressure force. Thus, in the equations of motion the light-matter interaction appears as a nonlinear term which is responsible for the unique dynamical properties of optomechanical systems [4].
The realistic description of optomechanical systems requires a consideration of the environment. Even when the temperature is assumed to be zero, that is, when classical thermal fluctuations are neglected, quantum entanglement with the environment has a significant impact on the dynamical properties of the system. This is especially true for the photon field, for which a sufficiently high dissipation rate causes decoherence. The system is forced into a classical mixed ensemble such that classical signatures that are hidden in the isolated quantum system become visible in the open quantum system [5–7]. On the other hand, the nonlinear optomechanical interaction induces fluctuations around the classical steady state of the photon field [8]. Near the semiclassical limit, the quantum dynamics can therefore be considered as fluctuations which occur in the linearized equations of motion as deviations from classical expectation values [1].
Driving the system enhances the radiation pressure force so that the light-matter interaction is parametrized by an effective optomechanical coupling tunable by the laser power, instead of the bare single photon-phonon coupling. The other optomechanical parameters can be adjusted over a wide range due to the almost arbitrary dimensioning of the building components. Therefore, optomechanical systems are of great interest since they allow the investigation and experimental detection of a variety of quantum and classical phenomena on both the microscopic and the macroscopic scale [9, 10]. Examples of experimental realizations in terms of the single optomechanical cell are a cavity with an oscillating mirror, the membrane-in-the-middle setup, microtoroids, or electromechanical implementations using superconducting circuits. Depending on the detuning between laser frequency and cavity resonance frequency, different dynamical effects have been detected, including non-demolution measurements [11–13], quantum ground state cooling [14–16], micro-macro entanglement [17–19], the generation of non-classical states such as squeezed light [20–22] or Schrödinger-cat states [23, 24], nonlinear multistability effects and self-sustained oscillations for the cavity-cantilever-setup [25–32] and for the membrane-in-the-middle-setup [33–39], as well as coherent state transfer between photons and phonons [40–44].
Of particular importance in the context of the latter are coupled optomechanical sys-

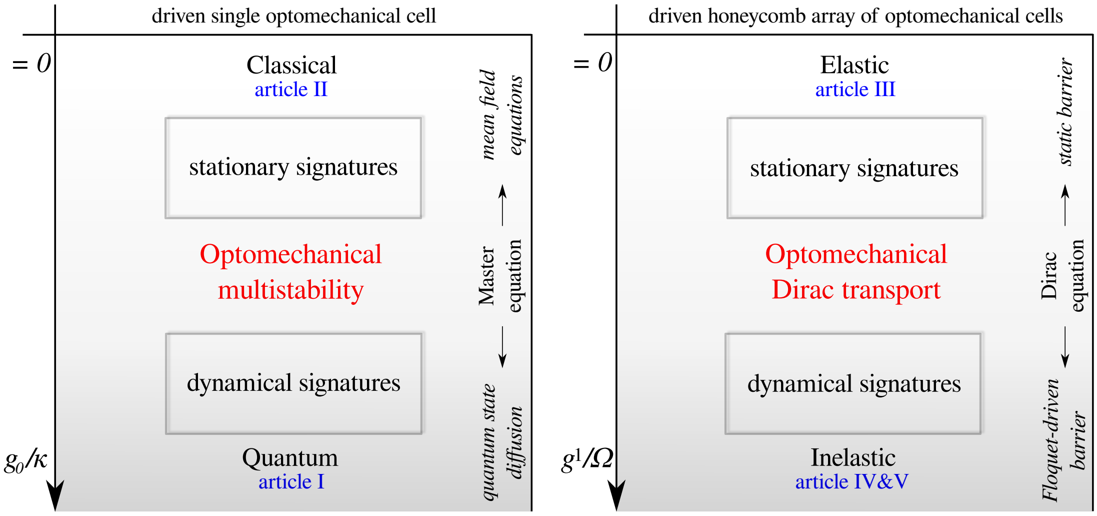

Fig. 1: Illustration of the two aspects studied in this thesis (colored red) and applied methods. For the single optomechanical cell the bare photon-phonon-coupling g_0 (photon dissipation $\sim \kappa$) determines the transition from classical to quantum multistability. For the honeycomb array of optomechanical cells the periodically oscillating part g^1 (frequency Ω) in the laser-driven effective optomechanical coupling determines the transition from elastic to inelastic Dirac transport.

tems such as artificial optomechanical arrays, that are setups composed of several periodically arranged optomechanical cells [45–48]. The dynamical multi-mode effects that occur here allow insight into new (quantum) phenomena at a macroscopic level and can be utilized for transport, storage, processing and conversion of optical and mechanical collective excitations [49–60], as well as creation of classical gauge fields [61–63] and topological effects [64]. Planar metamaterials are of particular interest because of their special, in-situ optically tunable band structure and the ease of optical control. One of these metamaterials is optomechanical graphene. Here, low-energy photons and phonons can be described within the linearized semiclassical regime by an optomechanical Dirac-Weyl Hamiltonian, which is similar to that for electrons in graphene [65]. The crucial difference is the photon-phonon coupling inside the barrier. In addition to ultrarelativistic transport phenomena such as Klein tunneling, the formation of polariton states may cause the interconversion between light and sound. Furthermore, as demonstrated for the photon-assisted electron transport in graphene-based nanostructures [66], time-dependent external fields produce new effects which are also relevant for fundamental problems such as *zitterbewegung* [67–71]. Due to the energy sensitivity of the transport phenomena, driven optomechanical barriers in optomechanical graphene should have a significant impact, too. In this context circular barriers are of special interest as they allow for a richer scattering behaviour due to their finite size [72–75].

The first part of this thesis deals with the dynamics of a single driven optomechanical cell and focuses on multistability effects in the classical and in the quantum regime, see Fig. 1 (left). This work was motivated by the possibility to detect the quantum-to-classical crossover directly in the dynamical behaviour of optomechanical systems near the semiclassical limit [30, 32]. The crossover is controlled via the quantum parameter, which is defined as the ratio of single photon-phonon coupling to photon dissipation, g_0/κ. A clear classical picture is required, so first the dynamics in the classical limit is studied where classical multistability is characterized by stationary signatures. For studying the dynamics in the quantum regime the quantum-optical master equation is solved numerically. We discuss whether and how classical multistability is manifested in the quantum regime, where new dynamical patterns appear because quantum trajectories can move between classical attractors due to fluctuation induced instabilities. To follow the transition from quantum mechanics to classical mechanics, we employ phase space techniques such as Wigner and autocorrelation functions.

The second part of this thesis deals with the driven elastic and inelastic transport of Dirac quasiparticles, propagating as light and sound waves on a honeycomb array of optomechanical cells (optomechanical graphene), see Fig. 1 (right). This work was motivated by the various ultrarelativistic transport phenomena for electrons in graphene [76–80], which occur in optomechanical graphene in a new manner due to the additional optomechanical degree of freedom. Within an effective Dirac-Weyl theory, we study the scattering/tunneling of a plane photon wave by/through laser-induced photon-phonon coupling planar and circular barriers. First, the energy-conserved (elastic) case of static barriers is investigated. Analyzing the stationary scattering regimes in dependence of the system parameters we discuss how the phonon-affected transport in the barrier determines the scattering behaviour. Then, considering finite values of the time-dependent part of the coupling strength ($g^1/\Omega > 0$), the non-energy-conserved (inelastic) case of periodically oscillating barriers is studied. The related time-dependent scattering problem is solved using Floquet theory for an effective two-level system. We discuss the importance of avoided crossings in the quasienergy bands, which occur due to the optomechanical degeneration. Furthermore, we investigate the role of sideband states and their interference for the new dynamical signatures that occur there.

1.2 Optomechanical multistability

Our goal is to detect the quantum-to-classical crossover in the dynamics of the single optomechanical cell, which is characterized by multistability effects. After introducing the Hamiltonian description, we explain how the quantum-to-classical transition can be realized via the quantum parameter that enters the rescaled equations of motion. Based on these equations, the classical dynamics is analyzed for the membrane-in-the-middle setup (article II). Then, the quantum dynamics is investigated for the simpler cavity-cantilever setup (article I).

Hamiltonian description The isolated optomechanical cell, see Fig. 2, is described by the Hamiltonian [1–3] $H/\hbar = H_0 + H_{int} + H_{ext}$ where

$$H_0 = -\Delta \left(a_L^\dagger a_L + a_R^\dagger a_R \right) + \Omega_m b^\dagger b, \tag{1a}$$

$$H_{int} = g_0 (b^\dagger + b)(a_L^\dagger a_L - a_R^\dagger a_R) - J(a_L^\dagger a_R + a_L a_R^\dagger), \tag{1b}$$

$$H_{ext} = \alpha(a_L + a_L^\dagger) + \mathrm{e}^{i\varphi}\alpha(a_R + a_R^\dagger). \tag{1c}$$

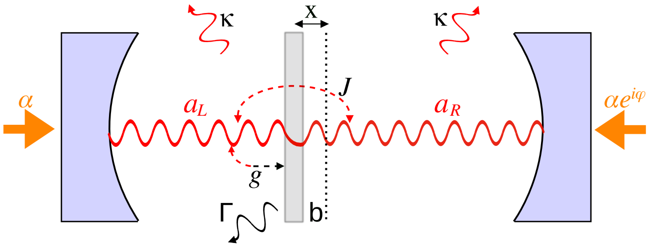

Fig. 2: Membrane-in-the-middle (cavity-cantilever) setup. A vibrating cantilever with transmissivity $\propto J$ ($J = 0$) is subjected to the cavity photon field via radiation pressure $\propto g_0$. The system is driven from both sides (left side).

Here b and $a_{L/R}$ are bosonic operators for the cantilever (frequency Ω_m) and for the left/right cavity photon field (frequency Ω_c), respectively. The radiation pressure induced interaction is parametrized by the bare single-photon coupling rate $g_0 = Gx_{zpf}$, where $G = \Omega_c/(L/2)$ (L is the length of the whole cavity) and $x_{zpf} = \sqrt{\hbar/2m\Omega_m}$ is the zero-point fluctuation of the membrane with effective mass m. In the case of the membrane-in-the-middle setup the transmissivity of the membrane is taken into account by a finite photon tunneling probability $\sim J$ [50, 81–83]. The simpler cavity-cantilever setup is obtained formally by setting $J = a_R \equiv 0$ in the Hamiltonian, cf. Fig. 2. Note that the Hamiltonian is written in the rotating frame of the external pump laser (amplitude α, phase shift $\varphi = \pi$) so that only the detuning $\Delta = \Omega_l - \Omega_c$ appears (Ω_l denotes the frequency of the laser). Our theoretical analysis is based on the quantum-optical master equation [84]

$$\dot{\rho} = -\frac{i}{\hbar}[H, \rho] + 2\Gamma\mathcal{D}[b, \rho] + 2\kappa \sum_{L/R} \mathcal{D}\left[a_{L/R}, \rho\right], \tag{2}$$

from which we obtain the time evolution of the cavity-cantilever density matrix $\rho(t)$. The environment is taken into account by the dissipative terms $\mathcal{D}[L, \rho] = L\rho L^\dagger - \frac{1}{2}(L^\dagger L\rho + \rho L^\dagger L)$ which describe cantilever damping ($\propto \Gamma$) and radiation losses ($\propto \kappa$). We neglect thermal fluctuations, i.e., the temperature is assumed to be zero.

Quantum-to-classical transition From eq. (2) we obtain the equations of motion for the expectation values

$$\frac{\mathrm{d}}{\mathrm{d}t}\langle a_L\rangle = i\Delta\langle a_L\rangle - ig_0\langle(b^\dagger + b)a_L\rangle - \kappa\langle a_L\rangle - iJ\langle a_R\rangle - i\alpha, \tag{3a}$$

$$\frac{\mathrm{d}}{\mathrm{d}t}\langle a_R\rangle = i\Delta\langle a_R\rangle + ig_0\langle(b^\dagger + b)a_R\rangle - \kappa\langle a_R\rangle - iJ\langle a_L\rangle - \mathrm{e}^{i\varphi}i\alpha, \tag{3b}$$

$$\frac{\mathrm{d}}{\mathrm{d}t}\langle b\rangle = -i\Omega\langle b\rangle - ig_0\langle a_L^\dagger a_L - a_R^\dagger a_R\rangle - \Gamma\langle b\rangle. \tag{3c}$$

The cantilever phase space variables are given as $x = x_{zpf}(b^\dagger + b)$ and $p = p_{zpf}i(b^\dagger - b)$, where $p_{zpf} = \sqrt{\hbar m\Omega_m/2}$ is the zero-point fluctuation of the momentum. The interaction terms in eqs. (3) scale with $g_0 = Gx_{zpf} \sim \sqrt{\hbar}$ and contain quantum correlations. We explain under which conditions such correlations can be neglected, i.e., when $\langle ab\rangle = \langle a\rangle\langle b\rangle$ (mean field). This leads to the quantum-to-classical transition.
If one considers the equations of motion (3) as force equations of the type $\mathrm{d}^2\langle\boldsymbol{\xi}\rangle/\mathrm{d}t^2 = \langle\boldsymbol{F}(\boldsymbol{\xi})\rangle$ (the components ξ_i are the generalized coordinates of the system and F_i the corresponding forces), then the classical equations apply to their expectation values [85].

But $\langle \boldsymbol{F}(\boldsymbol{\xi})\rangle = \boldsymbol{F}(\langle\boldsymbol{\xi}\rangle)$ (mean field) only applies if quantum correlations are negligible. To estimate their influence we expand the force around the expectation value $\langle\boldsymbol{\xi}\rangle$,

$$\langle F_i(\boldsymbol{\xi})\rangle = F_i(\langle\boldsymbol{\xi}\rangle) + \frac{1}{2}\sum_{j,l}\frac{\partial^2 F_i(\langle\boldsymbol{\xi}\rangle)}{\partial\xi_j\partial\xi_l}\langle(\xi_j - \langle\xi_j\rangle)(\xi_l - \langle\xi_l\rangle)\rangle + \dots . \tag{4}$$

For forces that depend linearly on ξ_i (harmonic oscillator) the correction terms disappear. Then, the semiclassical equations of motion are automatically fulfilled, in particular coherent states remain coherent. However, the nonlinear correlation terms in the eqs. (3) are of higher order and lead to quantum corrections which are determined by the size of the Heisenberg uncertainty (variances). Thus, the quantum nature consists on the one hand of the general uncertainty of the state and, on the other hand, of quantum corrections determined by the uncertainty.
In the classical limit the Heisenberg uncertainty must go to zero, since only then quantum corrections disappear. To realize this, we introduce dimensionless quantities, i.e., we measure time as $\tau = t\cdot\Omega$ and rescale the system parameters according to $(\Delta,\kappa,\Gamma)\to(\Delta,\kappa,\Gamma)/\Omega_m$, $J\to \mathrm{e}^{i\varphi}J/\Omega_m$. The field amplitudes are rescaled according to $b\to(g_0/\Omega_m)\cdot b$ and $a\to(\Omega_m/\alpha)\cdot a$. Now, the quantum correction terms in eq. (4) are determined by rescaled variances. They vanish for $g_0\to 0$ and $\alpha\propto 1/g_0\to\infty$, because then the width of the states in phase space approaches the delta peak. At the same time, the parametrization of the nonlinear interaction in eq. (3) remains constant because it is now given by the combined size $P = g_0^2\alpha^2/\Omega_m^4$ (proportional to the pump power). Thereby, the classical dynamics does not change under this rescaling and the quantum-to-classical transition is formally equivalent to decreasing Planck‘s constant, $\hbar\to 0$, making it possible to study the influence of quantum effects.
In this context optical dissipation plays an important role as it leads to the attenuation of quantum effects. As a result, quantum corrections in eq. (4) are small for the photon field (justifying its linearized equations of motion) and the system is close to the semiclassical limit (for a more detailed explanation see chapter quantum multistability). For this reason, instead of g_0 only, it is usual to employ the dimensionless quantum parameter $\sigma = g_0/\kappa$ [1, 30, 32]. For our purposes we fix $\kappa = 1$ ($\Gamma = 0.001$) and vary g_0 only.

Classical multistability In the classical limit $\sigma = 0$, the mean field equations apply (we omit the brackets $\langle\cdot\rangle$ for the expectation values). Classical multistability is characterized by stationary solutions, that are, attractors or repulsors, reaching from simple fixed points to more complicated nonlinear signatures on the route to chaos. We discuss them in dependence on the pump power P and the detuning Δ, where we focus on the cantilever motion. Special attention is paid to self-sustained oscillations.

The system reveals a reflection symmetry $x\to -x$ with $p\to -p$ and $a_{L/R}\to a_{R/L}$, which implies the existence of a trivial fixed point $x_0 = 0$. Increasing the pump power P leads to a symmetry breaking through the occurence of further fixed points $\pm x_i$ which are defined as the static solutions of (3), see Fig. 3 (a) and (b) [eqs. (2)-(5) in article II]. These non-trivial fixed points appear through supercritical (a) and subcritical (b) pitchfork bifurcations with the latter being accompanied by a saddle-node bifurcation (for a global plot see Fig. 3 in article II). Changes in the stability of the fixed points

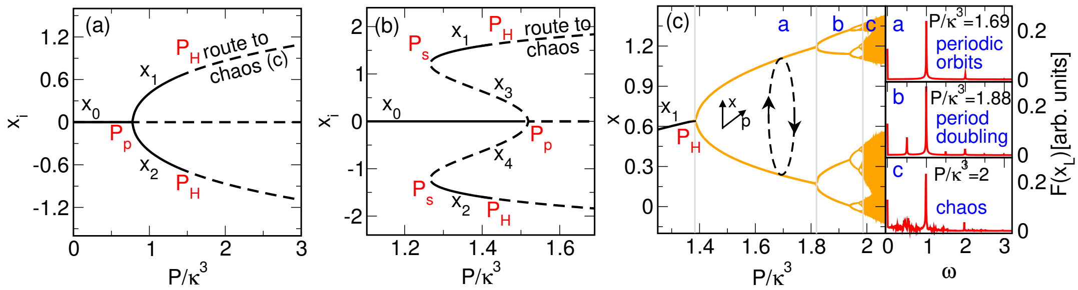

Fig. 3: Fixed points in dependence on the pump power P with (a) supercritical ($\Delta/\kappa = 0$), (b) subcritical ($\Delta/\kappa = -1.65$) pitchfork bifurcation (P_p) for $J/\kappa = -0.5$, together with saddle-node bifurcation (P_s) and Hopf bifurcations (P_H). Solid (dashed) curves denote stable (unstable) fixed points. Panel (c): route to chaos in the Feigenbaum diagram starting at the upper fixed point after the supercritical pitchfork bifurcation in panel (a), and optical spectrum of the left photon mode.

occur according to the bifurcation type, which implies hysteresis for case (b). The fixed point bifurcations and stability characteristics can also be obtained in dependence on detuning Δ, where new patterns like a 'boomerang' appear (Figs. 3, 10 in article II). If the pump power P (or detuning $|\Delta|$) is further increased, Hopf bifurcations occur and lead to the instability of the fixed points $x_{1,2}$. Within linear stability analysis [Jacobi matrix is given by eqs. (B2),(B3) of article II] Hopf bifurcations are manifested by the transition of two complex eigenvalues of the Jacobian matrix from the negative to the positive real numbers (Fig. 4 in article II). As a result, self-sustained periodic oscillations occur with a frequency given by the imaginary part of the complex eigenvalue pair. A further increase of the pumping leads to period-doubling bifurcations and finally to chaos. The different dynamical regimes of the mechanical mode are illustrated in the Feigenbaum diagram in Fig. 3 (c) and are also reflected in the optical spectrum. The analysis of oscillations for finite amplitudes away from the Hopf bifurcation requires a description that goes beyond linear stability analysis. For this, a simple periodic oscillation of the cantilever is assumed,

$$x(t) = x_c + A\cos\omega t, \tag{5}$$

taking into account that the frequency of the oscillation does not have to match the natural frequency of the cantilever. To determine the parameters x_c, A and ω we insert the ansatz (5) in the equations of motion (3c), which yields the conditions

$$x_c = -P\sum_m |a_L^m|^2 - |a_R^m|^2, \tag{6a}$$

$$\Gamma\omega A = -2P\,\mathrm{Im}\left\{\sum_m a_L^{m*}a_L^{m-1} - a_R^{m*}a_R^{m-1}\right\}, \tag{6b}$$

$$A(1-\omega^2) = -2P\,\mathrm{Re}\left\{\sum_m a_L^{m*}a_L^{m-1} - a_R^{m*}a_R^{m-1}\right\}. \tag{6c}$$

Here we have exploited that the cantilever oscillation leads to the excitation of sidebands of the photon field at integer multiples of the frequency ω. Hence, the photon fields

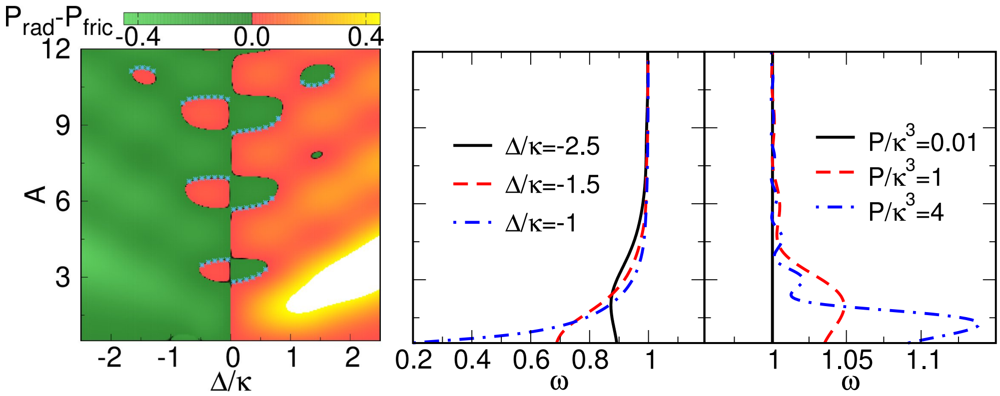

Fig. 4: Left panel: power balance $\mathcal{P}_{rad} - \mathcal{P}_{fric}$ as a function of A and Δ/κ for $P/\kappa^3 = 1$. The stable periodic orbits obtained from numerics are dotted blue. Right panels: oscillation frequency ω calculated from the selfconsistend eqs. (6) as a function of A for different Δ/κ (P/κ^3) at $P/\kappa^3 = 1$ $(\Delta/\kappa = 0.5)$. In all panels $J/\kappa = 0$.

also reveal a periodic motion, $a_{L/R}(t) = \exp\left(\mp i(A/\omega)\sin\omega t\right)\sum_{n=-\infty}^{\infty} a^n_{L/R}\exp(in\omega t)$, where the Fourier components $a^n_{L/R}$ must be determined by the equations of motion (3a) and (3b) self-consistently [eqs. (8) in article II]. For small values of J this can be done iteratively. The self-sustained oscillations after the Hopf bifurcation are correctly predicted within this approach (see Fig. 8 in article II).

The eqs. (6) allow for a simple physical interpretation. They imply that for a harmonic cantilever-oscillation on average over time, (a) the force acting on the oscillator, (b) the change in oscillator energy, and (c) the phase shift of the oscillation must vanish. Condition (b) can be written as a power balance $\mathcal{P} = \mathcal{P}_{rad} - \mathcal{P}_{fric} = 0$, where $\mathcal{P}_{rad} = -P\omega A \mathrm{Im}\{...\}$ is the mean energy gain due to radiation pressure and $\mathcal{P}_{fric} = \Gamma\omega^2 A^2/2$ is the mean energy loss due to friction [28,30,35]. Condition (c) determines the oscillation frequency, which in a simpler approach that is mostly used in literature agrees with the natural frequency of the cantilever, $\omega = \Omega_m$. However, for certain system parameters there may be significant deviations from the natural frequency, so the simpler approach would yield the wrong result for such a case (see Figs. 5, 8 in article II). In principle, this effect should be measurable in the optical spectrum.

Besides self-induced oscillations after the Hopf bifurcation, further periodic orbits may occur at larger amplitudes. These can be determined numerically via the self-consistent eqs. (6). By way of illustration we take a step back and represent the power balance $\mathcal{P}$ as a function of the amplitude A and detuning Δ, see the left panel in Fig. 4 (here $J = 0$; for $J \neq 0$ see Figs. 6, 7 in article II). In addition to the condition for periodic orbits $\mathcal{P} = 0$, for stability $\mathrm{d}\mathcal{P}/\mathrm{d}A < 0$ must be satisfied (otherwise friction forces would cause an unphysical increase of the amplitude). Our approach predicts the multistability of self-sustained oscillations, that is the coexistence of several stable periodic orbits with different amplitudes, in agreement with the numerically determined solutions. Again, the oscillation frequency of the orbits may deviate significantly from the natural cantilever frequency, see the right panels in Fig. 4. Obviously, a frequency renormalization is necessary to obtain the right solutions at smaller amplitudes, while at larger amplitudes the simpler approach with $\omega = \Omega_m$ is a good approximation.

Many of the classical signatures just discussed exist in a similar manner for the simpler cavity-cantilever setup. This applies especially to the classical multistability of self-sustained oscillations, which are the origin of the quantum multistability analyzed in the next section.

Quantum multistability For analyzing the dynamic behavior of the system in the quantum regime, we focus on the cantilever motion again. Therefore, we fix the parameters as $P = 3/16$ [$P = 1.5$ in article I, due to a different rescaling in eqs. (4),(5) there] and $\Delta = -0.4$. For these parameter values the classical cantilever dynamics features simple periodic orbits at amplitudes $A \approx 1.2$ und $A \approx 2.7$ (Fig. 1 in article I) with a frequency very close to Ω_m (thus no frequency renormalization is necessary).

We let σ become finite, but we keep $\sigma \ll 1$ in order to stay close to the semiclassical limit. Quantum correlations are now important and the master equation (2) must be solved without using the mean field approximation. This is done by means of the Quantum state diffusion method [86] which represents one possible unraveling of the master equation [6]. For this purpose, the density matrix $\rho(\tau)$ is represented by an ensemble of quantum trajectories $|\psi_k(\tau)\rangle$, each of which satisfies the nonlinear stochastic differential equation [87]

$$\begin{aligned} |\mathrm{d}\psi\rangle = \; & -\tfrac{i}{\hbar} H |\psi\rangle \,\mathrm{d}\tau + \sum_{m=1,2} \left(\langle L_m \rangle L_m - \frac{1}{2} L_m^\dagger L_m - \frac{1}{2} \langle L_m^\dagger \rangle \langle L_m \rangle \right) |\psi\rangle \,\mathrm{d}\tau \\ & + \sum_{m=1,2} \left(L_m - \langle L_m \rangle \right) |\psi\rangle \,\mathrm{d}\xi_m . \end{aligned} \tag{7}$$

Here, $H/\hbar$ is the Hamiltonian (1), $L_m \in \{\sqrt{2\kappa} a, \sqrt{2\Gamma} b\}$ are the Lindbladians of the cavity mode or the cantilever mode respectively, and $\mathrm{d}\xi_m$ are normalized, uncorrelated differential random complex numbers (Wiener increments). The temporal evolution of the density matrix results from the ensemble averaging $\rho(\tau) = \mathcal{M}_k(|\psi_k(\tau)\rangle \langle \psi_k(\tau)|)$, and expectation values from observables O are obtained according to $\mathcal{M}_k(\langle \psi_k(\tau)|O|\psi_k(\tau)\rangle)$. For the numerical treatment we use the implementation from ref. [88] and average about 3000 trajectories. Since we want to compare the classical with the quantum dynamics, the initial state is prepared as the state that is closest to the classical state, i.e., a pure product state from coherent cantilever and cavity states at $\langle a \rangle = \langle b \rangle = 0$ (brackets of the expectation values are omitted in what follows).
At the beginning, the position-momentum uncertainty product of the cantilever has the minimal value, but it takes on larger values when the system is evolved in time, see Fig. 5 (a). The increase of uncertainty is associated with the out-spreading of the phase space volume occupied by the cantilever state. As a result, the quantum dynamics of the cantilever initially follows the harmonic oscillation of the inner classical orbit, but deviates significantly from it at later times, see Fig. 5 (b) und (c).
To get an insight into the physical process the full phase space dynamics of the cantilever is displayed in Fig. 6 by means of the Wigner function [89]. Initially, almost all of the the phase space volume is weigthed on the inner classical orbit and is well localized. This explains why in Fig. 5 (b) the time evolution of the quantum expectation value is close to the classical one. Later, part of the phase space volume is transferred to

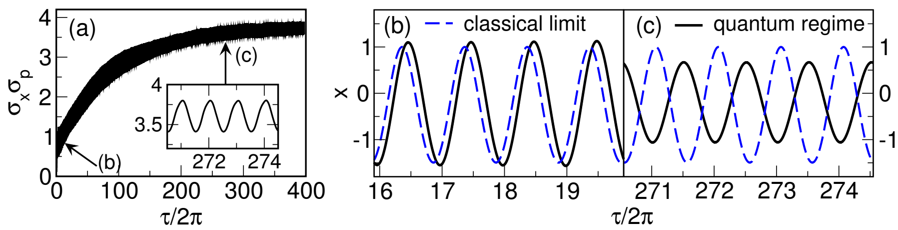

Fig. 5: Time evolution of (a) the cantilever uncertainty product $\sigma_x\sigma_p$ and (b/c) of the cantilever position in the classical limit $\sigma = 0$ (blue dashed curve) and in the quantum regime $\sigma = 0.1$ (black curve).

the second classical orbit until finally almost all of the weight lies on it. During the temporal evolution, the once localized state becomes delocalized and is spread out along the entire orbit, associated with the increase in the uncertainty product. The smaller the value of σ the larger the time scale on which this effect takes place (see Figs. 6, 7, 8 in article I).

Apparently, the classical multistability has a counterpart in the quantum regime, where quantum multistability appears as the dynamical spread out of the phase space volume on different classical periodic orbits. However, due to the delocalization of the phase space quasiprobability, a quantitative analysis or experimental observation of the effect can not be provided by means of simple expectation values, see Fig. 5 (c). Instead one can employ the cantilever position autocorrelation function

$$R_\tau\left(\delta\tau\right) = \int\limits_{\tau-\pi}^{\tau+\pi} \left\langle x\left(\tau'\right) x\left(\tau' + \delta\tau\right)\right\rangle \mathrm{d}\tau. \tag{8}$$

$R_\tau\left(\delta\tau\right)$ represents the weighted sum of the oscillatory motion on the classical orbits, where its amplitude indicates how the weight of the full phase space volume is distributed over the two orbits, see Fig. 6. For more details regarding the definition of the autocorrelation function see eqs. (9),(10) in article I and corresponding explanations.

For the interpretation of the results we analyze the properties of the single quantum trajectory, which itself is not measurable, but nevertheless provides insight into the physical behavior of the whole system. As can be seen from eq. (7), the temporal evolution of each quantum trajectory is determined on the one hand by the Hamiltonian and dissipative (coherent) dynamics (the first two terms), and on the other hand by the environment-induced white noise (last term). As explained in ref. [90], near the classical limit $\hbar \to 0$, for large enough disspation rates the noise term predominate and leads to a rapid localization of the trajectory in phase space (decoherence). However, the coherent state is not reached. If the trajectory has shrunk to a phase space volume close to its minimal Heisenberg uncertainty, the drift terms are of comparable magnitude and cause the opposite effect, namely delocalization in phase space. The dynamic interplay of these competing regimes results in fluctuations in the uncertainty product close to its minimal value. Due to their interaction, this holds not only for the photon but also for the phonon mode, $\sigma_x\sigma_p \gtrsim \frac{1}{2}(g_0/\Omega)^2 \sim \sigma^2$ (see Fig. 4 in article I), in spite of the relatively small damping loss of the membrane. In this context it becomes clear why the photon dissipation rate enters the quantum parameter g_0/κ: For larger values of κ

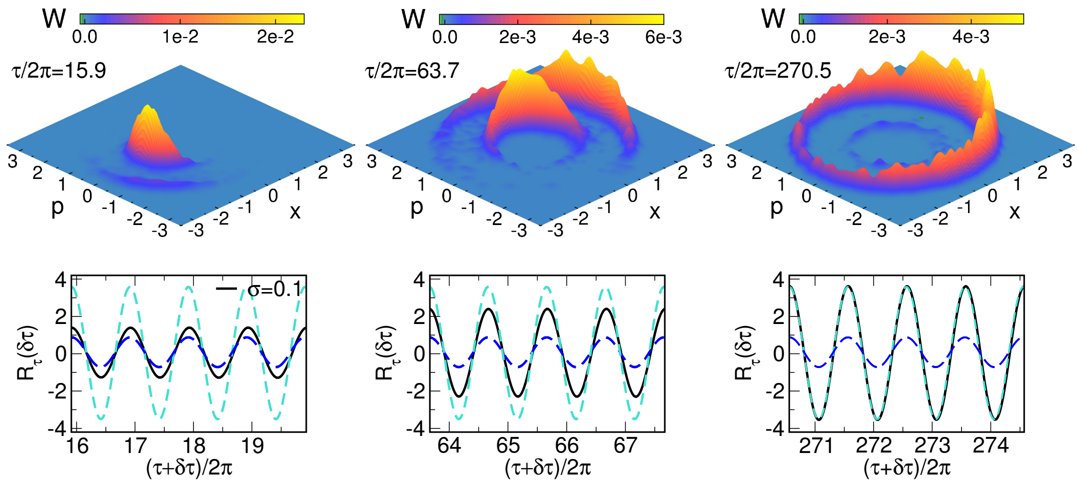

Fig. 6: Cantilever Wigner function $W(x, p)$ and position autocorrelation function according to eq. (8) at $\sigma = 0.1$; dashed curves: autocorrelation functions of the two classical orbits.

the localization effects are more pronounced than the delocalizations effects (that scales with $\sim g_0$), so the Heisenberg uncertainty product is closer to its minimal value and the system is moved closer towards the semiclassical limit.

Accordingly, the quantum trajectories move on classical trajectories, but are subjected to stochastic fluctuations which lead to deviations from the classical trajectory. This is illustrated in Fig. 7. If the fluctuation is large enough, the quantum trajectory can jump from one attractor to the other. This is the reason why quantum multistability appears as a dynamic effect. The transition probability of the attractor jump, and thus the time scale of the instability, is essentially determined by the ratio of the width of the wave packet to the distance of the classical trajectories in phase space. In the classical limit $\sigma = 0$ the instabilities disappear and the trajectory remains on the classic trajectory for all time. In the quantum regime $\sigma > 0$, on the other hand, the width of the wavepacket is finite and the transition probability increases the more the wavepacket overlaps with the adjacent classical trajectory. In addition, the random nature of the quantum fluctuations (realized by different noise realizations in numerics) ensures that the quantum trajectories do not remain at the same phase space point but diverge with time, leading to the outspreading visible in Fig. 6.

According to Fig. 5, after a sufficiently long time almost the entire phase space volume is weighted on the outer orbit. This raises the question why the reverse process, i.e. the jump of the quantum trajectories from the outer to the inner orbit, is much less likely. An answer can be found in the power balance derived within the mean field description, which can be understood as a kind of effective potential (U_{eff}) in phase space and takes the form of a double well for the two classical orbits. The tunneling effect (in phase space), induced by the finite Heisenberg uncertainty of the state, causes transitions from one well into the other. The tunneling probabilities, and therefore the stability characteristics of the quantum trajectories, are determined by the height and the width of the potential wall. Thus, the probability of the transition from the inner to the outer orbit (P_{12}) is larger than for the opposite case (P_{21}). In the classical limit

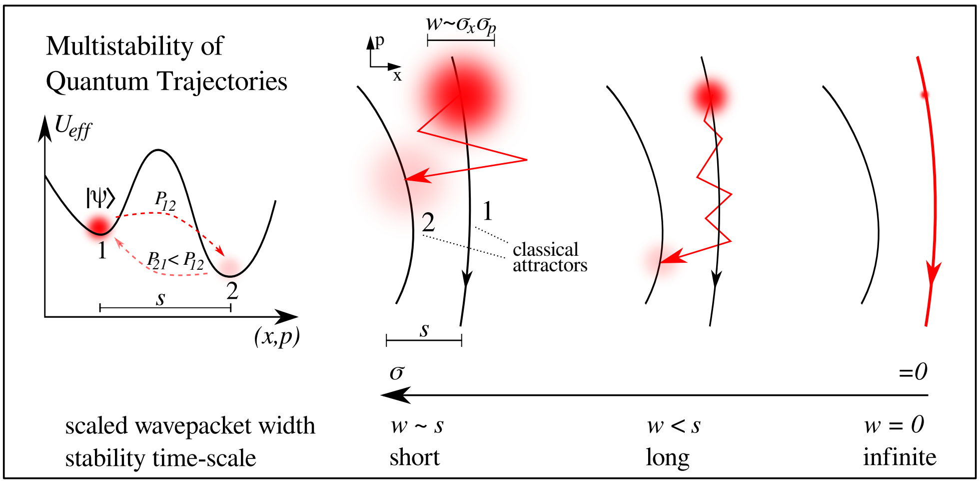

Fig. 7: Single stochastic state picture. Quantum multistability arises as a result of fluctuation induced instabilities, which have their origin in the tunneling through barriers of an effective potential U_{eff} in phase space.

$\sigma = 0$, that is, when the wavepacket width vanishes, the transition probabilities on both sides go to zero. Based on this mechanism, quantum mechanics can protect the system from irregular dynamics by replacing less stable chaotic attractors with the more stable simple periodic orbits [see Figs. 6 (c), 7 and 8 in article I]. We also found that in the quantum regime the system can be localized on simple periodic orbits, although in the classical limit such orbits do not exist as the power balance is not fulfilled [see Fig. 6 (b) in article I].

1.3 Optomechanical Dirac transport

We now turn to the transport dynamics of collective excitations on a two-dimensional array of optomechanical cells. Within an effective Dirac-Weyl theory we study the elastic (articles III,IV) and inelastic (articles IV, V) transport and interconversion processes of light and sound for the scattering problem of a plane light wave that hits laser-induced static and periodically oscillating planar and circular barriers, see Fig. 8 (left part).

Hamiltonian description Given is a honeycomb array of identical cavity-cantilever setups, see Fig. 8 (right part). Each cell for itself is described by the optomechanical Hamiltonian (1) (with $a_L \equiv a$ and $a_R = J = 0$). Close to the semiclassical limit the dynamics of the cavity photon field can be considered as quantum fluctuations around the classical stationary mean-field state α_{cl}. The latter is proportional to the amplitude α of the laser that drives the optomechanical cell. Then, using the linearized equations of motion and performing the rotating-wave approximation in the red detuned regime, $\Delta = -\Omega_m$, the system Hamiltonian reads $H/\hbar = \sum_j \Omega_m b_j^\dagger b_j - \Delta a_j^\dagger a_j - g(b_j^\dagger a_j + a_j^\dagger b_j) - \sum_{\langle ij\rangle} K_a a_i^\dagger a_j + K_b b_i^\dagger b_j + \text{h.c.}$ Here, a_i denotes the fluctuating part of the bosonic operator now. Note that, in the course of linearization, the optomechanical interaction is no longer given by the bare single photon coupling g_0,

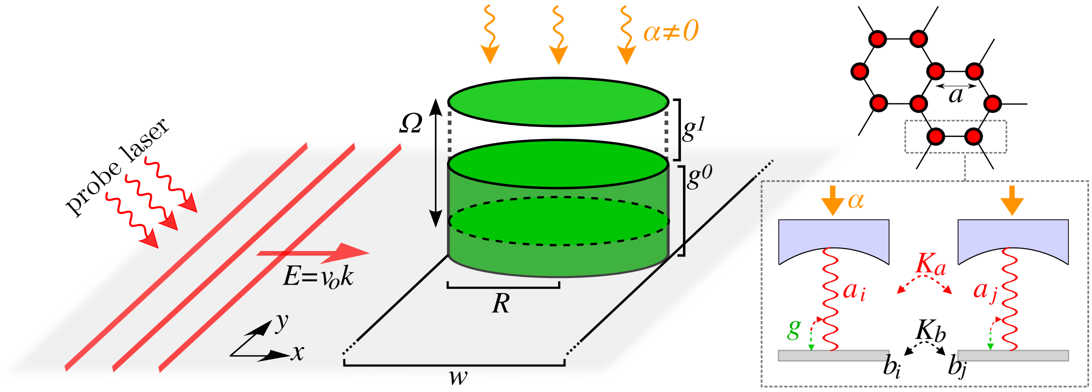

Fig. 8: Scattering geometry. On a honeycomb array of optomechanical cells (gray, see right part) a plane Dirac photon wave of energy E and wavevector $k\boldsymbol{e}_x$ hits a circular (planar) barrier of radius R (width w). The barrier with optomechanical coupling strength $g = g^0 + g^1 \cos(\Omega t)$ is created by an external laser with laser power $\sim \alpha(t)$. Right part: photons and phonons can hop between neighboured sites with tunneling frequency $K_{a/b} = 2v_{o/m}a/3$, where $v_{o/m}$ is the Fermi velocity of the photon/phonon.

but by the effective optomechanical coupling strength $g = g_0\alpha_{cl}$. Its optical tunability allows to create barrier potentials of almost arbitrary shape and heigth. The finite tunneling probability between neighboured sites in the lattice is taken into account by K_a and K_b, in the same way as for the photon-photon interaction in eq. (1b).
Starting from this Hamiltonian description and taking dissipation into account, transport processes in optomechanical graphene have been studied by means of linearized Langevin equations [65]. The numerical analysis of the transport of a low-energy optical wavepacket through a planar barrier has shown, that the phenomena occurring here are robust against dissipation (the main effect of dissipation is the decay of the field amplitudes). In addition, a qualitative agreement was found with the results obtained within the continuum approximation [91], valid for sufficiently low energies and barrier potentials that are smooth on the lattice constant a but sharp on the de Broglie wavelength of the quasiparticle wave. For these reasons we employ this effective description and do not consider dissipative terms explicitly.
Then, the unitary time evolution of the system can be described by the Dirac equation

$$i\hbar \frac{\partial}{\partial t} |\psi(t)\rangle = H |\psi(t)\rangle \tag{9}$$

with the single-valley Dirac-Weyl Hamiltonian ($H \to H - \hbar\Omega_m$)

$$H/\hbar = \left(\overline{v} + \frac{1}{2}\delta v \tau_z\right) \boldsymbol{\sigma} \cdot \boldsymbol{k} - g\tau_x, \tag{10}$$

where $\overline{v} = (v_o + v_m)/2$, $\delta v = v_o - v_m$. Within this first-quantized one-particle description the quasiparticles propagate as optical/mechanical waves with wave vector $\boldsymbol{k}$ and Fermi velocities determined by the photonic/phononic hopping rates, cf. fig 8. Due to the optomechanical and sublattice degrees of freedom, the states are four-fold degenerate. This is reflected by the presence of the Pauli matrices τ, σ in the Hamiltonian (10), corresponding to the (photon-phonon) polariton and sublattice pseudospin, respectively.

The coupling g in the Hamiltonian (10) parametrizes the optomechanical barrier, which is created by a laser that uniformly drives a sharply edged region of the honeycomb array. For a time-independent laser amplitude a stepwise constant barrier is created with coupling strength g^0 and stationary scattering takes place. In order to study dynamic effects of non-stationary scattering, we consider a temporal modeling of the laser with frequency Ω. This additionally leads to a time-dependent component in the coupling strength with amplitude g^1. Two kinds of barrier shapes are considered,

$$g = \left[g^0 + g^1 \cos \Omega t\right] \times \begin{cases} \Theta(x) - \Theta(x-w) & \text{planar barrier} \\ \Theta(r-R) & \text{circular barrier} \end{cases} \tag{11}$$

with (x, y) and (r, φ) as the cartesian and polar coordinates, respectively. For details on various constraints of the barrier parameter values, refer to articles IV,V.
To formulate/solve the scattering problem, the same procedure is used for all cases (for details see the theoretical approaches in articles III-V). First, the wave functions are determined in the different spatial regions, defined by the potential (11). After that, the continuity of the wave functions is used to obtain the scattering coefficients, which in turn enter the scattering quantities. The latter are defined in an appropriate way, depending on the underlying scattering geometry, and are used to discuss the scattering and transport behaviour. In all our calculations we use dimensionless variables, i.e. we employ units such that $\Omega = v_o = \hbar = 1$ ($v_m = 0.1$). Therefore, inelastic scattering is discussed in dependence of the four parameters $E, g^{0,1}, R(w)$. For static barriers a further rescaling can be used so that the two parameters $E/g^0, Rg^0(wg^0)$ remain.

Elastic transport For the elastic transport through the static barrier $g^1 = 0$ the energy is conserved because the Hamiltonian (10) is time-independent. Hence, the wave functions are built up by the eigenfunctions of the Hamiltonian, $|\sigma, k\rangle\, |\tau\rangle$. Here, $|\sigma, k\rangle$ is the eigenvector of the Dirac-Weyl Hamiltonian $H = \boldsymbol{\sigma k}$ with band index $\sigma = \pm 1$ (sublattice pseudospin), and $|\tau\rangle$ is the polariton state with quantum number $\tau = \pm 1$ (polariton pseudospin). The latter is formed as a superposition of the bare optical/mechanical eigenstates $|o/m\rangle$ of τ_z, since photonic and phononic contributions are mixed inside the barrier where $g^0 \neq 0$ and a polariton bandstructure results [cf. eq. (2) and Fig. 1 in article III]. Outside the barrier the optical/mechanical modes are uncoupled, $|\tau\rangle = |o/m\rangle$, and the bandstructure simplifies to the two independent Dirac cones, $E = v_{o/m}\sigma k$. For all scattering problems, including the inelastic case, the incoming photon wave is considered to be in a plane wave state at energy $E > 0$, $|\psi^{in}\rangle = |+1, k\boldsymbol{e}_x\rangle\, |o\rangle$, cf. Fig 8.

Transport through the static planar barrier corresponds to an effectively one-dimensional problem as the photon wave hits the potential perpendicularly. As a result, the helicity is conserved, $\boldsymbol{\sigma k}/k = \text{const.}$, and there are no backscattered waves (Klein tunneling). Due to the optomechanical coupling, behind the barrier $x > w$ the transmitted wave consists of optical and mechanical components, $|+1, k^{o/m}\rangle\, |o/m\rangle$ ($k^o \equiv k$), although no phonon waves are impinging on the potential. Therefore, the transmission probability of the phonon

$$T^m_{st} = \left[1 + k^2 v_o^2 (v_o - v_m)^2 / 4 v_o v_m (g^0)^2\right]^{-1} \sin^2((q^+ - q^-)w/2) \tag{12}$$

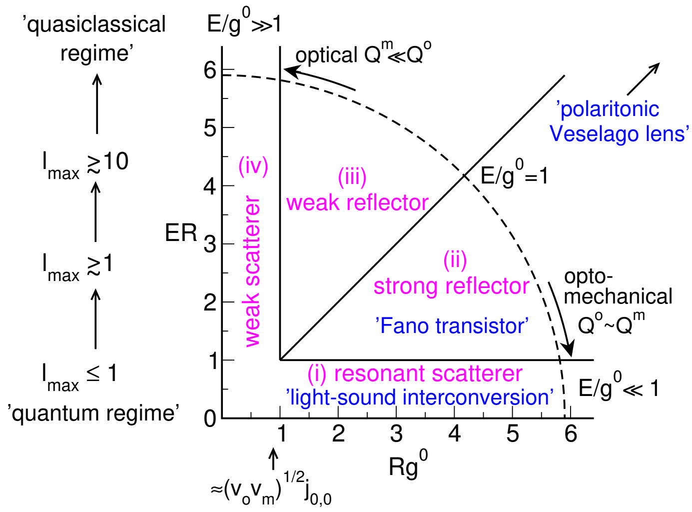

Fig. 9: Scattering regimes for the static circular barrier. The size parameter ER determines the maximum angular momentum l_{max} being possible in the scattering, the energy-coupling ratio E/g^0 switches between the optomechanical and the optical regime. On the Rg^0 axis the resonance $i = 0$ according to eq. (16) with $l = 0$ is marked.

can be understood as a photon-phonon interconversion probability ($q^{\pm}_{st}$ are the waven umbers inside the barrier), which due to $T^o + T^m = 1$ completely characterizes the transport.

Based on eq. (12), substantially two regimes can be distinguished by the energy-coupling ratio E/g^0. For $E/g^0 > 1$ the denominator becomes larger than one and consequently the light-sound interconversion is suppressed. In particular, for $E/g^0 \gtrsim 3$ the transmission becomes almost purely photonic, $T^o_{st} \gg T^m_{st}$ [optical regime, cf. Fig. 1 in article IV]. The reason is that the wave number of the phonon in the barrier is much larger than that of the photon (due to $v_o \gg v_m$) and therefore merges with the linear dispersion of the phonon outside the barrier (cf. Fig. 1 in article III), so that the scattering/transmission of the phonon disappears. In contrast, for $E/g^0 < 1$, the transmission probability of the phonon is comparable to that of the photon, $T^o \sim T^m$ (optomechanical regime). Note that the distinction of these optical and optomechanical regimes holds not only for the planar barrier, but also for the circular barrier, simply because the energy dispersion is not affected by the specific geometry. A very simple picture arises for $E/g_0 \ll 1$. Then, the interference of the polariton waves inside the barrier leads to the formation of standing waves such that the barrier can be understood as a kind of Fabry-Pérot interferometer. In the case of resonance,

$$wg_0 = \sqrt{v_o v_m} n\pi/2 \simeq 0.5n \tag{13}$$

with n even (odd) natural number, constructive interference of the optical (mechanical) wave causes pure photon (phonon) transmission, $T^m_{st} = 0$ ($T^m_{st} = 1$).

For the scattering by the static circular barrier, helicity is in general not conserved (except for $\phi = 0$), thus the wavevectors of the scattered waves have components in any planar direction. Exploiting the symmetry, the incident and reflected wavefunctions ($r > R$) and the transmitted wavefunction ($r \leq R$) are expanded as eigenfunctions of the angular momentum operator (partial waves) with quantum numbers $l = 0, 1, \ldots$ [see eqs. (3) - (6) in article III]. The scattering behavior is characterized by the reflected wavefunction in the far field, which is composed of optical and mechanical components.

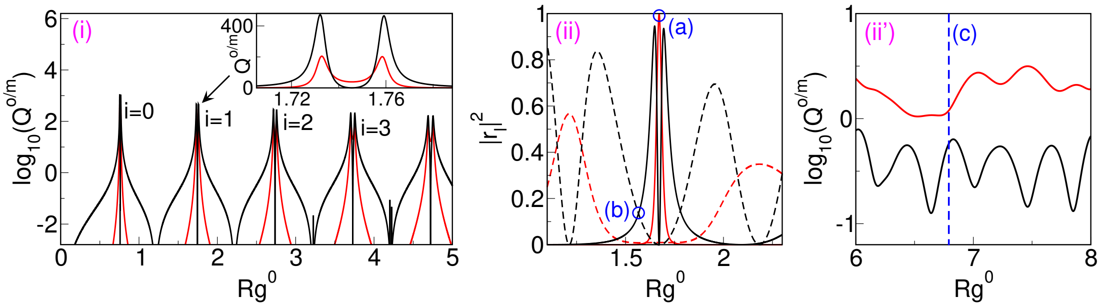

Fig. 10: Scattering efficiency/reflection coefficients of the photon (red) and the phonon (black) as a function of Rg^0 within the resonant scattering regime (i) $E/g^0 = 0.001$ ($ER \ll 1$), the strong reflector regime (ii) $E/g^0 = 0.158$ ($ER \lesssim 1$; dashed $l = 0$, solid $l = 1$), and on the threshold to the weak reflector regime (ii') $E/g^0 = 0.5$ ($ER > 1$).

The radial current density of the reflected wave

$$j^{o/m}(\phi) = \frac{4v_o}{\pi k^{o/m} r} \sum_{l,l'=0}^{\infty} r_{l'}^{o/m*} r_l^{o/m} \left[\cos((l+l'+1)\phi) + \cos((l-l')\phi)\right] \tag{14}$$

describes the angular distribution of the photon/phonon emission by the barrier [the reflection coefficients $r_l^{o/m}$ are given by eqs. (7) - (10) in article III]. For the total intensity we employ the scattering efficiency

$$Q^{o/m} = \frac{4}{k^{o/m}R} \sum_{l=0}^{\infty} |r_l^{o/m}|^2, \tag{15}$$

that is the angle-integrated current density divided by the diameter of the barrier and the incident photon current. Similar to $T^{o/m}$ for the planar barrier, $Q^{o/m}$ can be understood as a photon-phonon interconversion probability.
Compared to the infinite planar barrier, the finite size of the circular barrier leads to a richer scattering behavior. The different scattering regimes can be classified by means of the strength parameter Rg^0 and the size parameter ER and are summarized in Fig. 9 (cf. Fig. 2 in article III). As explained above, the light-sound interconversion rate is determined by the energy-coupling ratio E/g^0 that switches between the optical and the optomechanical regime. In the latter case the barrier acts as a resonant scatterer with resonance condition

$$Rg^0 = \sqrt{v_o v_m}\, j_{l,i}, \tag{16}$$

quite similar as for the planar barrier, cf. eq. (13). Here, $j_{l,i}$ denotes the i'th zero of the Bessel function J_l with $i = 0, 1, 2, \ldots$. For small size parameters, that is, when the wave number of the incident photon wave is large compared to the extension of the barrier (quantum regime), only the first partial waves are excited. This leads to sharp peaks in the scattering efficiency of the photon and the phonon, see panel (i) in Fig. 10.
When the size parameter becomes larger, higher partial waves are resonantly excited and the strong reflector regime is entered, see panel (ii) in Fig. 10. Here, one can switch between entirely photon [case (a)] to phonon scattering [case (b)] just by varying the radius/coupling of the barrier. On the threshold to the weak reflector regime so much

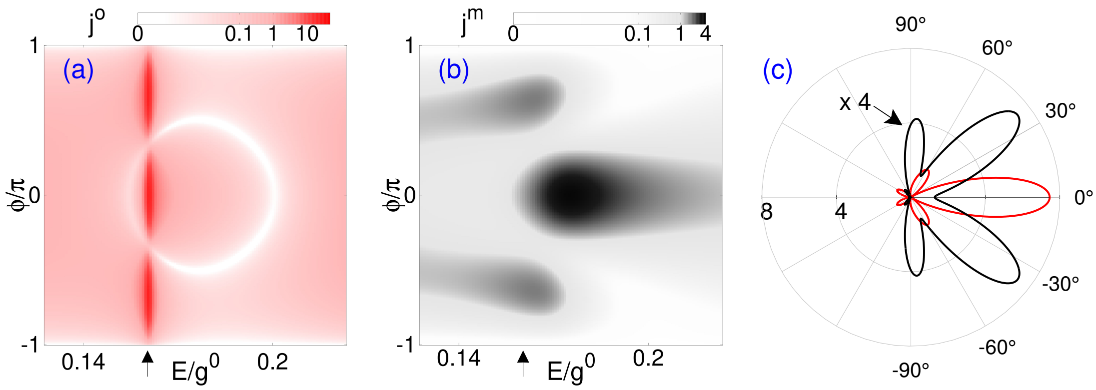

Fig. 11: Far-field current of the photon (red) and the phonon (black) according to eq. (14) in the ϕ-E/g^0 plane (a,b) and as a polar plot (c), corresponding to the cases marked in panel (ii), (ii') in Fig. 10 [arrows mark the energy used in panel (ii)].

partial waves are excited such that the definite resonance pattern is replaced by a more continuous functional behaviour, see panel (ii') in Fig. 10. At the same time phonon scattering is weaker since $E/g^0 \sim 1$. For $E/g^0 > 1$ the scattering becomes optical and the weak reflector regime is entered (for more details see article III).
Resonances feature vortices of the current inside the barrier, leading to a spatial and temporal trapping of the photon-phonon bound state [see Fig. 4 and eqs. (13), (14) in article III]. The specific vortex patterns are reflected in the far-field by a cosinusoidal angle distribution with maxima at $\phi = l'/(2l+1)$ where $l' \in 0, ..., l$, see eq. (14). In addition, interference of different angular contributions $l = 0, 1$ may lead to a Fano resonance [92], detectable as a suppression of forward scattering. Both effects arise for the photon as well as for the phonon, see panels (a),(b) in Fig. 11 (for more details see Fig. 5 in article III). A richer angular scattering distribution arises at higher size parameters, where photons and phonons may be emitted simultaneously into different directions, see panel (c) in Fig. 11. In this way, the circular barrier can be utilized as an angle-dependent light-sound translator in the sense of a Fano transistor. For even larger size parameters (quasiclassical regime) the barrier may act as a polaritonic Veselago lens that focuses the light beam in forward direction (see Fig. 6 in article III).

Inelastic transport For the inelastic transport through the oscillating barrier $g^1 \neq 0$ the energy is not conserved because the Hamiltonian (10) is time-dependent. The polariton states inside the barrier can be treated effectively as periodically driven two-level systems. To find their time-periodic solution based on eq. (9) we employ the Floquet formalism [93] for a two-level system [94–99]. The state vector is given by $|\psi(t)\rangle = \mathrm{e}^{-i\varepsilon t}|\varepsilon(t)\rangle$ with ε as the quasienergy and

$$|\varepsilon(t)\rangle = \sum_p \sum_{\tau=\pm} c_p^\tau |\sigma, \boldsymbol{k}\rangle |\tau\rangle \, \mathrm{e}^{ip\Omega t}, \quad p \in \mathbb{Z}, \tag{17}$$

as the Floquet state expanded in Fourier series. The Fourier coefficients c_p^τ are determined by the Floquet eigenvalue equation $\mathcal{F}\boldsymbol{c} = \varepsilon \boldsymbol{c}$ [the Floquet matrix $\mathcal{F}$ is given by eqs. (A.1) - (A.5) in article V]. Eq. (17) implies that the oscillating barrier gives (takes) energy to (away from) photons and phonons, $E_n = E + n\Omega$. Hence, the wavefunctions

are superpositions of states with energies E_n (central band/sideband states). The wavefunctions outside the barrier are of the form $\sum_n |\sigma_n, k_n\rangle\, |o/m\rangle\, \mathrm{e}^{-iE_nt}$ with wave numbers $k_n^{o/m}$ obtained from the unperturbed dispersion. The wavefunction inside the barrier is composed of Floquet states (17), $\sum_n |\varepsilon^{(\pm)} \stackrel{!}{=} E_n\rangle\, \mathrm{e}^{-iE_nt}$, where the wave numbers $q_n^{(\pm)}$ and Fourier coefficients $c_p^{\tau,(\pm)}$ are obtained from the numerical diagonalization of the Floquet matrix $\mathcal{F}$ [here $(\pm)$ denotes the two levels of the state].
In contrast to the elastic case, the quantum number n is important now and enters the effective parameters E_n/g^0 and E_nR (E_nw) that characterize the inelastic scattering. We found that the significance of the sideband states for the scattering is essentially determined by two aspects. First, the influence of the oscillating barrier becomes larger for larger values of g^1/Ω, since then more sideband states are involved in the scattering. For our explanations we want to stay close to the static problem, which is why we assume $g^1/\Omega \ll 1$ (for more details beyond this regime see Figs. 6,8,9 in article V and corresponding explanations). Second, the location of the energies E_n in the quasienergy bandstructure is important. The scattering is affected by the oscillating barrier if the wave numbers of the time-dependent case deviate from the wave numbers of the time-independent case. These deviations are largest close to avoided crossings in the polaritonic quasienergy bandstructure (see Fig. 12 in article V). Such avoided crossings are located at crossing energies (CE) [given by eq. (16) in article V]. Consequently, the impact of the oscillating barrier becomes largest for photon energy E close to a CE. This is most prominent at symmetric Floquet resonance, that is, when the static coupling g^0 is chosen to be

$$g^0_{sr} = \Omega \frac{\sqrt{v_o v_m}}{v_o + v_m}. \tag{18}$$

Then, different CE cross each other at $E_n = n\Omega$ and therefore the sideband states have a significant impact on the scattering (cf. Fig. 3 in article V).

For the tunneling through the oscillating planar barrier the helicity remains a conserved quantity, thus Klein tunneling persists and no backscattered waves appear. After numerically solving the infinite system of coupled linear equations for the transmission coefficients $t_n^{o/m}$ and making use of the equation of continuity [with time-periodic current density according to eq. (3) in artice IV] one obtains the time-averaged transmission probability

$$\overline{T}^{o/m} = \frac{v_{o/m}}{v_o} \sum_n \left| t_n^{o/m} \right|^2, \tag{19}$$

which can be understood as a photon-phonon conversion probability as $\overline{T}^o + \overline{T}^m = 1$. At symmetric Floquet resonance $g^0 = g^0_{sr}$ the transmission pattern for the static barrier is drastically modified at photon energies $E = 0$ and $E = \Omega$, see Fig. 12. At certain values of wg^0, the optomechanical regime is replaced by the optical regime ($E/g^0 \ll 1$) and vice versa ($E/g^0 \approx 3.5$). Obviously, instead of E/g^0 the effective energy-coupling ratio E_n/g^0 now determines the scattering/transport, which is characterized by the mixing of the different scattering regimes as a result of interference between the different energy states. Better insight into the underlying mechanism is provided by the quasienergy spectrum [cf. Fig. 3/4 (a) in article IV]. Because of the symmetric situation the wave numbers of the wavefunctions under the barrier have equal magnitudes

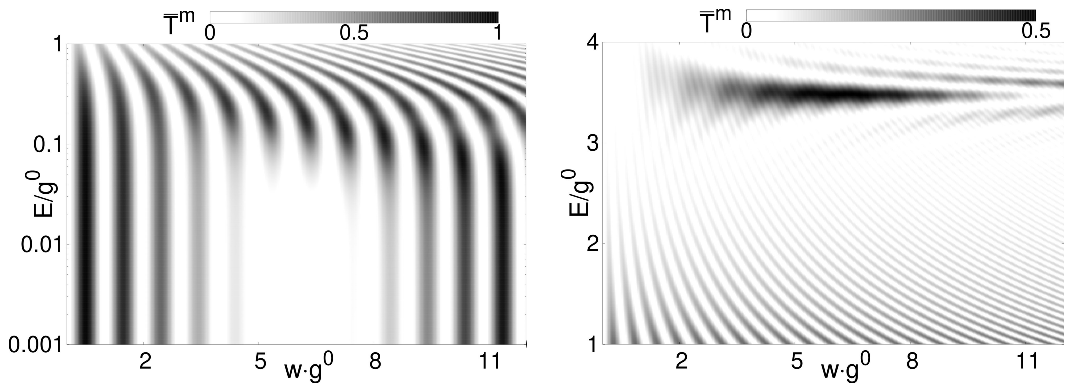

Fig. 12: $\overline{T}^m$ according to eq. (19) in the wg^0-E/g^0 plane for $g^1 = 0.073\Omega$ at symmetric Floquet resonance $g^0 = g^0_{sr}$. The transmission probability of the photon is $\overline{T}^o = 1-\overline{T}^m$.

but are antiparallel to each other, which results in standing optical and mechanical waves of different frequencies [cf. Fig. 3/4 (c) in article IV]. In the same way as for the static case, the oscillating barrier acts as a kind of Fabry-Pérot interferometer, but now also for higher harmonics. This leads to the suppression [cf. Fig. 3 (b) in article IV] or revival [cf. Fig. 4 (b) in article IV] of light-sound interconversion in dependence on wg^0 in Fig. 12. Furthermore, interference of the energy-states causes a time-periodicity in the current density [see Fig. 3/4 (d) in article IV].

For the oscillating circular barrier, in addition to the energy level n the angular momentum quantum number l comes into play. Matching the wave functions [eqs. (4)-(7) in article V], the scattering coefficients are determined by the numerical solution of the coupled linear system, which is solved for the different values of l [eqs. (8)-(11) in article V]. As for the elastic case, the angular scattering is described by the far-field current density of the reflected wave, which is now time-dependent [eq. (14) in article V]. Consequently, the scattering efficiency consists of a time-dependent part [eq. (13) in article V] and a time-averaged part

$$\overline{Q}^{o/m} = \sum_{n=-\infty}^{\infty} \sum_{l=0}^{\infty} \overline{Q}^{o/m}_{n,l} = \sum_{n=-\infty}^{\infty} \sum_{l=0}^{\infty} \frac{4}{k_n^{o/m} R} \left| r^{o/m}_{n,l} \right|^2 , \tag{20}$$

where $\overline{Q}^{o/m}_{n,l}$ represents the optical/mechanical scattering contribution of partial wave l at energy level n.
The interference of the states with energies E_n causes the mixing of the optical ($E_n/g^0 > 1$) and optomechanical ($E_n/g^0 \simeq 0$) regimes, which leads – similar as for the planar barrier – to the suppression and revival of light-sound interconversion. This is shown in Fig. 13 (left part) at symmetric Floquet resonance for the case $E \simeq 0$ (for the case $E \simeq \Omega$ see Fig. 7 in article V). The periodic time-dependence of the radiation characteristics also reveal the periodic time-dependence, which is reflected in the near-field, see Fig. 13 (right part). In the far field, the symmetric excitation of positive and negative energy states $n = \pm 1$ allows for a time-periodic switching between photon and phonon emission with frequency 2Ω [see Fig. 5 and Fig. 4 (d) in article V]. In this context we have argued that the (planar and circular) oscillating barrier can be

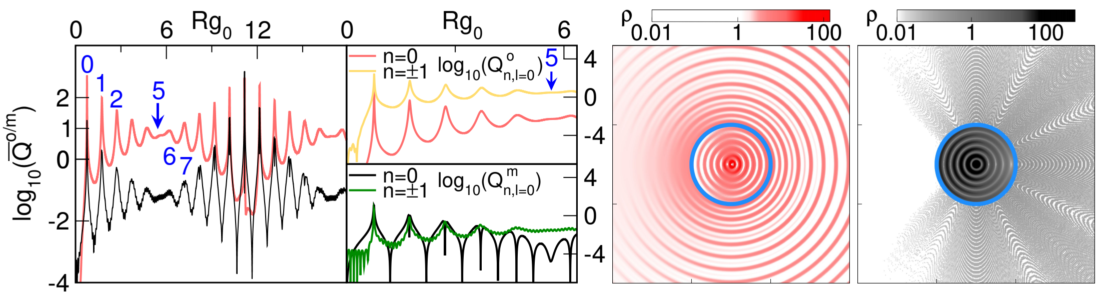

Fig. 13: Left part: time averaged scattering efficiency of the photon (red) and the phonon (black) and scattering contributions as a function of Rg^0 for photon energy $E/g^0 \simeq 0$ and coupling $g^1 = 0.04\Omega$ at symmetric Floquet resonance $g^0 = g^0_{sr}$. Blue numbers denote the resonance points $i = 0, 1...$ with $l = 0$ according to eq. (16). Right part: photon/phonon density $\rho = \langle\psi^{o/m}|\psi^{o/m}\rangle$ inside and outside the circular barrier (blue) at $t = 0$ for a value of Rg^0 corresponding to the $i = 5$'th resonance point.

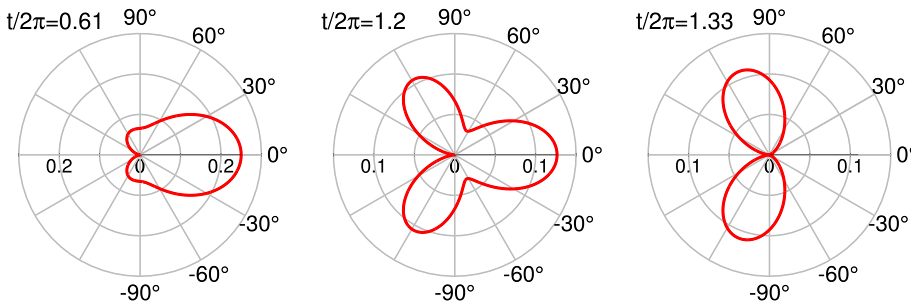

Fig. 14: Polar plots of the time-dependent far-field current density of the optical reflected wave [for parameter values see captions of Figs. 9-11 in article V].

utilized to observe *zitterbewegung*. The exact requirements for a possible experimental implementation are explained in more detail in article V.

The scattering behaviour is further specified by the effective size parameters $E_n R$ which determine the maximum number of partial waves involved. We found that the size parameter of the central band ER determines the maximum number of partial waves l^{max} for all energy channels, whereas the $E_n R$ determine the maximum number of partial waves for the sidebands l_n^{max} with the constraint $l_n^{max} \leq l^{max}$. Thus, for $E \simeq 0$ only partial waves with $l = 0$ are resonant, cf. Fig. 13. This is in contrast to the case $E \simeq \Omega$ for which many partial waves may be resonantly excited (see Fig. 7 in article V). As a consequence of their interference, the weak reflector and the resonant scattering regime are mixed (cf. Fig. 9) and new angle-dependent and time-dependent emission characteristics arise. This is most impressively demonstrated away from symmetric Floquet resonance, that is, when the strong and the weak reflector regimes are mixed [cf. case (3) of Fig. 3 in article V]. The interference of partial waves $l = 0, 1$ at sidebands $n = 0, -1$ [cf. Fig. 10 in article V] causes the time-periodic emission of light in different directions with and without forward scattering, see Fig. 14. In this way the circular barrier can be utilized as a time-periodic Fano transistor.

1.4 Conclusions

For driven optomechanical systems, the light-matter interaction is of crucial importance as it allows to adress different dynamic regimes near the semiclassical limit. In a single optomechanical cell, by varying the bare photon-phonon coupling g_0, effects of multistability can be studied in the classical regime and in the quantum regime. On a honeycomb lattice of optomechanical cells (optomechanical graphene), by varying the effective optomechanical coupling strength and its time-dependent part g^1, elastic and inelastic Dirac transport of light and sound through laser-induced photon-phonon coupling barriers can be studied. The most important stationary and dynamical signatures we identified are summarized in Fig. 15.

As our investigations have shown, dynamical signatures of multistability effects in single optomechanical cells provide a realistic opportunity to observe the quantum-to-classical corssover. Based on the quantum-optical master equation at zero temperature, the quantum-classical transition is formally achieved by rescaling the equations of motion with the quantum parameter g_0/κ (κ is the photon dissipation rate). In the classical limit, that is, when quantum correlations are neglible, multistability is the coexistence of several attractors. A peculiarity of the system are self-sustained oscillations. They occur on the route to chaos and as simple periodic orbits at multiple amplitudes, and can be explained by means of an effective potential (power balance). In the quantum regime, multistability is a dynamic effect. Quantum corrections, resulting from the nonlinear photon-phonon interaction in the semiclassical equations of motion, cause the uncertainty product to increase over time and lead to significant deviations from the classical cantilever motion. At the same time, due to decoherence, the system is close to a classical ensemble. For this reason, quantum multistability appears as the distribution of the cantilever phase space volume on classical attractors. For interpretation we have employed quantum trajectories (quantum state diffusion), which can jump between classical attractors due to noise-induced quantum fluctuations. We have argued that the attractor jump can be attributed to the tunneling through the effective mean field potential wall in phase space. Within this semiclassical picture, the tunneling probability determines the fluctuations and thus the time scale of the quantum jump, and establishes the quantum-to-classical transition: While in the quantum regime the tunneling probability is finite and the trajectory leaves the classical attractor after a certain time to jump onto another one, in the classical limit the trajectory remains on the attractor for all times because the Heisenberg uncertainty (the potential wall) approaches zero (goes to infinity). The specific stability characteristics are determined by the shape of the potential. As a result, quantum mechanics can protect the system from irregular motion in the sense that chaotic attractors are replaced by the more stable simple periodic orbits. For this case, an exponential relation between transient lifetime and quantum parameter has already been detected [100]. Based on these results, we conclude that there is a close connection between the tunneling mechanism and the noise-terms for quantum trajectories near the semiclassical limit. Future studies should address this problem in more detail, ideally involving finite temperatures. In this context, it must be clarified how the tunneling effect is to be understood in the presence of time-dependent effective potentials, such as for simple periodic orbits.

Our investigations in the second part of this thesis have shown, that many of the phenomena found for driven and undriven transport of Dirac electrons through circular and

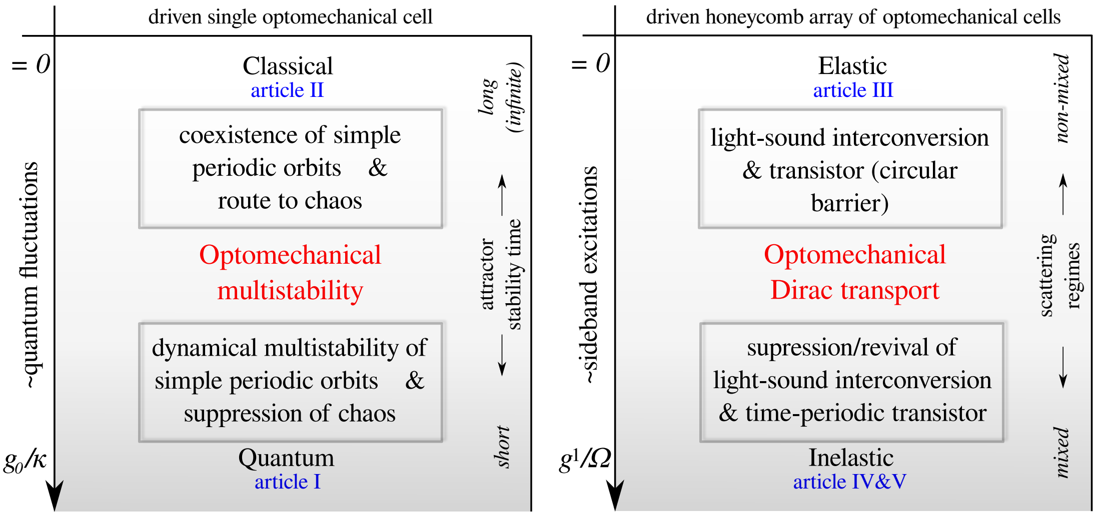

Fig. 15: Main results (boxes) of the two aspects studied in this thesis (colored red) with underlying mechanisms.

planar potential barriers in graphene, occur in a novel way in optomechanical graphene as a result of the photon-phonon interaction. In the case of static barriers ($g^1/\Omega = 0$), the phonon-affected transport in the barrier leads to the energy-conserved interconversion between light and sound. For the planar barrier, this effect can be attributed to Fabry-Pérot resonances of standing optical and mechanical waves. A special feature is the occurrence of Klein tunneling, that is the unimpeded penetration of the barrier at normal incidence of the photon wave on the barrier. In contrast, the finite size of the circular barrier leads to an angle-dependent light-sound conversion (transistor), accompanied by spatial and temporal trapping by the barrier, lensing, and depletion of forward scattering (Fano resonances). We found that different scattering regimes can be characterized by the energy of the incident photon wave, as well as the width and height of the potential barrier. In the case of oscillating barriers ($g^1/\Omega > 0$), the transport becomes inelastic due to the excitation of sideband states with quantized energies in the form of integer multiples of the oscillation frequency Ω. We have shown that the scattering behavior is drastically modified when the energy of the photon wave (sideband state) is close to an avoided crossing in the quasienergy spectrum (Floquet resonance). This holds even in the antiadiabatic limit, that is for small values of g^1/Ω, when only a few sidebands are excited. The interference of the energy states results in the mixing of the scattering regimes, i.e., a mixing of long-wavelength (quantum) and short-wavelength (quasiclassical) regimes. A result may be the suppression or revival of light-sound interconversion in dependence on the extension of the barrier. Moreover, the circular barrier may act as a time-periodic (Fano-)transistor that converts light into sound in different directions. As a further point we have shown that the oscillating barrier provides the energetic conditions to observe *zitterbewegung*. Although our model is based on a one-particle Hamiltonian description, the results should be of fundamental interest to signal processing applications based on laser-driven optomechanical metamaterials. Future studies should examine the influence of dissipation on wave packet dynamics in a more realistic description beyond the continuum approximation.

2 Thesis Articles

Author Contribution

Article I:
Optomechanical multistability in the quantum regime, C. Schulz, A. Alvermann, L. Bakemeier, and H. Fehske, *Europhys. Lett.* **113**, 64002 (2016). Copyright (2016) by EPLA.
C. Schulz, A. Alvermann, L. Bakemeier, and H. Fehske outlined the scope and strategy of the calculation. The calculation was performed by C. Schulz. A. Alvermann wrote the manuscript which was edited by all authors.

Article II:
Symmetry-breaking oscillations in membrane optomechanics, C. Wurl, A. Alvermann, and H. Fehske, *Phys. Rev. A* **94**, 063860 (2016). Copyright (2016) by the American Physical Society.
C. Wurl, A. Alvermann, and H. Fehske outlined the scope and strategy of the calculation. The calculation was performed by C. Wurl. A. Alvermann and C. Wurl wrote the manuscript which was edited by all authors.

Article III:
Light-sound interconversion in optomechanical Dirac materials, C. Wurl, and H. Fehske, *Scientific Reports* **7**, 9811 (2017). Open access.
C. Wurl and H. Fehske outlined the scope and strategy of the calculation. The calculation was performed by C. Wurl. H. Fehske wrote the manuscript which was edited by C. Wurl.

Article IV:
Time-periodic Klein tunneling through optomechanical Dirac barriers, C. Wurl, and H. Fehske, *arXiv:1811.11604* (2018). Accepted for publication in *European Journal of Physics: Special Topics* (Proceedings FQMT17).
C. Wurl and H. Fehske outlined the scope and strategy of the calculation. The calculation was performed by C. Wurl. C. Wurl and H. Fehske wrote the manuscript.

Article V:
Floquet scattering of light and sound in Dirac optomechanics, C. Wurl and H. Fehske, *arXiv:1809.10043v2* (2018). Accepted for publication in *Phys. Rev. A*.
C. Wurl and H. Fehske outlined the scope and strategy of the calculation. The calculation was performed by C. Wurl. C. Wurl and H. Fehske wrote the manuscript.

Confirmed:

(Prof. Dr. Holger Fehske) Greifswald, 10 December 2018

(Christian Wurl) Greifswald, 10 December 2018

A LETTERS JOURNAL EXPLORING THE FRONTIERS OF PHYSICS

Società Italiana di Fisica

sciences IOP Institute of Physics

LETTER

Optomechanical multistability in the quantum regime

To cite this article: C. Schulz *et al* 2016 *EPL* **113** 64002

Related content

- The optomechanical instability in the quantum regime
  Max Ludwig, Björn Kubala and Florian Marquardt
- Macroscopic quantum mechanics: theory and experimental concepts of optomechanics
  Yanbei Chen
- Stochastic differential equations for quantum dynamics of spin-boson networks
  Stephan Mandt, Darius Sadri, Andrew A Houck et al.

A Letters Journal Exploring the Frontiers of Physics

March 2016

EPL, **113** (2016) 64002
www.epljournal.org
doi: 10.1209/0295-5075/113/64002

Optomechanical multistability in the quantum regime

C. Schulz, A. Alvermann[(a)], L. Bakemeier and H. Fehske

Institute of Physics, Ernst-Moritz-Arndt-University of Greifswald - 17487 Greifswald, Germany

received 16 January 2016; accepted in final form 31 March 2016
published online 11 April 2016

PACS 42.50.Ct – Quantum description of interaction of light and matter; related experiments
PACS 37.10.Vz – Mechanical effects of light on atoms, molecules, and ions
PACS 07.10.Cm – Micromechanical devices and systems

Abstract – Classical optomechanical systems feature self-sustained oscillations, where multiple periodic orbits at different amplitudes coexist. We study how this multistability is realized in the quantum regime, where new dynamical patterns appear because quantum trajectories can move between different classical orbits. We explain the resulting quantum dynamics from the phase space point of view, and provide a quantitative description in terms of autocorrelation functions. In this way we can identify clear dynamical signatures of the crossover from classical to quantum mechanics in experimentally accessible quantities. Finally, we discuss a possible interpretation of our results in the sense that quantum mechanics protects optomechanical systems against the chaotic dynamics realized in the classical limit.

Introduction. – The interaction of light with mechanical objects [1,2] enjoys continued interest due to the successful construction and manipulation of optomechanical devices over a wide range of system sizes and parameter combinations (see the recent reviews [3,4] and references cited therein). With these devices both classical nonlinear dynamics, such as self-sustained oscillations [5–8] and chaos [9–11], and quantum-mechanical mechanisms, such as cooling into the ground state [12,13] and quantum non-demolition measurements [14–16], can be studied in a unified experimental setup.

This raises the question as to whether it might be possible to detect the crossover from classical to quantum mechanics directly in the dynamical behaviour of optomechanical systems. In a previous paper [11] we observed that the classical dynamical patterns, which are characterized by the multistability of self-sustained oscillations, change in a characteristic way if one moves into the quantum regime. Previously stable orbits become unstable, the system oscillates at a new amplitude, and especially the classical chaotic dynamics is almost immediately replaced by simple periodic oscillations. In this paper we explain this behaviour from the point of view of classical and quantum phase space dynamics. Most importantly, we will show that the dynamical patterns do not change at random but that clearly identifiable and new signatures can be observed.

(a) E-mail: alvermann@physik.uni-greifswald.de

The prototypical optomechanical system is a vibrating cantilever subject to the radiation pressure of a cavity photon field, for which the Hamilton operator reads [3,4,17]

$$\begin{aligned}\frac{1}{\hbar}H \;=\; & \left[\Omega_{\mathrm{cav}} - \Omega_{\mathrm{las}} + g_{\mathrm{rad}}(b^\dagger + b)\right] a^\dagger a \\ & + \Omega b^\dagger b + \alpha_{\mathrm{las}}(a^\dagger + a),\end{aligned} \tag{1}$$

where $b^{(\dagger)}$ and $a^{(\dagger)}$ are bosonic operators for the vibrational mode of the cantilever (frequency Ω) and for the cavity photon field (Ω_{cav}), respectively. This Hamilton operator applies to any generic optomechanical system, but we adopt the cavity-cantilever terminology throughout this paper. For our theoretical analysis we use the quantum-optical master equation [18]

$$\partial_t \rho = -\frac{\mathrm{i}}{\hbar}[H,\rho] + \Gamma\mathcal{D}[b,\rho] + \kappa\mathcal{D}[a,\rho] \tag{2}$$

for the cantilever-cavity density matrix $\rho(t)$, with the dissipative terms

$$\mathcal{D}[L,\rho] = L\rho L^\dagger - \frac{1}{2}(L^\dagger L\rho + \rho L^\dagger L) \tag{3}$$

that account for cantilever damping ($\propto \Gamma$) and radiative losses ($\propto \kappa$). Note that the above Hamilton operator is given in a frame that rotates with the frequency Ω_{las} of the external pump laser such that only the cavity-laser detuning $\Omega_{\mathrm{cav}} - \Omega_{\mathrm{las}}$ appears, and that we assume zero temperature in the master equation.

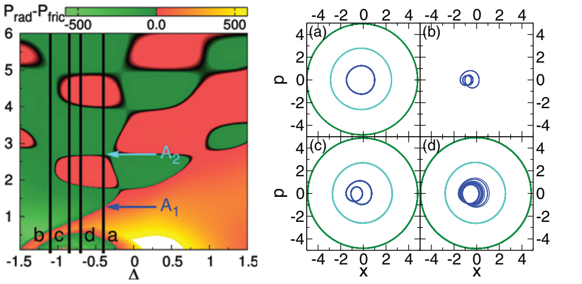

Fig. 1: (Color online) Left panel: chart of self-sustained oscillations in the classical limit for $P = 1.5$. Self-sustained oscillations occur for amplitudes A where the power balance between gains from the radiation pressure ($P_{\rm rad} = P\langle|\alpha|^2 {\rm Im}\beta\rangle_{\rm avg}$) and losses due to friction ($P_{\rm fric} = \bar{\Gamma}\langle|\beta|^2\rangle_{\rm avg}$) changes from positive to negative values with increasing A [5,6]. Right panels: classical orbits in the (x,p) cantilever phase space, for (a) $\Delta = -0.4$, (b) $\Delta = -1.1$, (c) $\Delta = -0.85$, and (d) $\Delta = -0.7$, as marked by vertical lines in the left panel. In case (a), the two innermost orbits have amplitudes $A_1 \approx 1.2$ and $A_2 \approx 2.7$. In cases (b), (c) the innermost orbit shows a few period doubling bifurcations that occur on the route to chaos [11], in case (d) it is chaotic.

Now introduce the five dimensionless parameters [5,6]

$$\Delta = \frac{\Omega_{\rm las} - \Omega_{\rm cav}}{\Omega}, \quad P = \frac{8\alpha_{\rm las}^2 g_{\rm rad}^2}{\Omega^4}, \quad \sigma = \frac{g_{\rm rad}}{\kappa}, \tag{4}$$

and $\bar{\kappa} = \kappa/(2\Omega)$, $\bar{\Gamma} = \Gamma/(2\Omega)$, and measure time as $\tau = \Omega t$. The parameter Δ gives the detuning of the pump laser and cavity, while P gives the strength of the laser pumping. For later numerical results we set the damping parameters $\bar{\kappa} = 0.5$, $\bar{\Gamma} = 5 \times 10^{-4}$ to typical experimental values [4].

The quantum-classical scaling parameter σ is the ratio of the quantum-mechanical quantity $g_{\rm rad}$, which is of order $\hbar^{1/2}$ because the quantum-mechanical position operator $\hat{x} \propto \hbar^{1/2}(b^\dagger + b)$ of the cantilever enters the expression for the radiation pressure, to the classical quantity κ that measures the cavity quality. The parameter σ thus controls the crossover from classical ($\sigma = 0$) to quantum ($\sigma > 0$) mechanics [6]. In the following we will increase σ to move into the quantum regime, but keep $\sigma \ll 1$ in order to remain in the vicinity of the classical limit $\sigma = 0$.

Classical multistability. – Our analysis begins in the limit $\sigma = 0$, where the optomechanical system is described by the classical equations of motion [6]

$$\partial_\tau \alpha = ({\rm i}\Delta - \bar{\kappa})\alpha - {\rm i}(\beta + \beta^*)\alpha - \frac{1}{2}{\rm i}, \tag{5a}$$

$$\partial_\tau \beta = (-{\rm i} - \bar{\Gamma})\beta - \frac{1}{2}{\rm i}P|\alpha|^2 \tag{5b}$$

for the cavity and cantilever phase space variables $\alpha = (\Omega/(2\alpha_{\rm las}))\langle a\rangle$, $\beta = (g_{\rm rad}/\Omega)\langle b\rangle$. We also use the cantilever position and momentum operator $\hat{x} = (1/\sqrt{2})(g_{\rm rad}/\Omega)(b^\dagger + b)$, $\hat{p} = ({\rm i}/\sqrt{2})(g_{\rm rad}/\Omega)(b^\dagger - b)$, with corresponding phase space variables $x = \langle\hat{x}\rangle = 1/\sqrt{2}\,(\beta + \beta^*)$ and $p = \langle\hat{p}\rangle = ({\rm i}/\sqrt{2})(\beta^* - \beta)$.

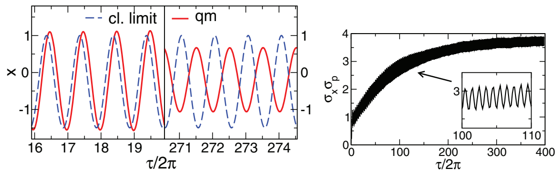

Fig. 2: (Color online) Left panel: cantilever position $x(\tau)$ from the classical equations of motion (5) and from the quantum-mechanical master equation (2) at $\sigma = 0.1$, for $P = 1.5$, $\Delta = -0.4$ (case (a) in fig. 1). Right panel: cantilever position-momentum uncertainty product $\sigma_x\sigma_p$ for the same parameters.

The classical equations of motion predict the onset of self-sustained cantilever oscillations $x(\tau) = x_0 + A\cos\tau$ as the pump power P is increased. Figure 1 shows the possible amplitudes A of these oscillations, which are obtained with the ansatz from ref. [5], for the value $P = 1.5$. We keep this value fixed throughout the paper, as the behaviour discussed here does not depend on it. Note in fig. 1 that several stable oscillatory solutions at different amplitudes A can coexist for one parameter choice. This classical multistability of self-sustained oscillations is the origin of the quantum multistability analyzed next.

Quantum multistability. – We now move into the quantum regime by letting σ become finite. In all our examples the quantum system is initially prepared in the pure product state of a coherent cantilever and cavity state at $\alpha = \beta = 0$, *i.e.*, in the state that is closest to a classical state at these coordinates. The cantilever-cavity density matrix is then evolved according to eq. (2).

Figure 2 shows the cantilever position x and the position-momentum uncertainty product $\sigma_x\sigma_p$, with the uncertainty $\sigma_O = (\langle\hat{O}^2\rangle - \langle\hat{O}\rangle^2)^{1/2}$ of an observable O. The quantum dynamics at finite σ closely follows the classical oscillations for an initial period of time, before it deviates significantly at later times. Deviations occur because the quantum state spreads out in phase space, as witnessed by the growth of the uncertainty product, whereby the cantilever position is smeared out.

The full phase space dynamics in fig. 3, which we display with the Wigner function $W(x,p)$ of the cantilever mode (see, *e.g.*, ref. [19] for the definitions), reveals a more definite dynamical pattern. For early times ($\tau \simeq 16$) the Wigner function retraces the classical orbit with amplitude $A_1 \approx 1.2$ from case (a) in fig. 1. At later times ($\tau \simeq 64$) the Wigner function shows a contribution from a second circular orbit with larger amplitude, before almost all weight is concentrated on the new orbit ($\tau \simeq 270$). In comparison to case (a) in fig. 1 this orbit is identified as the second classical orbit with amplitude $A_2 \approx 2.7$. During time evolution the quantum state spreads out along, but not perpendicular to, these two classical orbits.

The classical multistability of the optomechanical system thus has a direct counterpart in the quantum dynamics at small σ, where the system moves between the

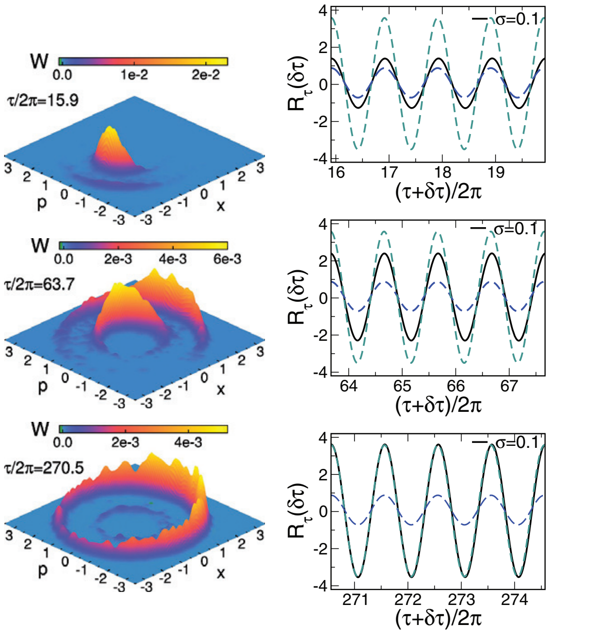

Fig. 3: (Color online) Wigner function $W(x,p)$ in cantilever phase space (left panels) and cantilever position autocorrelation function $R_\tau(\delta\tau)$ (right panels) for case (a) from fig. 1, at $\sigma = 0.1$ slightly away from the classical limit. The autocorrelation functions for the two inner classical orbits at amplitudes $A_{1/2}$ are included as dashed curves.

different classical orbits. This kind of quantum multistability leads to distinct dynamical features because the oscillatory nature of the different orbits is preserved.

The quantum multistability is clearly detected with the cantilever position autocorrelation function

$$R_\tau(\delta\tau) = \int_{\tau-\pi}^{\tau+\pi} \langle \hat{x}(\tau')\hat{x}(\tau'+\delta\tau)\rangle \, \mathrm{d}\tau', \tag{6}$$

instead of the position expectation value that averages over the phase space distribution. We choose this function because the dynamics is best described in cantilever phase space. Autocorrelation functions for the cavity mode could be used as well and should be more accessible to experimental measurements, but their interpretation is less straightforward because of the additional sidebands at multiples of the fundamental oscillation frequency.

The autocorrelation function in fig. 3 is the weighted sum of the oscillatory motion on the two orbits seen in the Wigner function. The frequency of the two orbits is identical (essentially, the cantilever frequency Ω), such that only one oscillation is visible in $R_\tau(\delta\tau)$. The amplitude of $R_\tau(\delta\tau)$ increases as weight is transferred from the inner to the outer orbit. Noteworthy, the oscillations persist at all times. In this way, the multistability of the quantum dynamics is not only observable during a short initial time period but during extended periods of time.

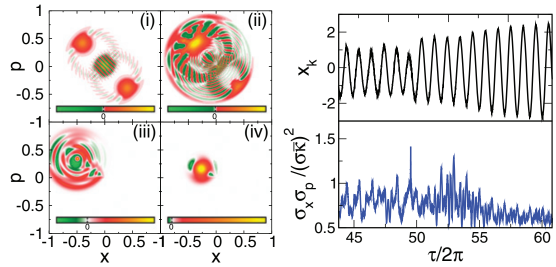

Fig. 4: (Color online) Left panels: Wigner function $W(x,p)$ for a single quantum trajectory starting from a "Schrödinger cat" state at (i) $\tau = 0$, and at later times (ii) $\tau = 0.001$, (iii) $\tau = 0.008$, and (iv) $\tau = 0.4$. Right panels: cantilever position x_k and uncertainty product $\sigma_x\sigma_p$ (see eq. (8)) for a single quantum trajectory at later times, in the situation of fig. 5. All results are for case (a) from fig. 1 and $\sigma = 0.1$.

Multistability of quantum trajectories. – The mechanism behind the quantum multistability can be understood through the phase space dynamics of individual quantum trajectories, as they arise in the quantum state diffusion (QSD) approach [20] to the solution of Lindblad master equations such as eq. (2).

In QSD the density matrix is represented by an ensemble of quantum trajectories $|\psi_k(\tau)\rangle$, from which it is obtained as an average

$$\rho(\tau) = \mathsf{mean}_k \Big\{ |\psi_k(\tau)\rangle\langle\psi_k(\tau)| \Big\}. \tag{7}$$

Accordingly, expectation values are computed as ensemble averages $O(\tau) = \mathrm{tr}[\rho(\tau)\hat{O}] = \mathsf{mean}_k \Big\{ \langle\psi_k(\tau)|\hat{O}|\psi_k(\tau)\rangle \Big\}$. Each quantum trajectory $|\psi_k(\tau)\rangle$ follows a stochastic equation of motion that combines the Hamiltonian and dissipative dynamics with a noise term [20]. Numerically, the density matrix is obtained through Monte Carlo sampling of the trajectories for different noise realizations. We use the QSD implementation from ref. [21], and typically average over $\simeq 3000$ trajectories to obtain the results in figs. 2–4, 7, 8. Although a single quantum trajectory is not observable by itself, the phase space dynamics of individual trajectories as shown in figs. 5, 6 allows us to deduce the properties of the entire density matrix.

Close to the classical limit quantum trajectories evolve rapidly into localized phase space states as a consequence of dissipation [22–24]. This is illustrated in fig. 4 for a single trajectory that starts from a "Schrödinger cat" state, given as the superposition of two coherent states, with the characteristic interference pattern in the Wigner function. In less than one oscillation period ($\tau = 0.4 < 1$) the trajectory evolves into a nearly coherent state with a positive Wigner function, which shows the rapid decoherence. The quantum trajectory remains in such a state during the subsequent time evolution, and the uncertainty product stays close to its minimal value

$$\sigma_q\sigma_p \geq \frac{1}{2}(g_{\mathrm{rad}}/\Omega)^2 = \frac{1}{2}(\sigma\bar{\kappa})^2 \tag{8}$$

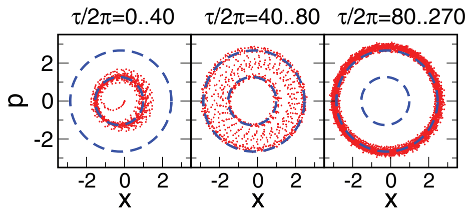

Fig. 5: (Color online) Stroboscopic (x,p) phase space plot of a single quantum trajectory (red dots), for case (a) from fig. 1 and $\sigma = 0.1$, at early (left panel), intermediate (central panel), and later (right panel) times τ as indicated. The initial conditions are $x(0) = p(0) = 0$, the quantum system is prepared in a coherent state at these coordinates. The two classical orbits at amplitudes $A_{1/2}$ are depicted with dashed curves.

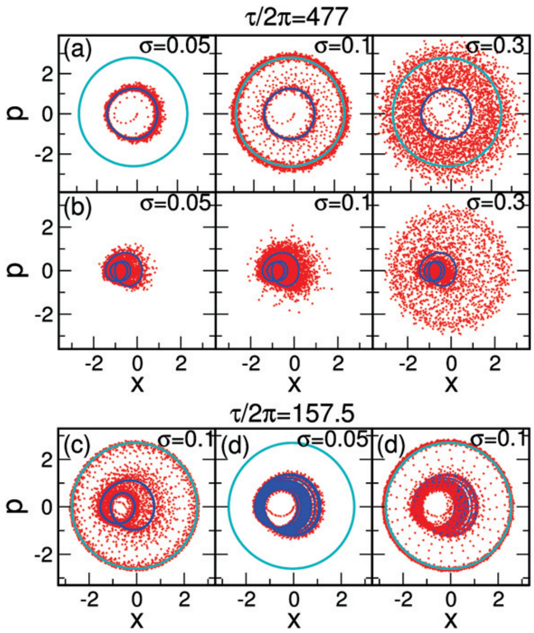

Fig. 6: (Color online) Phase space plot of many quantum trajectories in the QSD ensemble (red points) for cases (a)–(d) from fig. 1, different times τ, and values of σ as indicated. In all cases, the two innermost classical orbits from fig. 1 are included as solid curves. In case (b) the second orbit is missing.

given by the Heisenberg uncertainty relation for the $\hat{x}$, $\hat{p}$ operators (here, the quantum-classical scaling parameter σ comes into play). Notice that phase space localization occurs only in the vicinity of the classical limit, for $\sigma \ll 1$. It also explains the transition into the classical limit: For $\sigma \to 0$ the quantum trajectories evolve infinitely fast into minimal uncertainty states, and at the same time the lower bound in eq. (8) goes to zero. Then, every trajectory occupies one point in phase space, *i.e.*, it has become classical. Under this condition, the classical equations of motion (5) can be derived directly from the master equation (2).

Because a quantum trajectory is very localized in phase space it is well represented by a single phase space point, similar to a classical trajectory. In fig. 5 this representation is used for a stroboscopic phase space plot of a single quantum trajectory that contributes to the Wigner functions in fig. 3. This plot clearly shows the multistability of the quantum trajectory, which initially follows the inner orbit before it moves towards the outer orbit. During the time evolution the quantum trajectory follows the oscillatory motion of the two orbits at the cantilever frequency, and because the trajectory state is well localized in phase space, these oscillations are not averaged out but appear directly in the position expectation value $x_k(\tau) = \langle \psi_k(\tau) | \hat{x} | \psi_k(\tau) \rangle$ that is depicted in fig. 4.

Since every individual trajectory shows this type of quantum multistability it is also seen in the entire density matrix, given as the ensemble average of all trajectories. Because of the noise term in the stochastic QSD equation of motion the quantum trajectories are not exactly at the same phase space point but at different points on the respective orbits. This results in the broad distribution of the relative angle in phase space seen in the Wigner functions in fig. 3 especially at later times, when the quantum trajectories are spread out fully along the second orbit. Consequently, all oscillations are averaged out in expectation values such as the cantilever position $x(\tau)$ in fig. 2. Such values are, therefore, not the right quantities to detect the quantum multistability.

Instead, successful detection requires autocorrelation functions such as $R_\tau(\delta\tau)$ from eq. (6). Similar to the density matrix the function $R_\tau(\delta\tau)$ can be expressed (dropping the τ'-integration here) as an ensemble average,

$$R_\tau(\delta\tau) = \sum_k x_k(\tau)\, x_k(\tau+\delta\tau) + \sum_k \langle (\hat{x}(\tau) - x_k(\tau))\,(\hat{x}(\tau+\delta\tau) - x_k(\tau+\delta\tau)) \rangle_k, \quad (9)$$

where the expectation value $\langle \cdot \rangle_k = \langle \psi_k | \cdot | \psi_k \rangle$ is computed for each individual quantum trajectory. The correlation function in the second line is bounded by

$$|\langle (\hat{x}(\tau) - x_k(\tau))\,(\hat{x}(\tau+\delta\tau) - x_k(\tau+\delta\tau)) \rangle_k|^2 \leq \left\langle (\hat{x}(\tau) - x_k(\tau))^2 \right\rangle_k \left\langle (\hat{x}(\tau+\delta\tau) - x_k(\tau+\delta\tau))^2 \right\rangle_k . \quad (10)$$

Whenever the position uncertainty $\langle (\hat{x} - x_k)^2 \rangle_k$ of each trajectory becomes small, as is the case for $\sigma \ll 1$, the autocorrelation function $R_\tau(\delta\tau)$ is thus given by the ensemble average of the autocorrelation functions of the individual trajectories, *i.e.*, by the first line in eq. (9). Accordingly, the oscillations seen in $x_k(\tau)$ for each individual trajectory (cf. fig. 4) are preserved in the autocorrelation function in spite of the ensemble average. Furthermore, $R_\tau(\delta\tau)$ is the weighted sum of the autocorrelation functions for the different classical orbits, which are directly related to the orbit amplitudes $A_{1/2}$ as seen in fig. 3.

Notice that the behaviour described here —the motion of quantum trajectories between different classical orbits— emerges only because the trajectory states $|\psi_k\rangle$

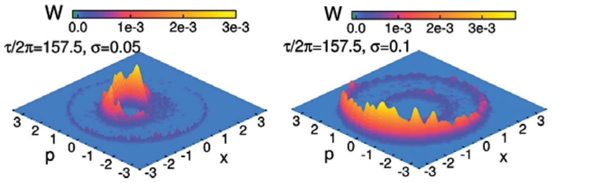

Fig. 7: (Color online) Wigner function $W(x,p)$ in cantilever phase space for case (d) from fig. 1, for τ and σ as in fig. 6.

deviate from coherent states. The noise terms in the QSD equations have the form $\bar{\Gamma}(b - \langle b \rangle_k)|\psi_k\rangle \mathrm{d}\xi$, here for the mechanical damping, with a random variable $\mathrm{d}\xi \propto \mathrm{d}\tau^{1/2}$ from the underlying Wiener process [20]. If $|\psi_k\rangle$ is exactly a coherent state, such that $(b - \langle b \rangle_k)|\psi_k\rangle = 0$, the noise term will vanish identically. This observation explains why the "quantum noise" disappears in the classical limit $\sigma = 0$, and the quantum trajectories follow the deterministic classical equations of motion (5). At finite but small $\sigma \ll 1$ trajectories are almost but not exactly in coherent states. The noise terms become effective but remain small, such that the quantum trajectories still follow the classical dynamics but are subject to a small stochastic correction. This small correction can change the long-time stability of classical orbits and their basin of attraction but does not destroy the classical dynamical patterns. Consequently, the quantum trajectories do not move arbitrarily in phase space but follow a classical orbit for some time before they leave the orbit with a finite probability. Afterwards, the trajectories can settle on a different attractive orbit if such an orbit exists at larger amplitudes.

Quantum multistability and classical orbits. – The quantum multistability observed for case (a) from fig. 1 depends on the presence of at least two classical orbits between which the quantum trajectories can move. The remaining cases (b)–(d) are variations of this situation, where either the second orbit is missing (case (b)) or the nature of the first orbit has changed (cases (c), (d)). The four cases are compared in fig. 6 with phase space plots of many quantum trajectories that represent the QSD ensemble for the density matrix.

In all cases the time scale relevant for quantum multistability shortens with increasing σ because the quantum trajectories leave the first classical orbit more rapidly when the noise terms become larger. For too large σ (*e.g.*, $\sigma = 0.3$ in case (a)) the clear dynamical pattern of quantum multistability —the movement between different classical orbits— disappears altogether.

In case (b) the quantum trajectories cannot settle on a nearby classical orbit once they left the first orbit. Quantum multistability, which is characterized by the prevalence of oscillatory motion over random diffusion, cannot be observed in such a situation.

In cases (c), (d) the inner orbit is no longer simpler periodic but a period-two orbit after the first period doubling bifurcation on the route to chaos (case (c)) or a chaotic

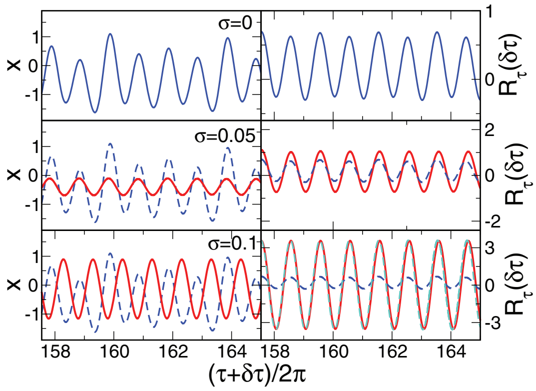

Fig. 8: (Color online) Cantilever position $x(\tau)$ (left panels) and position autocorrelation function $R_\tau(\delta\tau)$ (right panels) for case (d) at finite σ, in comparison to the results in the classical limit $\sigma = 0$ (top panels, and dashed curves in the lower panels). These curves correspond to the Wigner functions in fig. 7.

orbit (case (d)). Quantum multistability is not affected by the different nature of the inner classical orbit, because still a second simple periodic orbit at larger amplitude exists such that oscillations can be observed after the quantum trajectories have left the inner orbit.

This is illustrated for case (d) in figs. 7, 8. First, we observe again that the relevant time scale changes significantly with σ. If σ is increased from 0.05 to 0.1 in fig. 7 almost all weight of the Wigner function is transferred from the inner to the outer orbit. Second, the Wigner functions themselves look quite similar to those for case (a) in fig. 3. In agreement with this, well-defined oscillations are observed in the cantilever position and autocorrelation function in fig. 8, and the respective amplitudes can be related to those of the classical orbits in fig. 1.

The present data might suggest a more ambitious interpretation. Apparently, all curves at finite σ in fig. 8 show simple periodic oscillations even if (at $\sigma = 0.05$) most weight in the Wigner function is still on the inner —classically chaotic— orbit. To a certain extent, quantum mechanics protects the optomechanical system against classical chaotic dynamics. Initially, the quantum state cannot follow the intricate chaotic orbit curve because it occupies a finite part of phase space. Because of phase space averaging, the chaotic motion is replaced by simple oscillations at the fundamental system (*i.e.*, cantilever) frequency. Later, the quantum trajectories move to the second —classically simple periodic— orbit. At all times, the chaotic classical dynamics is replaced by clearly defined simple oscillations in the quantum regime. Notice that we here discuss possible signatures of classical chaos in the associated dissipative quantum dynamics and not in quantities such as the level statistics that are defined for conservative Hamiltonian systems only [25,26].

Conclusions. – In this paper we establish the quantum-mechanical counterpart of the classical multistability of optomechanical systems. While classical multistability corresponds to the coexistence of self-sustained oscillations at multiple amplitudes, quantum multistability is a dynamical effect in which the amplitude of oscillations changes over time. The change can be detected with phase space techniques such as the Wigner function, and analyzed quantitatively with autocorrelation functions.

Quantum multistability is observed close to the classical limit. There, the quantum trajectories in the QSD picture of dissipative dynamics are well localized in phase space. Quantum multistability results from corrections to the classical dynamics given by the noise terms in the stochastic QSD equations of motion. The picture of quantum trajectories also provides the link between the oscillatory quantum dynamics and the classical orbits such that, *e.g.*, the oscillations in the autocorrelation functions can be traced back to the classical self-sustained oscillations.

The time scale relevant for quantum multistability is set by the quantum-classical scaling parameter σ. An interesting goal is to obtain the time scale from the QSD equations by quantifying the size of the noise term. This is not an entirely trivial task, though, because the noise term depends not directly on σ but on the deviation of the quantum trajectory state from a coherent state.

An important aspect for experimental investigations of quantum multistability is the robustness of the feature. Quantum multistability manifests itself over an extended period of time, is observable in autocorrelation functions after the initial dynamics has evolved into a stable dynamical pattern, and does not require specific system preparations. The experimental feasibility depends mainly on the ability to tune the quantum-classical scaling parameter σ. For the prototypical cantilever-cavity system σ is changed, *e.g.*, by simultaneous adjustment of the cantilever mass and pump laser power (thus preserving the self-sustained oscillations). The central experimental challenge is to distinguish "quantum" multistability from the effects of "classical" thermal noise, which requires that the temperature be sufficiently low. The relevant dynamical energies are larger than the energy separation of low-lying quantum states, which allows for comparatively high temperatures. Furthermore, variation of σ changes the quantum-mechanical time scale while the thermal noise is not affected. This might open up the possibility of observing the crossover from classical to quantum mechanics directly in the dynamical behaviour of an optomechanical system.

* * *

This work was supported by Deutsche Forschungsgemeinschaft via Sonderforschungsbereich 652 (project B5).

REFERENCES

[1] Kippenberg T. J. and Vahala K. J., *Science*, **321** (2008) 1172.

[2] Marquardt F. and Girvin S. M., *Physics*, **2** (2009) 40.

[3] Meystre P., *Ann. Phys. (Berlin)*, **525** (2013) 215.

[4] Aspelmeyer M., Kippenberg T. J. and Marquardt F., *Rev. Mod. Phys.*, **86** (2014) 1391.

[5] Marquardt F., Harris J. G. E. and Girvin S. M., *Phys. Rev. Lett.*, **96** (2006) 103901.

[6] Ludwig M., Kubala B. and Marquardt F., *New J. Phys.*, **10** (2008) 095013.

[7] Kippenberg T. J., Rokhsari H., Carmon T., Scherer A. and Vahala K. J., *Phys. Rev. Lett.*, **95** (2005) 033901.

[8] Rokhsari H., Kippenberg T. H., Carmon T. and Vahala K. J., *Opt. Express*, **13** (2005) 5293.

[9] Carmon T., Rokhsari H., Yang L., Kippenberg T. J. and Vahala K. J., *Phys. Rev. Lett.*, **94** (2005) 223902.

[10] Carmon T., Cross M. C. and Vahala K. J., *Phys. Rev. Lett.*, **98** (2007) 167203.

[11] Bakemeier L., Alvermann A. and Fehske H., *Phys. Rev. Lett.*, **114** (2015) 013601.

[12] Chan J., Alegre T. P. M., Safavi-Naeini A. H., Hill J. T., Krause A., Groblacher S., Aspelmeyer M. and Painter O., *Nature*, **478** (2011) 89.

[13] Teufel J. D., Donner T., Li D., Harlow J. W., Allman M. S., Cicak K., Sirois A. J., Whittaker J. D., Lehnert K. W. and Simmonds R. W., *Nature*, **475** (2011) 359.

[14] Hertzberg J. B., Rocheleau T., Ndukum T., Savva M., Clerk A. A. and Schwab K. C., *Nat. Phys.*, **6** (2010) 213.

[15] Vanner M. R., Hofer J., Cole G. D. and Aspelmeyer M., *Nat. Commun.*, **4** (2013) 2295.

[16] Suh J., Weinstein A. J., Lei C. U., Wollman E. E., Steinke S. K., Meystre P., Clerk A. A. and Schwab K. C., *Science*, **344** (2014) 1262.

[17] Law C. K., *Phys. Rev. A*, **51** (1995) 2537.

[18] Carmichael H. J., *Statistical Methods in Quantum Optics 1* (Springer) 1999.

[19] Schleich W. P., *Quantum Optics in Phase Space* (Wiley-VCH) 2001.

[20] Gisin N. and Percival I. C., *J. Phys. A*, **25** (1992) 5677.

[21] Schack R. and Brun T. A., *Comput. Phys. Commun.*, **102** (1997) 210.

[22] Percival I. C., *J. Phys. A*, **27** (1994) 1003.

[23] Schack R., Brun T. A. and Percival I. C., *J. Phys. A: Math. Gen.*, **28** (1995) 5401.

[24] Rigo M. and Gisin N., *Quantum Semiclass. Opt.*, **8** (1996) 255.

[25] Gutzwiller M. C., *Chaos in Classical and Quantum Mechanics* (Springer, New York) 1990.

[26] Haake F., *Quantum Signatures of Chaos* (Springer, Berlin) 2010.

PHYSICAL REVIEW A **94**, 063860 (2016)

Symmetry-breaking oscillations in membrane optomechanics

C. Wurl, A. Alvermann,* and H. Fehske
Institut für Physik, Ernst-Moritz-Arndt-Universität Greifswald, 17487 Greifswald, Germany
(Received 16 September 2016; published 29 December 2016)

We study the classical dynamics of a membrane inside a cavity in the situation where this optomechanical system possesses a reflection symmetry. Symmetry breaking occurs through supercritical and subcritical pitchfork bifurcations of the static fixed-point solutions. Both bifurcations can be observed through variation of the laser-cavity detuning, which gives rise to a boomerang-like fixed-point pattern with hysteresis. The symmetry-breaking fixed points evolve into self-sustained oscillations when the laser intensity is increased. In addition to the analysis of the accompanying Hopf bifurcations we describe these oscillations at finite amplitudes with an ansatz that fully accounts for the frequency shift relative to the natural membrane frequency. We complete our study by following the route to chaos for the membrane dynamics.

DOI: 10.1103/PhysRevA.94.063860

I. INTRODUCTION

Optomechanical systems [1–4] show a variety of dynamical patterns in the classical and quantum regimes [5,6]. Several aspects of the classical nonlinear dynamics of these systems have been studied theoretically and observed experimentally, including self-sustained oscillations [7–10], multistability and hysteresis [11], and chaotic [12–14] behavior.

A different line of inquiry concerns the modification of the classical dynamics due to quantum effects [15]. The general correspondence between the classical and quantum dynamics of optomechanical systems and the specific fate of self-sustained oscillations under the influence of quantum noise [16] and phase space diffusion [17] have been addressed in recent studies [18–20]. These studies require a clear picture of the classical dynamical patterns to be able to identify the influence of quantum effects.

In order to contribute to this picture we address in this paper the nonlinear dynamics of a membrane inside a cavity (see Fig. 1), with a focus on the self-sustained oscillations that break the reflection symmetry of the specific setup considered here. Our work is motivated by previous studies of similar setups that addressed, e.g., the symmetry breaking at zero detuning [21], the onset of chaotic motion [22], or pattern formation and buckling phase transitions for a flexible membrane [23,24]. We extend these studies along three lines. First, we analyze the pitchfork and saddle-node bifurcations related to symmetry breaking and hysteresis, which leads to a clear characterization of the different transitions between the symmetric and nonsymmetric situation. Second, we establish a scaling relation for the bifurcations and fixed-point solutions that allows for tuning the symmetry-breaking transitions to different parameter regimes. Third, we introduce a new ansatz for the self-sustained membrane oscillations and develop an intuitive physical picture of symmetry-breaking oscillations that is based on the power balance between optical and mechanical degrees of freedom associated with this ansatz. These results should help to observe static and dynamical symmetry breaking in future experiments. The close relation between our theoretical findings and the actual experiment is established by the translation rules between model and real physical parameters given below.

One specific result of our study with potential experimental relevance is that the frequency of the self-sustained oscillations is shifted significantly relative to the natural membrane frequency. This is in contrast to the cantilever-cavity system with one photon mode, where self-sustained oscillations occur approximately at the cantilever frequency [10]. The frequency shift, which can be determined experimentally from the position of the optical sidebands, contains additional information about system parameters such as the membrane stiffness. At least in principle, mechanical parameters could thus be obtained from optical frequency measurements.

II. THEORETICAL SETUP

The symmetric membrane-in-the-middle setup considered here consists of a membrane with high reflectivity placed near the cavity center (see Fig. 1). Two degenerate photon modes in the left and right halves of the cavity contribute equally to the radiation pressure acting on the membrane. Photon tunneling through the membrane connects both photon modes, lifts their degeneracy, and results in a quadratic dispersion of the optical modes as a function of the membrane position [25–28].

For the theoretical analysis of this situation it is convenient to work with dimensionless quantities (see Appendix A for a summary), especially to measure time in units of the inverse membrane frequency (Ω^{-1}). Then, the classical equations of motion read

$$\dot{x} = p, \tag{1a}$$

$$\dot{p} = -x - \Gamma p - g(|a_\mathrm{L}|^2 - |a_\mathrm{R}|^2), \tag{1b}$$

$$\dot{a}_\mathrm{L} = [i\Delta - ix - \kappa]a_\mathrm{L} - iJa_\mathrm{R} - i, \tag{1c}$$

$$\dot{a}_\mathrm{R} = [i\Delta + ix - \kappa]a_\mathrm{R} - iJa_\mathrm{L} - i, \tag{1d}$$

for the membrane position (x) and momentum (p) and the photon field amplitudes in the left (a_L) and right (a_R) cavities. These equations contain five dimensionless parameters: the laser-cavity detuning $\Delta = (\Omega_\mathrm{las} - \Omega_\mathrm{cav})/\Omega$, cavity decay rate $\kappa = \pi c/(2FL\Omega)$, mechanical damping $\Gamma = 1/Q_\mathrm{m}$, membrane transmissivity $J = \mathrm{e}^{i\varphi}\sqrt{2(1-r)}(c/L)/\Omega$, and effective radiation pressure $g = (\pi c\,\Omega_\mathrm{cav}P)/(m\Omega^5 L^3 F)$. These

*Corresponding author: alvermann@physik.uni-greifswald.de

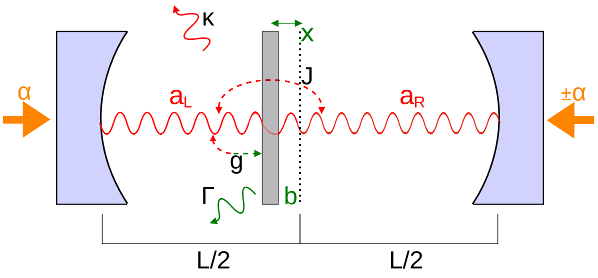

FIG. 1. The membrane-in-the-middle setup consists of a vibrating, partially reflective membrane placed in the center of a cavity, which is pumped by an external laser through the left and right mirrors with equal intensities.

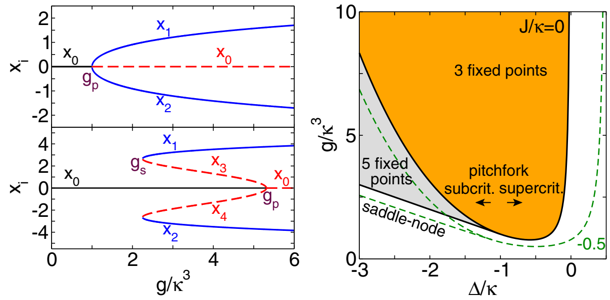

FIG. 2. Left panel: Supercritical pitchfork bifurcation for small detuning (upper plot, for $\Delta/\kappa = 0$), and subcritical pitchfork and saddle-node bifurcation for large detuning (lower plot, for $\Delta/\kappa = -3$), both for $J/\kappa = -1$. Right panel: Diagram of bifurcations (at g_p and g_s) and number of fixed points in the g-Δ plane, for $J/\kappa = 0$. Small nonzero J/κ shifts, essentially, the boundary curves in the plane (see, e.g., the dashed curves for $J/\kappa = -0.5$). Nontrivial fixed points exist for $\Delta < -J$.

parameters are obtained from the physical parameters of the cavity (length L, frequency Ω_{cav}, finesse F), the membrane (frequency Ω, mass m, quality factor Q_{m}, reflectivity r), and the laser (frequency Ω_{las}, transmitted power P, phase difference φ) as specified here and in Appendix A.

Note that the above equations of motion are valid for a relative phase $e^{i\varphi} = \pm 1$ of the laser amplitude at the right and left mirror, with $J > 0$ ($J < 0$) for equal (opposite) phase. The laser power enters through the parameter g. For typical experimental setups from the literature [4], we have $g \lesssim 10$ with significant optical losses ($\kappa \simeq 1$) and small mechanical damping ($\Gamma \simeq 10^{-4} \ll 1$). Since the effective optomechanical coupling g can be adjusted via the laser power, different experimental implementations are conceivable to achieve sufficiently large values of g. In the optomechanical setup in Ref. [25], for example, a pump power on the order of $P \sim 10^{-8}$ W is required if the cavity is driven with laser light with frequency $\Omega_{\text{las}}/2\pi \sim 10^{14}$ Hz. However, possible experimental realizations depend on the availability of highly reflective membranes with very small J.

We now study the fixed-point bifurcations related to symmetry breaking (Sec. III), the Hopf bifurcations leading to self-sustained oscillations and the properties of these oscillations at finite amplitudes (Sec. IV), before we follow the route to chaos (Sec. V) and conclude immediately thereafter (Sec. VI). The appendices collect additional information on the derivation of the dimensionless equations of motion (Appendix A), the stability analysis (Appendix B), and the finite amplitude ansatz (Appendix C).

III. SYMMETRY BREAKING

The equations of motion (1) are invariant under the replacement $x \mapsto -x$ (with $p \mapsto -p$ and swapping $a_{L/R} \mapsto a_{R/L}$), which defines the reflection symmetry of the system with respect to the membrane position. The symmetry implies the existence of a trivial fixed point $x_0 = 0$, while symmetry breaking results in additional nontrivial fixed points $\pm x_i \neq 0$.

The fixed points are obtained from Eq. (1) as the solutions with $\dot{x} = \dot{p} = \dot{a}_{\text{L}} = \dot{a}_{\text{R}} = 0$. Four nontrivial fixed points can exist in addition to $x_0 = 0$, namely,

$$x_{1/2} = \pm\sqrt{-\gamma + 2\sqrt{f}}, \tag{2a}$$

$$x_{3/4} = \pm\sqrt{-\gamma - 2\sqrt{f}}, \tag{2b}$$

where $\gamma = \kappa^2 + J^2 - \Delta^2$ and $f = -\Delta^2\kappa^2 - g(\Delta + J)$. These fixed points exist if the respective terms under the square root are non-negative. As a consequence of the reflection symmetry they occur in pairs $\pm x_i$ with opposite sign. The corresponding values for $a_{L/R}$ are

$$a_{\text{L/R}} = \frac{\Delta \pm x + i\kappa + J}{(i\Delta - \kappa)^2 + x^2 + J^2} \tag{3}$$

for all fixed points, with the $+$ ($-$) sign for a_L (a_R).

A. Pitchfork bifurcation

As g is increased, the nontrivial fixed points appear through a pitchfork bifurcation at

$$g_p = -\frac{\Delta^2\kappa^2}{\Delta + J} - \frac{1}{4}\frac{(\kappa^2 + J^2 - \Delta^2)^2}{\Delta + J}. \tag{4}$$

For small detuning $|\Delta| \leqslant \sqrt{\kappa^2 + J^2}$ the bifurcation at g_p is a supercritical pitchfork bifurcation (see Fig. 2, left panel, upper plot). For $g < g_p$ only the trivial fixed point $x_0 = 0$ exists. For $g > g_p$, the trivial fixed point becomes unstable and the two stable fixed points x_1, x_2 appear. For large detuning $|\Delta| \geqslant \sqrt{\kappa^2 + J^2}$ the bifurcation at g_p is a subcritical pitchfork bifurcation (see Fig. 2, left panel, lower plot), where the two unstable fixed points x_3, x_4 exist together with the stable trivial fixed point x_0 for $g < g_p$. The pitchfork bifurcation is accompanied by a saddle-node bifurcation at

$$g_s = -\frac{\Delta^2\kappa^2}{\Delta + J}, \tag{5}$$

which connects the unstable fixed points x_3, x_4 to the two stable fixed points x_1, x_2. For $g_s < g < g_p$ all five fixed points coexist.

B. Scaling

Equations (2)–(5) are invariant under the scaling $\Delta \mapsto s\Delta$, $J \mapsto sJ$, $\kappa \mapsto s\kappa$, $x \mapsto sx$, $a_{L/R} \mapsto (1/s)a_{L/R}$, $g_i \mapsto s^3 g_i$, for any $s > 0$. Therefore, the positions of the fixed points

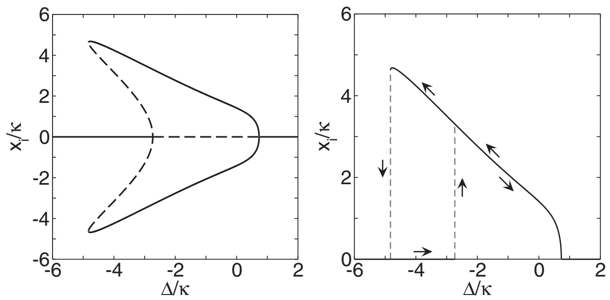

FIG. 3. Left panel: Boomerang fixed-point pattern as a function of Δ, for fixed $g/\kappa^3 = 4$, $J/\kappa = -1$. Right panel: Hysteresis of fixed points for cyclic change of Δ/κ. The stable (solid curves) and unstable (dashed curves) fixed points as drawn here are obtained for small g (i.e., small scaling parameter s). At larger g, fixed points can lose stability through Hopf bifurcations (cf. Sec. IV).

depend only on the appropriate ratios, e.g., J/κ, Δ/κ, and g/κ^3. The stability of the fixed points, however, depends on the absolute values of the system parameters and changes with s (see Sec. IV). The occurrence of nontrivial fixed points is summarized in Fig. 2.

Note that for $\Delta = 0$ only the supercritical pitchfork bifurcation occurs. In this situation symmetry breaking is formally related to the super-radiant phase transition in the Dicke model [21].

C. Boomerang pattern

Changing the laser-cavity detuning Δ instead of the effective radiation pressure g allows for observation of the supercritical and subcritical pitchfork bifurcation in succession (see Fig. 3, left panel). The saddle-node bifurcation in the resulting boomerang-like fixed point pattern can be observed through the hysteresis that occurs when Δ is changed along a cycle (see Fig. 3, right panel).

IV. SELF-SUSTAINED OSCILLATIONS

A. Hopf bifurcations

In the vicinity of the pitchfork and saddle-node bifurcations the stability of fixed points changes according to the type of the bifurcation. Away from the fixed-point bifurcations additional dynamical Hopf bifurcations can occur, through which potentially stable fixed points are replaced by oscillatory orbits.

The stability of the fixed points is determined by the stability matrix that is obtained from linearization of the equations of motion (see Appendix B for explicit expressions). Figure 4 shows the stability of fixed points according to the linear analysis for the supercritical and subcritical pitchfork bifurcation. Note that the stability changes under the s scaling that leaves the fixed points invariant, such that we have to specify the absolute value of, e.g., κ in Fig. 4.

Figure 5 shows the real part of the eigenvalues of the stability matrix, following the fixed points $x_0 \to x_1$ through the supercritical pitchfork bifurcation at small $|\Delta|$. In the vicinity of g_p we observe how one real eigenvalue touches

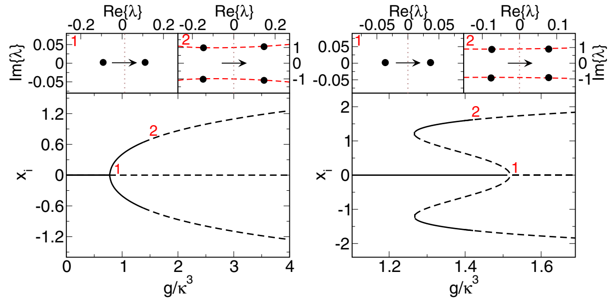

FIG. 4. Stability characteristics for the supercritical (left panel, $\Delta/\kappa = 0$) and subcritical (right panel, $\Delta/\kappa = -1.65$) pitchfork bifurcation, for $J/\kappa = -0.5$ and $\kappa = 1$. Stable (unstable) fixed points are plotted as solid (dashed) curves. The red numbers indicate the pitchfork (1) and Hopf bifurcations (2), which can be distinguished by the number of eigenvalues of the stability matrix that cross the imaginary axis (upper panels).

the imaginary axis ($\mathrm{Re}\,\lambda = 0$) at the bifurcation. At a certain value $g > g_p$ a pair of complex conjugate eigenvalues (λ, λ^*) crosses the imaginary axis, and a (supercritical) Hopf bifurcation takes place. The frequency of the oscillations that appear immediately after the Hopf bifurcation is given by the imaginary parts of the eigenvalue pair.

The position of the Hopf bifurcation and the oscillation frequency depend on the absolute parameter values, not only the ratios J/κ etc., and thus change under the s scaling that leaves the fixed point pattern invariant. Figure 5 shows both quantities as a function of the absolute parameter values. We note the significant shift of the oscillation frequency relative to the natural membrane frequency ($\omega = 1$) that occurs for some parameter combinations.

B. Finite amplitude ansatz

Close to the Hopf bifurcation, for small amplitudes, the frequency of the self-sustained oscillations follow from the local analysis of the equations of motion via the stability matrix

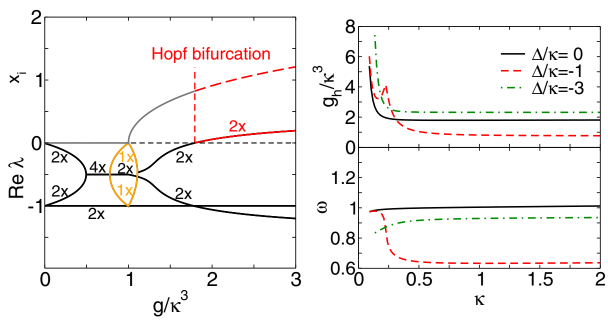

FIG. 5. Left panel: Real part of the six eigenvalues of the stability matrix across the pitchfork bifurcation, for $\Delta/\kappa = 0$, $J/\kappa = -1$ as in Fig. 2, and $\kappa = 1$. Small numbers indicate the multiplicity of the eigenvalues. At $g \approx 1.79$ the fixed point x_1 loses stability through a Hopf bifurcation. Right panel: Position of the Hopf bifurcation (g_h) and frequency of the small amplitude oscillations (ω) as a function of the absolute value of κ, for $\Delta/\kappa = 0, -1, -3$.

just presented. We now develop an analytical description to understand the properties of the self-sustained oscillations also at finite amplitudes, away from the Hopf bifurcation.

The starting point is the ansatz

$$x(t) = x_c + A\cos(\omega t + \vartheta) \tag{6}$$

for a simple periodic membrane oscillation at amplitude A. In contrast to the ansatz for the cantilever-cavity system with one-photon mode [10,11], where self-sustained oscillations occur at the natural cantilever frequency, the oscillation frequency ω has to be included as a parameter in our ansatz, because in general $\omega \neq 1$ already in the vicinity of the Hopf bifurcation. The phase angle ϑ is arbitrary and set to $\vartheta = 0$.

With the periodic ansatz (6) for the membrane position also the optical modes follow a periodic motion, but additional sidebands at multiples of ω occur. From the equations of motion (1c) and (1d) we obtain the Fourier series

$$a_L(t) = e^{-i(A/\omega)\sin\omega t} \sum_{n=-\infty}^{\infty} a_L^n e^{in\omega t},$$

$$a_R(t) = e^{+i(A/\omega)\sin\omega t} \sum_{n=-\infty}^{\infty} a_R^n e^{in\omega t}, \tag{7}$$

where the Fourier coefficients fulfill

$$a_L^n = \frac{\hat{J}_n\left(\frac{A}{\omega}\right) + J\sum_{m\neq 0} \hat{J}_{n-m}\left(2\frac{A}{\omega}\right) a_R^m}{\Delta - x_c - n\omega + i\kappa}, \tag{8a}$$

$$a_R^n = \frac{\hat{J}_n\left(-\frac{A}{\omega}\right) + J\sum_{m\neq 0} \hat{J}_{n-m}\left(-2\frac{A}{\omega}\right) a_L^m}{\Delta + x_c - n\omega + i\kappa} \tag{8b}$$

(see Appendix C for the derivation). For $J = 0$ both equations decouple and directly give the Fourier coefficients in terms of the Bessel functions $\hat{J}_n(\cdot)$, but for $J \neq 0$ a coupled system of linear equations has to be solved. For small $|J|$ this can be done iteratively.

To determine the parameters x_c, A, ω in the ansatz we have to insert Eqs. (6) and (7) into the first two equations of motion (1a) and (1b), which gives the conditions

$$x_c = -g\sum_m \left|a_L^m\right|^2 - \left|a_R^m\right|^2, \tag{9a}$$

$$\Gamma\omega A = -2g\,\mathrm{Im}\sum_m a_L^{m*}a_L^{m-1} - a_R^{m*}a_R^{m-1}, \tag{9b}$$

$$A(1-\omega^2) = -2g\,\mathrm{Re}\sum_m a_L^{m*}a_L^{m-1} - a_R^{m*}a_R^{m-1}. \tag{9c}$$

The first condition follows from comparison of the Fourier mode $n = 0$ on both sides of the equations; the other two conditions follow for the Fourier modes $n = \pm 1$. The contribution of the higher Fourier modes to the membrane motion is negligible within the limits of validity of the ansatz, and they do not give additional conditions.

For an intuitive physical interpretation of the three conditions (9) we note that Eqs. (1a) and (1b) are equations of motion of a driven harmonic oscillator, where the driving force is the radiation pressure ($\propto g$). In this picture, Eq. (9a) is a condition on the vanishing of the net force acting on the oscillator over one oscillation period, which can be written

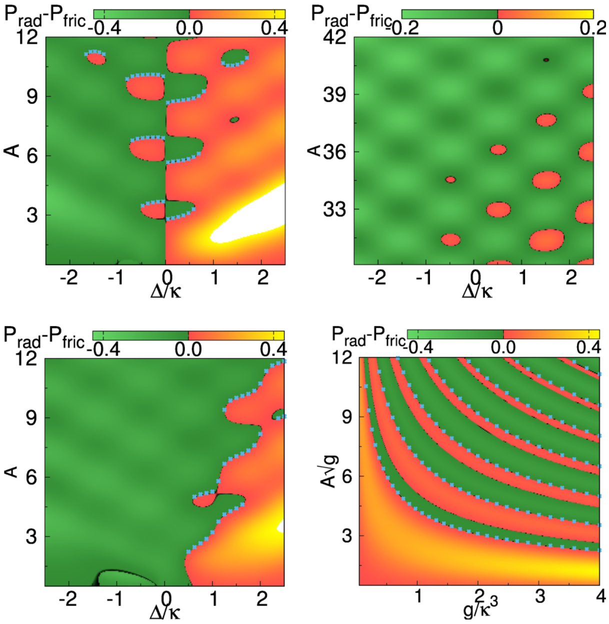

FIG. 6. Power balance $\mathcal{P} \sim \mathcal{P}_{\mathrm{rad}} - \mathcal{P}_{\mathrm{fric}}$ as a function of the oscillation amplitude A and Δ/κ ($g/\kappa^3 = 1$) or g/κ^3 ($\Delta/\kappa = 1.4$), respectively, for $J/\kappa = 0$ (upper plots) and $J/\kappa = -0.5$ (lower plots) with $\kappa = 1$. Stable periodic orbits obtained from the numerical solution of Eq. (1) are included as blue dots.

as $0 = \int_t^{t+2\pi/\omega} \dot{p}(t')dt'$. Condition (9b) is a condition on the vanishing of the net change of the oscillator energy $E = (x^2 + p^2)/2$ over one oscillation period, which can be written as $0 = \delta E = \int_t^{t+2\pi/\omega} x(t')\dot{x}(t') + p(t')\dot{p}(t')dt'$. This allows us to interpret Eq. (9b) as the power balance

$$\mathcal{P} = \mathcal{P}_{\mathrm{rad}} - \mathcal{P}_{\mathrm{fric}} \tag{10}$$

between the energy gain from the radiation pressure acting on the membrane $\mathcal{P}_{\mathrm{rad}} = -g\omega A\,\mathrm{Im}\sum_m a_L^{m*}a_L^{m-1} - a_R^{m*}a_R^{m-1}$ and the average energy loss due to friction $\mathcal{P}_{\mathrm{fric}} = \Gamma\omega^2 A^2/2$. These first two conditions are equivalent to those introduced in Ref. [10] for the optomechanical system with one photon mode.

The third new condition (9c) can be interpreted as a condition on the net phase shift per oscillation period, i.e., as the condition that ϑ is constant in Eq. (6). It can be written as $0 = \int_t^{t+2\pi/\omega}[x(t') - x_c]\dot{p}(t') + \dot{x}(t')p(t')dt'$. This condition allows us to determine the oscillation frequency ω in the ansatz. It would be missing if we considered a simpler ansatz with fixed $\omega = 1$.

The power balance $\mathcal{P}$ is plotted in Fig. 6. For these plots, the oscillation shift x_c and frequency ω have been determined from the conditions (9a) and (9c), and then the power balance $\mathcal{P}$ is computed as a function of the remaining free parameter in the ansatz, the oscillation amplitude A. Periodic solutions exist if condition (9b) is fulfilled, i.e., for $\mathcal{P} = 0$. Stable orbits exist if the frictional losses increase with the amplitude, i.e., for $d\mathcal{P}/dA < 0$.

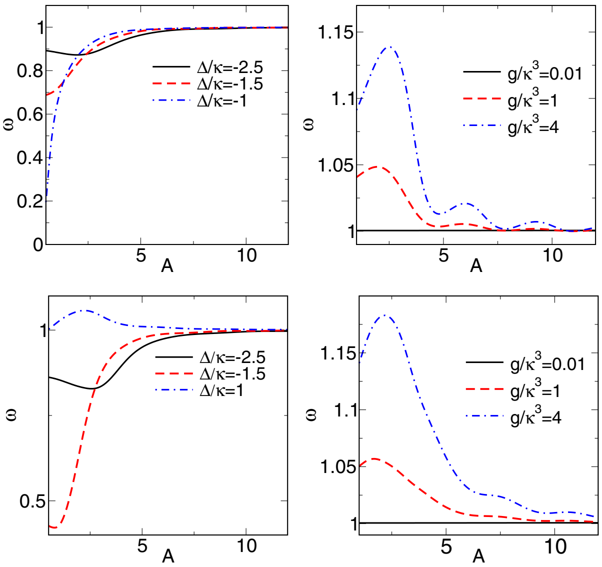

FIG. 7. Oscillation frequency ω calculated from Eqs. (9) as a function of the oscillation amplitude A for $g/\kappa^3 = 1$ (top/bottom left), $\Delta/\kappa = 0.5$ (top right) and $\Delta/\kappa = 1.4$ (bottom right) with $\kappa = 1$, corresponding to the previous figure (upper plots: $J/\kappa = 0$, lower plots: $J/\kappa = -0.5$).

C. Multistability

For each set of system parameters, i.e., moving parallel to the vertical axis in Fig. 6, multiple solutions with $P = 0$ can be found from the ansatz. Among these, the solutions with $d\mathcal{P}/dA < 0$ correspond to stable orbits obtained from numerical solution of the equations of motion (1) (blue dots in Fig. 6). Our ansatz thus correctly predicts the the coexistence of multiple stable periodic orbits at different amplitudes, i.e., the multistability of self-sustained oscillations in the membrane-in-the-middle setup.

D. Frequency renormalization

For most parameter combinations the oscillation frequency is shifted significantly relative to the natural membrane frequency (see Fig. 7), as we noted previously during the analysis of the Hopf bifurcations. Allowing for $\omega \neq 1$ is crucial to obtain the correct solutions from the ansatz, while a simpler ansatz with fixed $\omega = 1$ would fail (see Fig. 8). Since the oscillation frequency ω appears in Eq. (7) for the optical modes it can be observed directly in the optical spectrum (see Fig. 8), which allows for an experimental measurement.

V. ROUTE TO CHAOS

Starting from the self-sustained oscillations the entire route to chaos in optomechanical systems [13] can be observed also for the membrane-in-the-middle setup. Figure 9 shows the Feigenbaum cascade of period doubling bifurcations that lead to chaos, starting from the nontrivial fixed point x_1 after the supercritical pitchfork bifurcation (cf. Fig. 2). The sequence of period doubling bifurcations can be observed through the appearance of additional sidebands in the optical spectrum

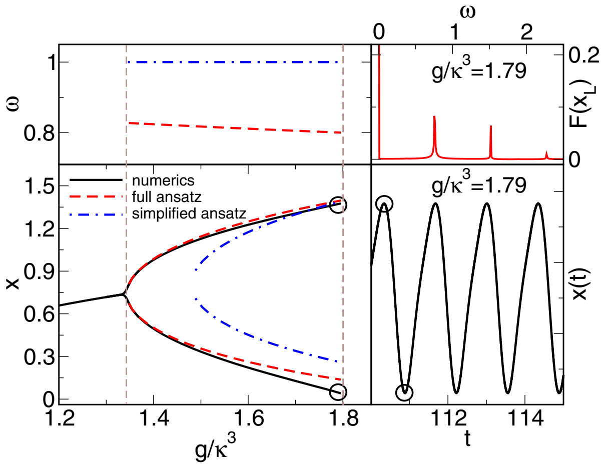

FIG. 8. Left panel: Maximal and minimal oscillation amplitude $x = x_c \pm A$ obtained with the ansatz (6) from Eqs. (9) (dashed red curve) in comparison to values obtained from direct solution of the equations of motion (1) (solid black curve), for $J/\kappa = 0$, $\Delta/\kappa = -0.5$, and $\kappa = 1$. The upper panel shows the deviation of the oscillation frequency from the bare membrane frequency ($\omega \neq 1$). Also included are the wrong results obtained with a simplified ansatz with fixed $\omega = 1$ (dot-dashed blue curves). Right panel: Cantilever position $x(t)$ (bottom) and the optical spectrum of the left photon mode (top) for $g = 1.79$, corresponding to the solution in the left panels (circles).

(see upper panels in Fig. 9). Intricate patterns of intertwined regular and chaotic motion replace the fixed point patterns at a larger scale, as shown in Fig. 10 for the supercritical pitchfork bifurcation and the boomerang pattern. It will probably be

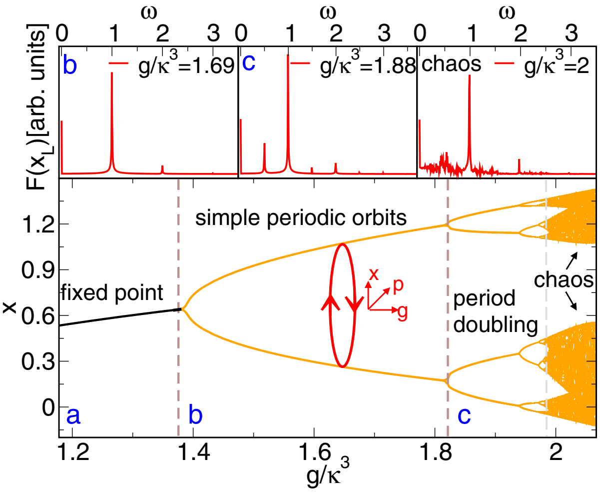

FIG. 9. Feigenbaum diagram starting at the upper fixed point after the supercritical pitchfork bifurcation for $\Delta/\kappa = 0$, $J/\kappa = -0.5$, and $\kappa = 1$. Proceeding from fixed points (regime a) via simple oscillations (regime b) and period doublings (regime c) finally results in chaos. The different dynamical regimes can be distinguished in the optical spectrum (upper panels, for the left cavity mode).

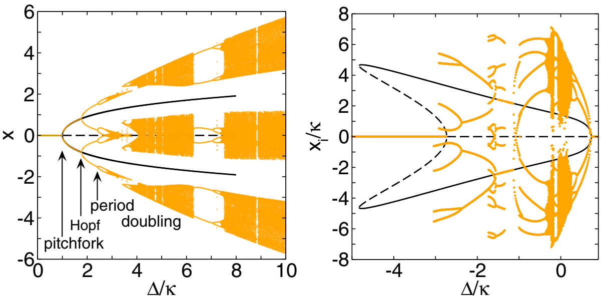

FIG. 10. Left panel: Evolution of chaos for small detuning, for $\Delta/\kappa = 0$, $J/\kappa = -1$, $\kappa = 1$ as in Fig. 5. Right panel: Chaos in the boomerang, for $g/\kappa^3 = 4$, $J/\kappa = -1$ as in Fig. 3, and $\kappa = 0.2$.

hard to resolve details of these features in the experiment, but it should be possible to measure the position of the first few bifurcations accurately.

VI. CONCLUSIONS

A membrane inside a cavity with reflection symmetry shows a variety of fixed-point bifurcations related to symmetry breaking. In addition to symmetry breaking, self-sustained oscillations appear for sufficient laser power. We here analyze the Hopf bifurcations that lead to their existence and describe their properties with a physically motivated ansatz for finite amplitude oscillations. The ansatz extends the results obtained for the cantilever-cavity system with one optical mode [10,11] to the situation of two coupled optical modes and to oscillations with variable frequency. The ansatz equations allow for an intuitive interpretation in physical terms, and especially the power balance proves useful for the prediction of the oscillation amplitudes and frequencies.

In contrast to the cantilever-cavity system the frequency of the self-sustained oscillations observed here differs from the natural mechanical (i.e., membrane) frequency. An interesting promise for future experiments is the indirect measurement of mechanical system parameters, e.g., the membrane stiffness, from the sidebands in the optical spectrum whose position is determined by the frequency shift. However, a major challenge for the experimental realization of the situation considered in this paper is to achieve the regime of high membrane reflectivity, i.e., small J.

In the present paper we focus specifically on the classical dynamics resulting from symmetry-breaking bifurcations. Certainly, the results reported here are only part of the broader picture of the dynamics of the membrane-in-the-middle system. The principal theoretical contribution of this work, our ansatz for the self-sustained oscillations, can be adapted to larger values of J, where the full dispersion of the cavity modes has to be taken into account, and also to situations without symmetry breaking, where the membrane is not placed in the cavity center. Based on a modified ansatz the present analysis extends to these scenarios, where dynamical patterns similar to those discussed here can be observed and which may be more easily realized in the experiment. These extensions should be addressed in a future study. A more speculative line of thought is to ask for the influence of quantum effects, such as the breaking of symmetry due to quantum fluctuations and noise, and the ensuing modifications of the classical bifurcations.

ACKNOWLEDGMENTS

The authors are grateful to B. Bruhn and L. Bakemeier for discussions leading to the research reported in this work. This work was financed by Deutsche Forschungsgemeinschaft through SFB 652 (Project No. B5).

APPENDIX A: DERIVATION OF THE DIMENSIONLESS EQUATIONS OF MOTION

We here summarize the relation between the standard equations of motion for the membrane-in-the-middle setup (cf. Fig. 1) given, e.g., in Ref. [26], and our dimensionless Eqs. (1). Note that we require only the classical equations of motion. The corresponding Hamiltonian can be constructed according to, e.g., Refs. [29,30].

The equations of motion for the photon amplitudes in the left (a_l) and right (a_r) half of the cavity, in a reference frame rotating with the laser frequency, have the form

$$\dot{a}_{\mathrm{L}} = [i\Delta - iGx - \kappa]a_{\mathrm{L}} - iJa_{\mathrm{R}} - \quad i\alpha, \qquad \text{(A1a)}$$

$$\dot{a}_{\mathrm{R}} = [i\Delta + iGx - \kappa]a_{\mathrm{R}} - iJa_{\mathrm{L}} - \sigma i\alpha, \qquad \text{(A1b)}$$

where $\Delta = \Omega_{\mathrm{las}} - \Omega_{\mathrm{cav}}$ is the detuning between the laser frequency Ω_{las} and the cavity frequency $\Omega_{\mathrm{cav}} = n(2\pi c)/(L/2)$ (for the nth optical mode), and κ the cavity decay rate. In the units chosen here, $|a_{L/R}|^2$ is the number of photons, and $\hbar\Omega_{\mathrm{cav}}|a_{L/R}|^2$ is the energy per optical mode. $G = -\partial\Omega_{\mathrm{cav}}/\partial x = \Omega_{\mathrm{cav}}/(L/2)$ gives the change of the optical frequency with membrane position x in the linear regime of small x, which also determines the radiation pressure.

The parameter J, the membrane transmissivity, can be determined from comparison of the position of the optical resonances at $\pm\sqrt{J^2 + G^2x^2}$ (for $\kappa = 0$) to the quadratic dispersion near $x = 0$ obtained from Maxwell's equations [26]. Note that this treatment is valid only in the limit of small J.

The parameter α is related to the laser input power P transmitted into the cavity. Especially at resonance we have $|\alpha| = (\kappa P/(2\hbar\Omega_{\mathrm{cav}}))^{1/2}$, such that the energy per optical mode is $\hbar\Omega_{\mathrm{cav}}|\alpha/\kappa|^2 = P/(2\kappa)$, in accordance with the choice of κ as the amplitude decay rate. The phase difference φ between the laser in each half of the cavity is included through the factor $\sigma = e^{i\varphi}$. In the present symmetric setup we consider only phase differences $\varphi = \{0,\pi\}$, such that $\sigma = \pm 1$.

The equation of motion for the membrane position (x) has the form

$$\ddot{x}(t) = -\Omega^2 x(t) - \Gamma\dot{x}(t) - \hbar(G/m)(|a_L|^2 - |a_R|^2), \quad \text{(A2)}$$

with the membrane frequency Ω, mass m, mechanical damping Γ, and the radiation pressure $\propto G$.

To obtain the dimensionless Eqs. (1), we now set $\bar{x} = (G/\Omega)x$, $\bar{p} = (G/\Omega^2)\dot{x}$, $\bar{a}_{\mathrm{L}} = (\Omega/\alpha)a_{\mathrm{L}}$, $\bar{a}_{\mathrm{R}} = \sigma(\Omega/\alpha)a_{\mathrm{R}}$, measure time as $\bar{t} = \Omega t$, and define the dimensionless parameters $\bar{\Gamma} = \Gamma/\Omega$, $\bar{\kappa} = \kappa/\Omega$, $\bar{J} = \sigma J/\Omega$, $\bar{\Delta} = \Delta/\Omega$, $\bar{g} = 2\Omega_{\mathrm{cav}}\kappa P/(m\Omega^5 L^2)$. The relation between the dimensionless model parameters and the physical setup parameters is summarized after Eq. (1). Note that $\hbar$ cancels in these equations, as it must in the classical case. To simplify notation, the overline $\bar{}$ annotation is omitted in the main text.

APPENDIX B: FIXED POINT STABILITY

For the linear stability analysis we rewrite the equations of motion (1) in terms of the quadratures $x_{\rm L/R} = (1/2)(a_{\rm L/R} + a^*_{\rm L/R})$, $p_{\rm L/R} = (i/2)(a^*_{\rm L/R} - a_{\rm L/R})$ (defined without the usual factor $1/\sqrt{2}$) instead of the complex variables $a_{L/R}$. We then get the equations of motion

$$\dot{x} = p, \tag{B1a}$$
$$\dot{p} = -x - \Gamma p - g\left(x_{\rm L}^2 + p_{\rm L}^2 - x_{\rm R}^2 - p_{\rm R}^2\right), \tag{B1b}$$
$$\dot{x}_{\rm L} = -(\Delta - x)p_{\rm L} - \kappa x_{\rm L} + J p_{\rm R}, \tag{B1c}$$
$$\dot{p}_{\rm L} = (\Delta - x)x_{\rm L} - \kappa p_{\rm L} - J x_{\rm R} - 1, \tag{B1d}$$
$$\dot{x}_{\rm R} = -(\Delta + x)p_{\rm R} - \kappa x_{\rm R} + J p_{\rm L}, \tag{B1e}$$
$$\dot{p}_{\rm R} = (\Delta + x)x_{\rm R} - \kappa p_{\rm R} - J x_{\rm L} - 1, \tag{B1f}$$

for six real variables. The stability analysis of the fixed points requires the Jacobi matrix of the right-hand side of these equations, which is given by

$$\begin{pmatrix} 0 & 1 & 0 & 0 & 0 & 0 \\ -1 & -\Gamma & -2gx_L & -2gp_L & +2gx_R & +2gp_R \\ p_{\rm L} & 0 & -\kappa & -\Delta + x & 0 & J \\ -x_{\rm L} & 0 & \Delta - x & -\kappa & -J & 0 \\ -p_{\rm R} & 0 & 0 & J & -\kappa & -\Delta - x \\ x_{\rm R} & 0 & -J & 0 & \Delta + x & -\kappa \end{pmatrix} \tag{B2}$$

with the respective fixed point values inserted. For the quadratures, they are

$$x_{L/R} = \frac{(\Delta \pm x + J)(-\Delta^2 + \kappa^2 + x^2 + J^2) - 2\Delta\kappa^2}{(-\Delta^2 + \kappa^2 + x^2 + J^2)^2 + 4\Delta^2\kappa^2},$$
$$p_{L/R} = \frac{\kappa(-\Delta^2 + \kappa^2 + x^2 + J^2) + 2\Delta\kappa(\Delta \pm x + J)}{(-\Delta^2 + \kappa^2 + x^2 + J^2)^2 + 4\Delta^2\kappa^2}, \tag{B3}$$

with the plus (or minus) sign for x_L, p_L (or x_R, p_R).

APPENDIX C: FOURIER SERIES SOLUTION FOR THE FINITE AMPLITUDE ANSATZ

To solve the vector-valued linear differential equation

$$\dot{\mathbf{x}}(t) = (\mathbf{A} + f(t)\mathbf{B})\mathbf{x}(t) + \mathbf{c} \tag{C1}$$

we write the solutions as

$$\mathbf{x}(t) = e^{g(t)\mathbf{B}}\,\mathbf{y}(t), \tag{C2}$$

where $\dot{g}(t) = f(t)$. The vector $\mathbf{y}(t)$ has to fulfill the differential equation

$$\dot{\mathbf{y}}(t) = e^{-g(t)\mathbf{B}}\,\mathbf{A}\,e^{g(t)\mathbf{B}}\,\mathbf{y}(t) + e^{-g(t)\mathbf{B}}\mathbf{c}. \tag{C3}$$

Unless the matrices $\mathbf{A}$ and $\mathbf{B}$ commute, this is a differential equation with time-dependent parameters.

To proceed with the solution, assume that $f(t)$ is a periodic function without a constant term such that also $g(t)$ is periodic, say, $g(t + 2\pi/\omega) = g(t)$. Then, the Fourier expansions

$$e^{-g(t)\mathbf{B}}\,\mathbf{A}\,e^{g(t)\mathbf{B}} = \sum_n e^{in\omega t}\mathbf{X}_n,$$
$$e^{-g(t)\mathbf{B}}\mathbf{c} = \sum_n e^{in\omega t}\mathbf{c}_n \tag{C4}$$

give the equations

$$\mathbf{y}_n = \frac{1}{i\omega n - \mathbf{X}_0}\left(\mathbf{c}_n + \sum_{m\neq 0}\mathbf{X}_m\mathbf{y}_{n-m}\right) \tag{C5}$$

for the Fourier coefficients in the expansion

$$\mathbf{y}(t) = \sum_n e^{in\omega t}\mathbf{y}_n. \tag{C6}$$

Applied to the equations of motion (1c) and (1d), with

$$\mathbf{A} = \begin{pmatrix} i(\Delta - x_c) - \kappa & -iJ \\ -iJ & i(\Delta + x_c) - \kappa \end{pmatrix}, \tag{C7}$$
$$\mathbf{B} = \begin{pmatrix} -i & 0 \\ 0 & i \end{pmatrix}, \quad \mathbf{c} = \begin{pmatrix} -i \\ -i \end{pmatrix}, \tag{C8}$$

and $f(t) = A\cos\omega t$ according to the ansatz (6), we have

$$\mathbf{X}_0 = \begin{pmatrix} i(\Delta - x_c) - \kappa & 0 \\ 0 & i(\Delta + x_c) - \kappa \end{pmatrix}, \tag{C9}$$
$$\mathbf{X}_m = -iJ\begin{pmatrix} 0 & \hat{J}_n(2\frac{A}{\omega}) \\ \hat{J}_n(-2\frac{A}{\omega}) & 0 \end{pmatrix}, \tag{C10}$$
$$\mathbf{c}_n = -i\begin{pmatrix} \hat{J}_n(\frac{A}{\omega}) \\ \hat{J}_n(-\frac{A}{\omega}) \end{pmatrix}, \tag{C11}$$

with the help of the Jacobi-Anger expansion

$$e^{iz\sin\omega t} = \sum_{n=-\infty}^{\infty}\hat{J}_n(z)e^{in\omega t} \tag{C12}$$

for the Bessel functions $\hat{J}_n(\cdot)$, and thus obtain the Fourier coefficients in Eq. (8).

[1] T. J. Kippenberg and K. J. Vahala, Science **321**, 1172 (2008).
[2] F. Marquardt and S. M. Girvin, Physics **2**, 40 (2009).
[3] P. Meystre, Ann. Phys. (Berlin) **525**, 215 (2013).
[4] M. Aspelmeyer, T. J. Kippenberg, and F. Marquardt, Rev. Mod. Phys. **86**, 1391 (2014).
[5] G. Heinrich, J. G. E. Harris, and F. Marquardt, Phys. Rev. A **81**, 011801 (2010).
[6] H. Wu, G. Heinrich, and F. Marquardt, New J. Phys. **15**, 123022 (2013).
[7] H. Rokhsari, T. H. Kippenberg, T. Carmon, and K. J. Vahala, Opt. Express **13**, 5293 (2005).
[8] T. J. Kippenberg, H. Rokhsari, T. Carmon, A. Scherer, and K. J. Vahala, Phys. Rev. Lett. **95**, 033901 (2005).

[9] T. Carmon, H. Rokhsari, L. Yang, T. J. Kippenberg, and K. J. Vahala, Phys. Rev. Lett. **94**, 223902 (2005).
[10] F. Marquardt, J. G. E. Harris, and S. M. Girvin, Phys. Rev. Lett. **96**, 103901 (2006).
[11] M. Ludwig, B. Kubala, and F. Marquardt, New J. Phys. **10**, 095013 (2008).
[12] T. Carmon, M. C. Cross, and K. J. Vahala, Phys. Rev. Lett. **98**, 167203 (2007).
[13] L. Bakemeier, A. Alvermann, and H. Fehske, Phys. Rev. Lett. **114**, 013601 (2015).
[14] X.-Y. Lü, H. Jing, J.-Y. Ma, and Y. Wu, Phys. Rev. Lett. **114**, 253601 (2015).
[15] M. C. Gutzwiller, *Chaos in Classical and Quantum Mechanics* (Springer, Berlin, 1990).
[16] C. W. Gardiner and P. Zoller, *Quantum Noise* (Springer, Berlin, 2004).
[17] W. P. Schleich, *Quantum Optics in Phase Space* (Wiley-VCH, New York, 2001).
[18] F. Armata, L. Latmiral, I. Pikovski, M. R. Vanner, C. Brukner, and M. S. Kim, Phys. Rev. A **93**, 063862 (2016).
[19] G. Wang, Y.-C. Lai, and C. Grebogi, Sci. Rep. **6**, 35381 (2016).
[20] C. Schulz, A. Alvermann, L. Bakemeier, and H. Fehske, Europhys. Lett. **113**, 64002 (2016).
[21] J. Mumford, D. H. J. O'Dell, and J. Larson, Ann. Phys. **527**, 115 (2015).
[22] J. Larson and M. Horsdal, Phys. Rev. A **84**, 021804 (2011).
[23] H. Xu, U. Kemiktarak, J. Fan, S. Ragole, J. Lawall, and J. M. Taylor, arXiv:1510.04971.
[24] J. Ruiz-Rivas, C. Navarrete-Benlloch, G. Patera, E. Roldán, and G. J. de Valcárcel, Phys. Rev. A **93**, 033850 (2016).
[25] J. Thompson, B. Zwickl, A. Jayich, F. Marquardt, S. M. Girvin, and J. G. E. Harris, Nature (London) **452**, 72 (2008).
[26] A. M. Jayich, J. C. Sankey, B. M. Zwickl, C. Yang, J. D. Thompson, S. M. Girvin, A. A. Clerk, F. Marquardt, and J. G. E. Harris, New J. Phys. **10**, 095008 (2008).
[27] M. Bhattacharya, H. Uys, and P. Meystre, Phys. Rev. A **77**, 033819 (2008).
[28] M. Ludwig, A. H. Safavi-Naeini, O. Painter, and F. Marquardt, Phys. Rev. Lett. **109**, 063601 (2012).
[29] H. K. Cheung and C. K. Law, Phys. Rev. A **84**, 023812 (2011).
[30] C. K. Law, Phys. Rev. A **51**, 2537 (1995).

www.nature.com/scientificreports

SCIENTIFIC REPORTS

OPEN

Light-sound interconversion in optomechanical Dirac materials

Christian Wurl & Holger Fehske

Received: 10 March 2017
Accepted: 25 July 2017
Published online: 29 August 2017

Analyzing the scattering and conversion process between photons and phonons coupled via radiation pressure in a circular quantum dot on a honeycomb array of optomechanical cells, we demonstrate the emergence of optomechanical Dirac physics. Specifically we prove the formation of polaritonic quasi-bound states inside the dot, and angle-dependent Klein tunneling of light and emission of sound, depending on the energy of the incident photon, the photon-phonon interaction strength, and the radius of the dot. We furthermore demonstrate that forward scattering of light or sound can almost switched off by an optically tuned Fano resonance; thereby the system may act as an optomechanical translator in a future photon-phonon based circuitry.

The rapidly emerging field of optomechanics, describing the mechanical effects of light, opens new prospects for exploring hybrid quantum-classical systems which raise fundamental questions concerning the interaction and entanglement between microscopic and macroscopic objects[1–3], classical-optical communication in the course of quantum information processing and storage[4–6], cooling of nanomechanical oscillators into their quantum ground state[7–9], or the development of nonclassical correlations[10], nonlinear dynamics, dynamical multistabilities and chaos[11–15]; for a recent review see ref. 16.

Going beyond the prototyp cavity-optomechanical system consisting of a Fabry-Perot cavity with a movable end mirror, the currently most promising platforms are optomechanical crystals or arrays[17–22]. These systems are engineered to co-localize and couple high-frequency (200-THz) photons and low-frequency (2-GHz) phonons. The simultaneous confinement of optical and mechanical modes in a periodic structure greatly enhances the light-matter interaction. Then the next logical step would be the creation of 'optomechanical metamaterials' with an *in situ* tunable band structure, which–if adequately designed–should allow to mimic classical dynamical gauge fields[23], Dirac physics[24], optomechanical magnetic fields[25], or topological phases of light and sound[26], just as optical lattices filled with ultracold quantum gases[27] and topological photonic crystals[28]. Because of the ease of optical excitation, photon-phonon interaction control (i.e., functionalization) and readout, artificial optomechanical structures should be promising building blocks of hybrid photon-phonon signal processing network architectures. Thereby the complimentary nature of photons and phonons regarding their interaction with the environment and their ability to transmit information over some distance will be of particular interest[5].

Here, we study a basic transport phenomenon in planar optomechanical metamaterials, the phonon-affected photon transmission (reflection) through (by) a circular barrier, acting as a 'qantum dot', created optically on a honeycomb lattice. Figure 1 shows the 'optomechanical graphene' setup under consideration. Solving the scattering problem for a plane photon wave injected by a probe laser, we discuss Dirac polariton formation, possible Klein tunneling and photon-phonon conversion triggered by the (barrier-laser) tunable interaction between the co-localized optical and mechanical modes in the quantum dot region. The scattering of a perpendicularly incident (plane) photon wave by a planar barrier has been investigated with a focus on Klein-tunneling[24]. Hence, to some degree, the present work can be understood as an extension of this study to the more complex quantum dot-array geometry, yielding a much richer angle-dependent scattering and photon-phonon conversion.

Theoretical modelling

To formulate the scattering problem we follow the standard approach of (i) linearizing the dynamics around the steady-state solution within the rotating-wave approximation in the red-detuned ($\Delta = \omega_L - \omega_{cav} < 0$) moderate-driving regime[16] and (ii) adapting the single-valley Dirac-Hamiltonian within the continuum approximation, valid for sufficiently low energies and barrier potentials that are smooth on the scale of the lattice constant a but sharp on the scale of the de Broglie wavelength[29]. Furthermore, focusing on the scattering by the barrier

Institute of Physics, Ernst-Moritz-Arndt University Greifswald, Greifswald, 17489, Germany. Correspondence and requests for materials should be addressed to C.W. (email: wurl@physik.uni-greifswald.de) or H.F. (email: fehske@physik.uni-greifswald.de)

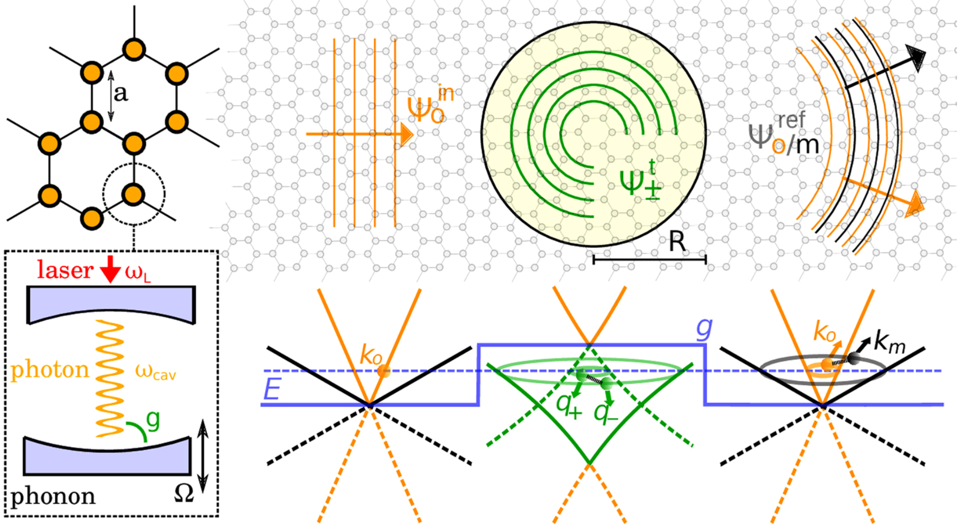

Figure 1. Setup considered in this work. Left part: Optomechanical graphene. Honeycomb array of optomechanical cells driven by a laser with frequency ω_L. The co-localized cavity photon (ω_{cav}) and phonon (Ω) modes interact (linearly) via radiation pressure tunable by the laser power[16]. Upper right part: Scattering geometry. An incident optical wave (ψ_o^{in}, energy E, wavevector $\mathbf{k}_o \| \mathbf{e}_x$) hits the quantum dot (radius R, photon-phonon coupling g); as a result transmitted polaritonic ($\psi^t = \psi_+^t + \psi_-^t$) and reflected ($\psi^{ref} = \psi_o^{ref} + \psi_m^{ref}$) waves appear (with wavevectors $\mathbf{q}_\pm$ and $\mathbf{k}_{o/m}$), which–due to the symmetry of the problem–carry an angular momentum, i.e., their wavevectors have components in any planar direction[29, 30]. Lower right part: Schematic bandstructure. Without photon-phonon coupling the photon (orange) and phonon (black) Dirac cones (obtained in low-energy approximation) simply intersect. In the quantum dot region with $g > 0$, weakly non-linear (photon-phonon) polariton bands (green) emerge. Here, solid (dashed) lines correspond to pseudospin $\boldsymbol{\sigma} = 1$ (-1). Connecting lines between $\mathbf{q}_+$ and $\mathbf{q}_-$ ($\mathbf{k}_o$ and $\mathbf{k}_m$) indicate that the corresponding states are superimposed. The dashed (solid) blue line gives the energy E (position-dependent profile of g). Model parameters: The continuum approximation is justified if $k \ll 1/a$ and $R \gg a$. Moreover, we have to avoid any 'phonon lasing' instabilities, i.e., the photon transfer element $2v_o/3a$ has to be smaller than $\Omega/3$[24]. If so, the effects discussed in this paper should be experimentally accessible for $g/\Omega \ll 1$. With a lattice constant $a \sim 50\,\mu$m[19], a photon [phonon] transfer element ~$\Omega/6$ [$\Omega/60$], and a membrane eigenfrequency $\Omega = -\Delta \sim 10$ MHz[24], the photons [phonons] group velocity v_o [v_m] is about 10^3 m/s [10^2 m/s], and the optomechanical coupling g should not exceed 0.1 MHz. Then, $R \sim 100a$.

exclusively, we assume $\Delta = -\Omega$, and obtain (after the appropriate rescaling $H \to H/\hbar - \Omega$) the optomechanical Dirac-Hamiltomian[24],

$$H = \left(\bar{v} + \frac{1}{2}\delta v \tau_z\right)\sigma \cdot \mathbf{k} - g\Theta(R - r)\tau_x, \tag{1}$$

as a starting point ($\hbar = 1$). Here, $\bar{v} = \frac{1}{2}(v_o + v_m)$, $\delta v = v_o - v_m$, with $v_{o/m}$ as the velocities of the optical/mechanical modes, $\boldsymbol{\tau}$ and $\boldsymbol{\sigma}$ are vectors of Pauli matrices, $\mathbf{k}(\mathbf{r})$ gives the wavevector (position vector) of the Dirac wave, R is the quantum-dot radius, and g parametrizes the photon-phonon coupling strength, cf. Fig. 1. The low-energy dispersion follows as

$$E_{\tau,\sigma}(\mathbf{k}) = \sigma\bar{v}|\mathbf{k}| + \sigma\tau\sqrt{g^2 + \frac{\delta v^2}{4}|\mathbf{k}|^2}, \tag{2}$$

where $\tau = \pm 1$ denote the two-fold degenerate, non-linear polariton branches with sublattice pseudospin $\sigma = \pm 1$. The eigenfunctions of (1) take the form $\psi_{\tau,\sigma} = \mathcal{N}_{\tau,\sigma}|\sigma, \mathbf{k}\rangle(g|o\rangle + \varepsilon_{\tau,\sigma}|m\rangle)$ with normalization $\mathcal{N}_{\tau,\sigma} = (g^2 + \varepsilon_{\tau,\sigma}^2)^{-1/2}$, $\varepsilon_{\tau,\sigma} = v_o\sigma k - E_{\tau,\sigma}$, and the bare (optical/mechanical) eigenstates o/m of τ_z. For $g = 0$, the bandstructure simplifies to two independent photonic and phononic Dirac cones, and the scattering problem can be solved as for a graphene quantum dot[29–31].

We expand the incident photonic wave (in x direction), the transmitted wave inside the dot ($\psi^t = \psi_+^t + \psi_-^t$) and the reflected wave ($\psi^{ref} = \psi_o^{ref} + \psi_m^{ref}$) in polar coordinates ($l$–quantum number of angular momentum):

$$\psi_o^{in} = \frac{1}{\sqrt{2}}e^{ik_o x}\begin{pmatrix}1\\1\end{pmatrix}|o\rangle = \sum_{l=-\infty}^{\infty} i^{l+1}\phi_l^{(1)}(k_o r)|o\rangle, \tag{3}$$

$$\psi_{\pm}^{t} = \mathcal{N}_{\pm}\sum_{l} i^{l+1} t_{\pm,l}\phi_l^{(1)}(q_{\pm}r)[g|o\rangle + \varepsilon_{\pm}|m\rangle], \tag{4}$$

$$\psi_{o/m}^{ref} = \sum_{l} i^{l+1}\sqrt{\frac{v_o}{v_{o/m}}}\, r_{o/m,l}\phi_l^{(3)}(k_{o/m}r)|o/m\rangle. \tag{5}$$

For $E>0$, we can take $\sigma=+1$ and distinguish the branches of the incident and reflected waves by $\tau=\pm1$. For the transmitted wave, where $\varepsilon_{\pm}=v_o\sigma_{\pm}q_{\pm}-E$, $E \gtrless g$ is possible and we denote the two polaritonic branches by $+$ and $-$. Here, for $E>g$ ($E<g$) $\sigma_{\pm}=1$ ($\tau_{\pm}=-1$), and states with different $\tau_{\pm}=\pm1$ ($\sigma_{\pm}=\pm1$) are superimposed, see Fig. 1. In eqs (3–5) the eigenfunctions of the Dirac-Weyl Hamiltonian $\boldsymbol{\sigma}\cdot\mathbf{k}$ are

$$\phi_l^{(1,3)}(kr) = \frac{1}{\sqrt{2}}\begin{pmatrix} -i\mathcal{Z}_l^{(1,3)}(kr)e^{il\phi} \\ \sigma\mathcal{Z}_{l+1}^{(1,3)}(kr)e^{i(l+1)\phi}\end{pmatrix}, \tag{6}$$

where $\mathcal{Z}_l^{(1)} = J_l\,[\mathcal{Z}_l^{(3)} = H_l^{(1)}]$ are the Bessel [Hankel] function of the first kind (in the following we omit the upper index $^{(1)}$ of the Hankel functions). The continuity conditions at $r=R$ give the reflection $r_{o/m,l}$ and transmission coefficients $t_{\pm,l}$:

$$r_{o/m,l} = -\sqrt{\frac{v_{o/m}}{v_o}}\frac{Z_{o/m,l}}{detA}, \qquad t_{\pm,l} = -\frac{1}{\mathcal{N}_{\pm}}\frac{W_{\pm,l}}{detA}. \tag{7}$$

In eq. (7), $Z_{o,l}=\det A - igY$, and

$$\begin{aligned} Z_{m,l} \;=\; & -i\varepsilon_{+}\varepsilon_{-}\times\{(Y_l(k_oR)J_{l+1}(k_oR) - Y_{l+1}(k_oR)J_l(k_oR)) \\ & \times(\sigma_{+}J_l(q_{-}R)J_{l+1}(q_{+}R) - \sigma_{-}J_l(q_{+}R)J_{l+1}(q_{-}R))\}, \end{aligned} \tag{8}$$

$$\begin{aligned} W_{\pm,l} \;=\; & \mp\varepsilon_{\mp}\times\{(H_l(k_oR)J_{l+1}(k_oR) - H_{l+1}(k_oR)J_l(k_oR)) \\ & \times\{(J_l(q_{\mp}R)H_{l+1}(k_mR) - \sigma_{\mp}J_{l+1}(q_{\mp}R)H_l(k_mR))\}, \end{aligned} \tag{9}$$

$$\begin{aligned} Y \;=\; & Y_l(k_oR)\times\{[\varepsilon_{-}\sigma_{+}J_l(q_{-}R)J_{l+1}(q_{+}R) - \varepsilon_{+}\sigma_{-}J_l(q_{+}R)J_{l+1}(q_{-}R)] \\ & \cdot H_{l+1}(k_mR) + \sigma_{+}\sigma_{-}(\varepsilon_{+} - \varepsilon_{-})J_{l+1}(q_{+}R)J_{l+1}(q_{-}R)H_l(k_mR)\} \\ & + Y_{l+1}(k_oR)\times\{[\varepsilon_{-}\sigma_{-}J_l(q_{+}R)J_{l+1}(q_{-}R) - \varepsilon_{+}\sigma_{+}J_l(q_{-}R)J_{l+1}(q_{+}R)] \\ & \cdot H_l(k_mR) + (\varepsilon_{+} - \varepsilon_{-})J_l(q_{-}R)J_l(q_{+}R)H_{l+1}(k_mR)\}. \end{aligned} \tag{10}$$

Here, $\det A$ is obtained from eq. (10) when substituting $Y_{l(+1)}$ by $H_{l(+1)}$ and multiplying by g. Note that the scattering coefficients are invariant under the transformation $(E, g, R^{-1})\to(\gamma E, \gamma g, \gamma R^{-1})$ with $\gamma\in\mathbb{R}$. Furthermore, the reflection coefficients have upper bounds: $|r_{o,l}|\le 1$ and $|r_{m,l}| \le \sqrt{v_o/v_m}/2$.

From the current density of the reflected waves in the far field,

$$\begin{aligned} j_{o/m}(\phi) \;=\; & \frac{4v_o}{\pi k_{o/m}r}\sum_{l,l'=0}^{\infty} r^{*}_{o/m,l'}r_{o/m,l} \\ & \times[\cos((l + l' + 1)\phi) + \cos((l - l')\phi)], \end{aligned} \tag{11}$$

we obtain the scattering efficiency, that is, the scattering cross section divided by the geometric cross section, as

$$Q_{o/m} = \frac{4}{k_{o/m}R}\sum_{l=0}^{\infty}|r_{o/m,l}|^2. \tag{12}$$

We note that in eqs (11), (12), and hereafter, $l\ge 0$. The density $\rho=\psi^{\dagger}\psi$ and the current $\mathbf{j}=\psi^{\dagger}\boldsymbol{\sigma}\psi$ in- and outside the quantum dot region further specify the scattering.

Numerical results and discussion

Treating the scattering by the circular quantum dot region numerically, we adopt $v_m=0.1v_o$ and employ units such that $v_o=1$. Moreover, for the experimental reliable parameters quoted in the caption of Fig. 1, fixing g, $100a$ is a natural unit for the quantum dot radius R, where the number of cells (defects) enclosed in the quantum dot region is about 10^4R^2. Due to the scale invariance of the scattering coefficients, in what follows all physical quantities will be discussed in dependence on E/g and Rg.

Figure 2 displays the complex pattern of both the photonic Q_o and phononic Q_m contributions to the scattering efficiency in the E/g–Rg plane. When the photon hits the quantum dot it stimulates mechanical vibrations (phonons) because of the optomechanical interaction. Then both scattered waves are inherently correlated. For energies of incident photon larger than the optomechanical coupling, Q_o (Q_m) reveals a very broad (narrow) ripple structure with maxima of high (rather low) intensity. Above $E/g\sim 2$ the phonon is hardly scattered, while the photon is still heavily influenced by the dot. This is because the phonon wave numbers take large values very

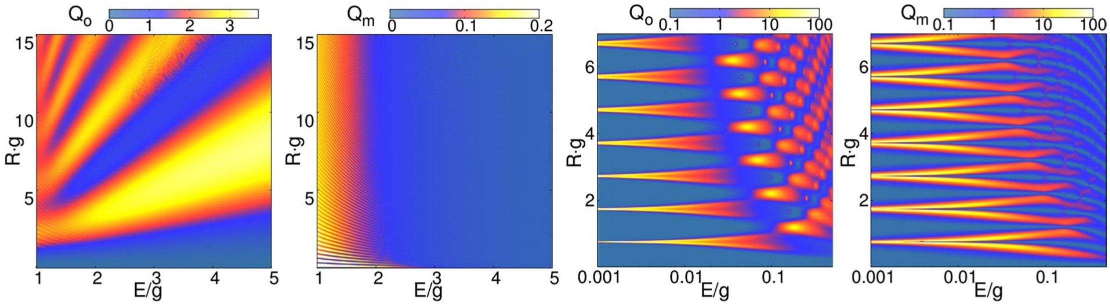

Figure 2. Photonic/phononic scattering efficiency $Q_{o/m}$ in the E/g-Rg plane.

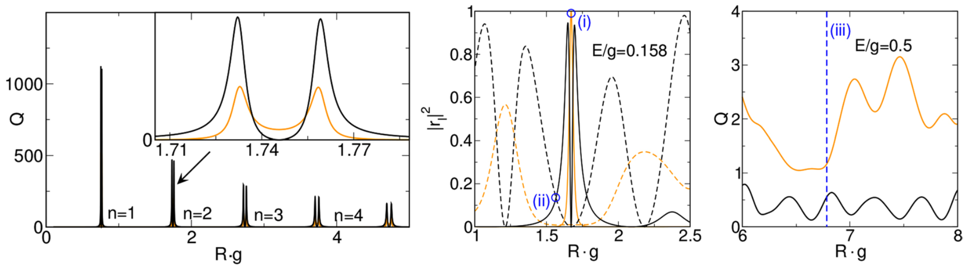

Figure 3. Left: scattering efficiency for photons (orange) and phonons (black) in dependence on Rg. Here, $E/g = 0.001$, i.e., the size-parameter $ER \ll 1$. For $n = 2$, Q_m vanishes at $Rg \simeq 1.75$, whereas Q_o stays finite (see inset). Middle: photonic (orange) and phononic (black) reflection coefficients with $l = 0$ (dashed) and $l = 1$ (solid) in dependence on Rg, where $E/g = 0.158$, i.e., the size-parameter $ER \lesssim 1$. For better comparison, the phononic coefficients were divided by their upper bound $v_o/4v_m$. Rigth: photonic (orange) and phononic (black) scattering efficiency at $E/g = 0.5$; now $ER \gtrsim 1$. The cases $Rg = 1.671$, $Rg = 1.566$ and $Rg = 6.78$ are marked by (i), (ii), and (iii), respectively.

quickly, compared to those of the photon, simply because v_m is smaller than v_o by an order of magnitude. If the dispersion of the phonon is unaffected by g, the wave numbers inside and outside are almost identical and scattering disappears. The same, in principle, happens to the photon, but at much larger energies. In this limit, photon scattering resembles the scattering of ultrarelativistic Dirac particles, which are massless outside the dot and carry an effective mass $m = g\sqrt{2/v_o^3(v_o - v_m)}$ inside the quantum dot region (here, v_o plays the role of vacuum ligth speed).

The situation becomes much more involved when the energy of the incident optical wave is smaller than the optomechanical coupling, see the right panels in Fig. 2 for $E/g < 1$. Let us first consider the case where the size-parameter ER is very small, i.e., the wavelengths $2\pi/k_{o/m}$ are large compared to the quantum dot radius R. In Fig. 2 this corresponds to the region $E/g \lesssim 0.01$. Here, sharp scattering resonances occur at a sequence of equidistant radii. The left panel in Fig. 3 gives a closer look at this limiting behavior and demonstrates that in each case two resonances occur, in fact, symmetrically around a point where the phonon scattering vanishes while the photon scattering is small but finite (see inset). These resonances, numbered by $n \in \mathbb{N}$, belong to the lowest photonic/phononic partial waves with $l = 0$. Expanding the phononic reflection coefficients (8) with respect to the small size-parameter ER, the phonon-scattering depletion points result as $Rg = j_{l,n}\sqrt{v_o v_m}$, where $j_{l,n}$ are the n-th zero of the Bessel function J_l. We note that here the phonon resonance peaks are larger than the photonic ones. Of course, such resonances also occur for the next higher partial wave with $l = 1$ at $Rg = j_{1,n}\sqrt{v_o v_m}$, but are not visible in Fig. 3 left on account of their tiny linewidth/intensity.

In case that the size-parameter $ER \sim 1$, the wavelengths $2\pi/k_{o/m}$ are in the order of the dot radius R. In this regime, only the lowest partial waves will be excited to any appreciable extent, and the photonic [phononic] resonances appear as bright spots [splitted stripes] at specific 'points' [lines] in the E/g-Rg plane, see Fig. 2. The linewidths get smaller for larger l, once one of the reflection coefficients $r_{o,l}$ ($r_{m,l}$) reaches unity (their upper bound). The photonic resonances with even (odd) l are approximately located at $Rg = j_{1(0),n}\sqrt{v_o v_m}$, where the phononic scattering is perfectly suppressed. This is illustrated by the middle panel in Fig. 3: At $Rg \simeq 1.7$ [case (i)], the $l = 1$ photon mode is resonant and the scattering becomes purely photonic (i.e., the contribution of all phonon modes goes to zero). The phonon resonances of the $l = 1$ mode appear symmetrically about this photon resonance (at these points, on the other hand, the photonic contribution is significantly weakened). A similar scenario arises for the resonance of the $l = 0$ modes at $Rg \simeq 1.24$ and $Rg \simeq 2.24$. Vice versa, at certain radii the scattering becomes purely phononic, see, e.g., case (ii) where $Rg = 1.566$. This allows one to switch from entirely photon to phonon scattering just by varying the dot radius.

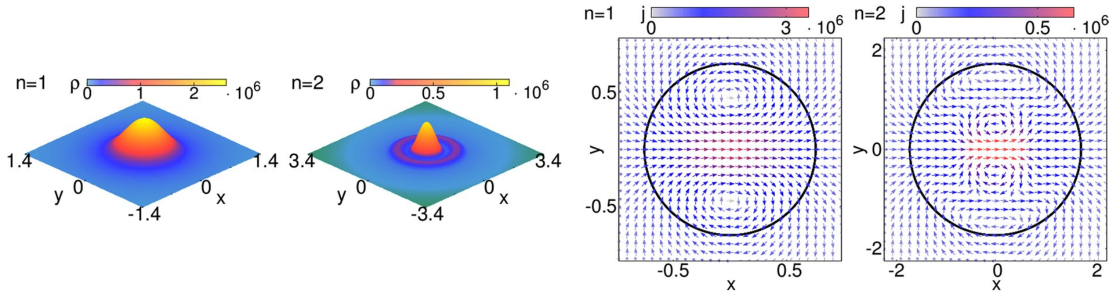

Figure 4. Scattering characteristics in the near field. Shown are the probability density $\rho=\psi^{\dagger}\psi$ (left) and the current density $\boldsymbol{j}=\psi^{\dagger}\boldsymbol{\sigma}\psi$ for $l=0$ (right; the circle marks the quantum dot), where $\psi=\psi^{t}$ inside and $\psi=\psi^{in}+\psi^{ref}$ outside the dot. Results correspond to the resonances $n=1$ and $n=2$ given by Fig. 3 (left) and we have chosen $R=0.754$ for $n=1$ and $R=1.732$ for $n=2$ (with $g=1$), where $Q_o=Q_m$ (crossing of black and orange lines in the inset of the left panel in Fig. 3).

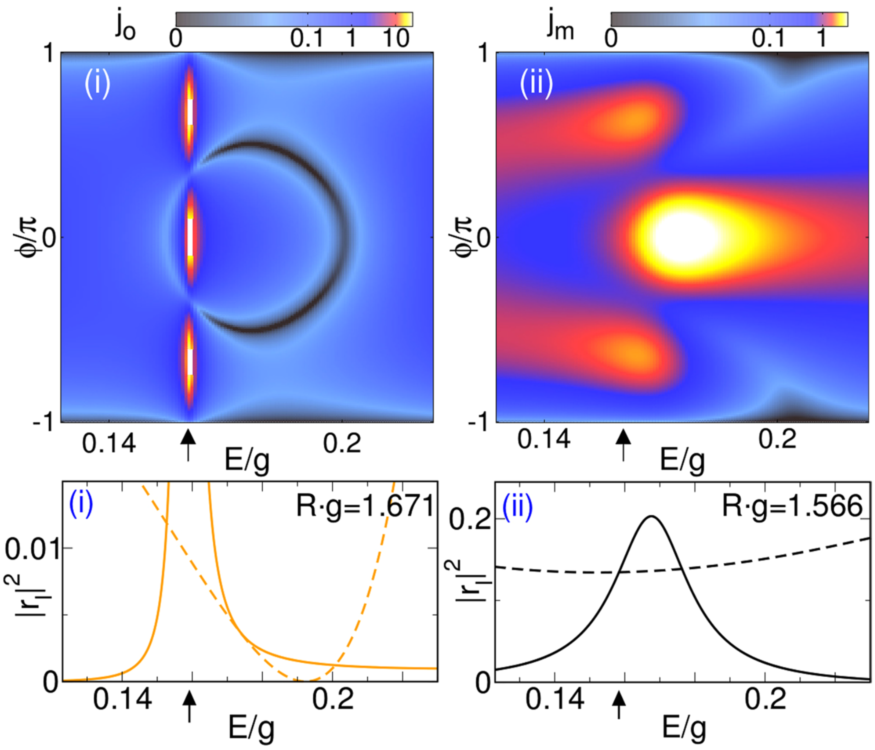

Figure 5. Photonic (j_o) and phononic (j_m) angle-resolved far-field current [top] and first two photonic (orange) and phononic (black) reflection coefficients with $l=0$ (dashed) and $l=1$ (solid) [bottom] in dependence of E/g for the cases (i) and (ii) in the middle panel of Fig. 3. Again the phononic reflection coefficients $|r_m|^2$ are divided by $v_o/4v_m$. Arrows mark the energy $E/g=0.158$ used in the middle panel of Fig. 3.

If the size-parameter increases further, the situation changes again. Now even higher partial waves will be excited. In this regime, the photon scattering efficiency is always a larger than the phononic one. Approximating the resonance points by the zeros of the Bessel function is no longer possible; as a result both Q_o, $Q_m>0$, cf. Fig. 3 right. In the extreme limit $ER \gg 1$, however, phonon scattering is negligibly small and does not have to be considered.

Having discussed the global scattering efficiency of the quantum dot, let us now analyze the spatial resolution of the wave transmisson and reflection. We start by investigating the scattering characteristics, specified by the probability density $\rho=\psi^{\dagger}\psi$ and current density $\mathbf{j}=\psi^{\dagger}\hat{\mathbf{j}}\psi$, in the near field, see Fig. 4. In the quantum dot region polaritons (mixed photon-phonon states) are formed. For very small size-parameters $ER \ll 1$ and energies $E/g<1$, the polariton density inside the dot becomes

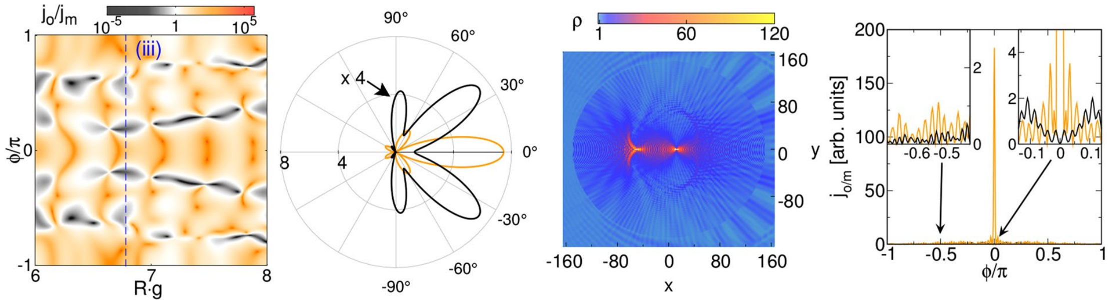

Figure 6. Left: angle-resolved ratio of photonic (j_o) and phononic (j_m) currents in the far field depending on Rg. Middle left: polar plot of the photonic (orange) and phononic (black) far-field currents (arbitrary units) for case (iii) of Fig. 3 [right panel] (marked by the vertical blue dashed line in the left panel). The phononic current was multiplied by a factor of four. Middle right: probability density ρ inside and outside the quantum dot. Right: photonic (orange) and phononic (black) currents in the far-field for $R=150$ ($g=1$), $E=0.5$, i.e., the size-parameter $ER \gg 1$.

$$|\psi^t|^2 = (|t_{+,l}|^2 + |t_{-,l}|^2)[J_l(qr)^2 + J_{l+1}(qr)^2] - 2\frac{v_o - v_m}{v_o + v_m}\Re\mathfrak{e}(t_{+,l}^* t_{-,l})t[J_l(qr)^2 - J_{l+1}(qr)^2]. \tag{13}$$

Obviously, ρ is radially symmetric (we have used that $q_\pm \to q = g/\sqrt{v_o v_m}$ for $E \to 0$). For resonant scattering the polariton density increases dramatically inside the dot, indicating a spatial and temporal 'trapping' of photon-phonon bound state, cf. Fig. 4, left panels. The resonance of the lowest partial wave $l=0$ confines the 'quasiparticle' about $r=0$, while resonances with higher $l>0$ (not shown) give rise to ring-like structures close to the dot boundary related to 'whispering gallery modes'.

The current density inside the dot is given by

$$\mathbf{j}^t = \frac{2v_o v_m}{v_o + v_m}(|t_{+,l}|^2 + |t_{-,l}|^2) \times \{\cos((2l+1)\phi)[J_{l+1}(qr)^2 + J_l(qr)^2]\mathbf{e}_r + \sin((2l+1)\phi)[J_{l+1}(qr)^2 - J_l(qr)^2]\mathbf{e}_\phi\}. \tag{14}$$

The panels right in Fig. 4 show that the incident wave is fed into vortices which trap the polariton. For $l=0$, two vortices arise for the $n=1$ mode. Further vortices occur on the symmetry axis when n increases. In general, the vortex pattern of the l-th mode is dominated by $2(2l+1)$ vortices which give rise to $2l+1$ preferred scattering directions in the far field for $n=1$ (see below)[29]. We note that a very similar vortex pattern (scattering characteristics) arises for moderate size-parameters $ER \sim 1$, e.g., for the cases (i) and (ii) in the middle panel of Fig. 3.

The current density of the reflected waves in the far field given by eq. (11) exhibits the already mentioned cosinusoidal angle distribution with maxima at $\phi = l'\pi/(2l+1)$ where $l' \in \{0, \ldots, \pm l\}$. Consequently, if the $l=0$ mode is resonant, only forward scattering takes place, whereas resonaces belonging to higher modes scatter the light respectively sound into different directions. This is illustrated by Fig. 5 (upper panels), for the far-field currents $j_{o/m}$ of a specific quantum dot system that preferably suppresses either the phonon [case(i)] or the photon [case(ii)] scattering [cf. Fig. 3, middle]. Accordingly, when the photonic partial wave with $l=1$ becomes resonant, we observe three preferred scattering directions with equal intensity (left upper panel). Though a similar distribution results for the phononic resonance, now the forward scattering is somewhat enhanced as the lower $l=0$ mode substantially contributes (right upper panel). Note that both waves will never be scattered in the angle range $\phi \simeq \pm\pi$ due to absence of backscattering. Most interestingly, the constructive and destructive interference between a resonant l mode and the off-resonant $l=0$ mode can lead to a Fano resonance[32] that for its part may cause a depletion of Klein tunneling, i.e., a suppression of forward scattering[29]. In this way, the interference between the first two photonic and phononic partial waves depicted in the lower panels of Fig. 5 give rise to Fano resonances, which are reflected in the almost vanishing currents $j_{o/m}$ at certain ratios $E/g(\phi)$, even for $\phi=0$ (see upper panels). Varying the energy of the incident wave therefore allows to control the scattering into pure photon or phonon waves, having preferred directions of propagation, with or without forward scattering.

For larger size-parameters, $ER>1$, where many partial waves may become resonant [e.g., case (iii) in Fig. 3 (right)], a rather complex structure of the far-field currents evolves. The two left panels in Fig. 6 display the ratio j_o/j_m in the Rg–ϕ plane and gives a polar plot of the light/sound emission. The figure corroborates the use of the considered setup as an optomechanical switch or light-sound translator. Finally, when $ER \gg 1$ and the extent of the quantum dot is much greater than the wavelengths, the scattering shows features known from ray optics [cf. Fig. 6, middle right]. Such size parameters can only be realized by very large R, i.e., by a large number of cells (of the order of 10^8) enclosed in the quantum dot region. The excitation of a large number of partial waves and their interference results in a caustics-like pattern of the transmitted wave inside the quantum dot and, most strikingly, the circular optomechanical barrier acts as a lens, focusing the light beam in forward direction, whereas the sound propagation is depleted [cf. Fig. 6, right]. The far-field currents strongly oscillate when ϕ becomes finite, whereby the phonon contribution is on average much smaller than those of the photon.

To sum up, we have demonstrated Dirac physics in an optomechanical setting. Solving–within Dirac-Weyl theory–the problem of light scattering by circular barriers in artificial graphene composed of tunable optomechanical cells, we show that large quantum dots enable photon lensing, while small dots trigger the formation of polariton (photon-phonon) states which cause a spatial and temporal trapping of the incident wave in vortex-like structures, and a subsequent direction-dependent re-emittance of light and sound. In the latter case (quantum regime), the quantum dot can be used to entangle photons and phonons and convert light to sound waves and vice versa. Equally important, the forward scattering and Klein tunneling of photons could switched off for small dots by optically tuning a Fano resonance arising from the interference between resonant scattering and the background partition. In this way optomechanical cells might be utilized to transfer, store, translate and process information in (quantum) optical communications, or simply to realize a coherent interface between photons and phonons.

References

1. Vitali, D. *et al*. Optomechanical entanglement between a movable mirror and a cavity field. *Phys. Rev. Lett.* **98**, 030405 (2007).
2. Ludwig, M., Hammerer, K. & Marquardt, F. Entanglement of mechanical oscillators coupled to a nonequilibrium environment. *Phys. Rev. A* **82**, 012333 (2010).
3. Ghobadi, R. *et al*. Optomechanical micro-macro entanglement. *Phys. Rev. Lett.* **112**, 080503 (2014).
4. Palomaki, T. A., Harlow, J. W., Teufel, J. D., Simmonds, R. W. & Lehnert, K. W. Coherent state transfer between itinerant microwave fields and a mechanical oscillator. *Nature* **475**, 210 (2013).
5. Safavi-Naeini, A. H. & Painter, O. Proposal for an optomechanical traveling wave phonon–photon translator. *New Journal of Physics* **13**, 013017 (2011).
6. Fang, K., Matheny, M. H., Luan, X. & Painter, O. Optical transduction and routing of microwave phonons in cavity-optomechanical circuits. *Nature Photonics* **10**, 489 (2016).
7. Chan, J. *et al*. Laser cooling of a nanomechanical oscillator into its quantum ground state. *Nature* **478**, 89 (2011).
8. Teufel, J. D. *et al*. Sideband cooling of micromechanical motion to the quantum ground state. *Nature* **495**, 359 (2011).
9. Frimmer, M., Gieseler, J. & Novotny, L. Cooling mechanical oscillators by coherent control. *Phys. Rev. Lett.* **117**, 163601 (2016).
10. Riedinger, R. *et al*. Non-classical correlations between single photons and phonons from a mechanical oscillator. *Nature* **530**, 313 (2016).
11. Marquardt, F., Harris, J. G. E. & Girvin, S. M. Dynamical multistability induced by radiation pressure in high-finesse micromechanical optical cavities. *Phys. Rev. Lett.* **96**, 103901 (2006).
12. Qian, J., Clerk, A. A., Hammerer, K. & Marquardt, F. Quantum signatures of the optomechanical instability. *Phys. Rev. Lett.* **109**, 253601 (2012).
13. Wurl, C., Alvermann, A. & Fehske, H. Symmetry-breaking oscillations in membrane optomechanics. *Phys. Rev. A* **94**, 063860 (2016).
14. Bakemeier, L., Alvermann, A. & Fehske, H. Route to chaos in optomechanics. *Phys. Rev. Lett.* **114**, 013601 (2015).
15. Schulz, C., Alvermann, A., Bakemeier, L. & Fehske, H. Optomechanical multistability in the quantum regime. *Europhys. Lett.* **113**, 64002 (2016).
16. Aspelmeyer, M., Kippenberg, T. J. & Marquardt, F. Cavity optomechanics. *Rev. Mod. Phys.* **86**, 1391–1452 (2014).
17. Zhang, M., Shah, S., Cardenas, J. & Lipson, M. Synchronization and phase noise reduction in micromechanical oscillator arrays coupled through light. *Phys. Rev. Lett.* **115**, 163902 (2015).
18. Eichenfield, M., Chan, J., Camacho, R. M., Vahala, K. J. & Painter, O. Optomechanical crystals. *Nature* **462**, 78–82 (2009).
19. Safavi-Naeini, A. H. & Painter, O. Design of optomechanical cavities and waveguides on a simultaneous bandgap phononic-photonic crystal slab. *Opt. Express* **18**, 14926–14943 (2010).
20. Safavi-Naeini, A. H. *et al.* Two-dimensional phononic-photonic band gap optomechanical crystal cavity. *Phys. Rev. Lett.* **112**, 153603 (2014).
21. Ludwig, M. & Marquardt, F. Quantum many-body dynamics in optomechanical arrays. *Phys. Rev. Lett.* **111**, 073603 (2013).
22. Heinrich, G., Ludwig, M., Qian, J., Kubala, B. & Marquardt, F. Collective dynamics in optomechanical arrays. *Phys. Rev. Lett.* **107**, 043603 (2011).
23. Walter, S. & Marquardt, F. Classical dynamical gauge fields in optomechanics. *New Journal of Physics* **18**, 113029 (2016).
24. Schmidt, M., Peano, V. & Marquardt, F. Optomechanical Dirac physics. *New Journal of Physics* **17**, 023025 (2015).
25. Schmidt, M., Kessler, S., Peano, V., Painter, O. & Marquardt, F. Optomechanical creation of magnetic fields for photons on a lattice. *Optica* **2**, 635–641 (2015).
26. Peano, V., Brendel, C., Schmidt, M. & Marquardt, F. Topological phases of sound and light. *Phys. Rev. X* **5**, 031011 (2015).
27. Bloch, I. Ultracold quantum gases in optical lattices. *Nature* **1**, 23 (2005).
28. Lu, L., Joannopoulos, J. D. & Soljačić, M. Topological photonics. *Nature Photonics* **8**, 821 (2014).
29. Heinisch, R. L., Bronold, F. X. & Fehske, H. Mie scattering analog in graphene: Lensing, particle confinement, and depletion of Klein tunneling. *Phys. Rev. B* **87**, 155409 (2013).
30. Schulz, C., Heinisch, R. L. & Fehske, H. Electron flow in circular graphene quantum dots. *Quantum Matter* **4**, 346–351 (2015).
31. Schulz, C., Heinisch, R. L. & Fehske, H. Scattering of two-dimensional Dirac fermions on gate-defined oscillating quantum dots. *Phys. Rev. B* **91**, 045130 (2015).
32. Fano, U. Effects of configuration interaction on intensities and phase shifts. *Phys. Rev.* **124**, 1866–1878 (1961).

Acknowledgements

This work was supported by Deutsche Forschungsgemeinschaft through SFB 652 (project B5). The authors wish to thank Andreas Alvermann for useful discussions at an early stage of this work.

Author Contributions

H. Fehske and C. Wurl outlined the scope of the paper and the strategy of the calculation. The calculations were performed by C. Wurl. H. Fehske wrote the paper which was edited by C. Wurl.

Additional Information

Competing Interests: The authors declare that they have no competing interests.

EPJ manuscript No.
(will be inserted by the editor)

Time-periodic Klein tunneling through optomechanical Dirac barriers

Christian Wurl[a] and Holger Fehske[b]

Institute of Physics, Ernst Moritz Arndt University Greifswald, Greifswald, 17489, Germany

Abstract. We study the interconversion between photons and phonons coupled via radiation pressure in artificial Dirac materials realized by a honeycomb array of optomechanical cells. In particular we analyze the chiral tunneling of (photon-phonon) polaritons through an oscillating planar barrier. While a static barrier accommodates constructively interfering optical or mechanical waves leading to photon or phonon transmission, an oscillating barrier allows for inelastic scattering that causes sideband excitations and interference effects which, in turn, may suppress or revive the light-sound interconversion.

Introduction. In optomechanical graphene, that is, a honeycomb array of optomechanical cells driven by a laser with frequency ω_l, co-localized cavity photon (eigenfrequency ω_o) and phonon (eigenfrequency ω_m) modes interact (linearly) via radiation pressure. The latter is tunable by the laser power. Recently, the scattering and conversion process between photons and phonons, triggered by static laser-induced planar [1] and circular quantum barriers [2], has been worked out within an effective Dirac-Weyl theory, and the emergence of optomechanical Dirac physics has been demonstrated. Because of the chiral nature of the quasiparticles, having a Dirac-like bandstructure, the transport phenomena show similarities to those of low-energy electrons in graphene, but are more subtle due the photon-phonon coupling in the barrier, leading to the formation of polariton (photon-phonon) states. Moreover, for perpendicular incidence of the photon wave, Klein tunneling appears, that is, the unimpeded transmission of the particle regardless of the height or width of the barrier. Interestingly, in the limit of low photon energies or high coupling strengths, when the barrier acts as a kind of Fabry Pérot interferometer, a perfect interconversion between photons and phonons takes place, as a result of a constructive interference of standing optical and mechanical waves respectively.

In this contribution, we extend these investigations by analyzing the passage of Dirac-Weyl quasiparticles in optomechanical graphene through a harmonically oscillating (driven) potential barrier, i.e., we consider the significant case where the energy is not conserved. To this end, we solve the time-periodic scattering problem for a perpendicularly impinging plane photon wave of energy E (injected by a probe laser), and discuss how a quantum barrier that oscillates in time with frequency Ω affects the tunneling process. Since Klein tunneling persists for oscillating barriers due to the

[a] e-mail: `wurl@physik.uni-greifswald.de`
[b] e-mail: `fehske@physik.uni-greifswald.de`

conservation of helicity, we expect that the transport through the barrier is mainly determined by the conversion rate between photons and phonons.

Theoretical approach. For sufficiently low energies, if the barrier is smooth on the lattice scale but sharp on the de Broglie wavelength, umklapp scattering is suppressed and the continuum approximation applies. Then, the system under consideration can be described by the optomechanical Dirac-Weyl Hamiltonian

$$H = \left(\overline{v} + \frac{1}{2}\delta v\, \tau_z\right) \boldsymbol{\sigma} \cdot \boldsymbol{k} - g\,(x,t)\, \tau_x\,, \tag{1}$$

given in units of $\hbar$ after rescaling $H \to H - \hbar\omega_m$ [1,2]. Here, $\overline{v} = (v_o + v_m)/2$, $\delta v = v_o - v_m$, with $v_{o,m}$ as the Fermi velocities of the optical/mechanical modes, $\boldsymbol{\tau}$ and $\boldsymbol{\sigma}$ are Pauli matrices, $\boldsymbol{k}$ ($\boldsymbol{r}$) gives the wavevector (position vector) of the Dirac wave, and $g\,(x,t)$ parametrizes the time-dependent photon-phonon coupling. Note that the single-valley Dirac-Hamiltonian (1) is obtained within the rotating-wave approximation, i.e., in a frame rotating with the laser frequency, in the red detuned moderate-driving regime, $\Delta = \omega_l - \omega_o = -\omega_m$. In order to make the scattering inelastic, we assume that the laser amplitude is modulated by a frequency much smaller than the eigenfrequency of the laser and the mechanical mode, $\Omega \ll \omega_l, \omega_m$ (otherwise the rotating-wave approximation is not granted). Furthermore, to stay within the continuum approximation, Ω should be much smaller than the typical mechanical hopping in the array, i.e. $\Omega \ll 2v_m/3a$ with a as the lattice constant [1]. Then the coupling strength within the barrier of width w is given by

$$g\,(x,t) = [g_0 + g_1 \cos(\Omega t)]\,[\Theta\,(x) - \Theta\,(x-w)]\;, \tag{2}$$

where $g_{0,1}$ is assumed to be constant and $g_1 \leq g_0$.

For the tunneling problem, we consider the incoming photon to be in a plane wave state at energy E and use the time-independent eigensolutions of (1) for $x < 0$, $\psi^{in} \sim |o\rangle \exp(ik^o x - iEt)$, with $k^{o,m} = E/v_{o,m}$ being the optical/mechanical wavenumber and $|o,m\rangle$ the bare optical/mechanical eigenstate of τ_z. In case of perpendicular photon incidence and a barrier potential that is translational invariant in y-direction, the scattering problem becomes one-dimensional. Then, the helicity, $\sigma_x \cdot k_x/|k_x|$, is a conserved quantity with eigenvalue $+1$ (this quantum number is therefore omitted in the following). For this reason no reflected waves appear and Klein-tunneling takes place. As a result of the optomechanical coupling, behind the barrier $x > w$, the transmitted wave consists of optical and mechanical modes $\psi^t = \psi^{t;o} + \psi^{t;m}$, $\psi^{t;o,m} \sim \sum_n t_n^{o,m}\,|o,m\rangle \exp(ik_n^{o,m}x - iE_nt)$. Here, energy states with $E_n = E + n\Omega$ and $k_n^{o,m} = E_n/v_{o,m}$, $n \in \mathbb{Z}$, are superimposed, since the oscillating barrier can give (take) energy to (away from) photons and phonons. The wave inside the barrier is $\psi^b = \psi^{b;+} + \psi^{b;-}$, $\psi^{b;\pm} \sim \sum_{n,n'} b_n^{\pm}[c_{nn'}^{o;\pm}\,|o\rangle + c_{nn'}^{m;\pm}\,|m\rangle]\exp(iq_n^{\pm}x - iE_{n-n'}t)$, with Fourier coefficients $c_{nn'}^{o,m;\pm}$ and wavenumbers $q_n^{\pm}$ obtained from Floquet theory [3,4]. It matches with the incident and transmitted wavefunction at the boundaries, which defines an infinite system of coupled linear equations for the scattering coefficients $t_n^{o,m}$ and $b_n^{\pm}$. From its numerical solution we obtain the current density of the transmitted wave:

$$j^{t;o,m}\,(x/v_{o,m} - t) = v_{o,m} \sum_{n,n'} (t_{n'}^{o,m})^* t_n^{o,m} \exp\left[i\,(n-n')\,\Omega\,(x/v_{o,m} - t)\right]. \tag{3}$$

Then the equation of continuity gives the time-averaged transmission probability $\overline{T}^{o/m} = (v_{o,m}/v_o)\sum_n |t_n^{o,m}|^2$, with $\overline{T}^o + \overline{T}^m = 1$ (no backscattering). Because there are no phonon waves impinging on the barrier, the transmission probability $\overline{T}_m$ can be understood as photon-phonon conversion probability.

Results. In what follows, we adopt $v_m = 0.1 v_o$ and employ units such that $v_o = 1$. Moreover, since the scattering problem is invariant under the transformation $[E, g_{0,1}, \Omega, w^{-1}] \to \gamma[E, g_{0,1}, \Omega, w^{-1}]$ with $\gamma \in \mathbb{R}$, we use units such that $\Omega = 1$.

For a static barrier, $g_1 = 0$, we can analytically calculate the transmission probability of the mechanical mode,

$$T^m_{st} = [1 + (k^o)^2 v_o^2 \left(v_o - v_m\right)^2 / \left(4 v_m v_o g_0^2\right)]^{-1} \sin^2\left((q^+_{st} - q^-_{st}) w/2\right), \tag{4}$$

with wavenumbers $q^{\pm}_{st}$ obtained from the static energy dispersion [2]. Since $T^o_{st} = 1 - T^m_{st}$, in Fig. 1 (upper panels) only T^m_{st} is plotted in the E/g_0-wg_0 plane. As a result of the optomechanical coupling, the incoming photon can be converted into phonons, i.e., $T^m_{st} > 0$. For energies larger than the barrier height (right panel), T^m_{st} reveals a stripe structure with low intensity, where for $E/g_0 \gtrsim 2$ the photon-phonon conversion is strongly suppressed since $v_m \ll v_o$ [2]. For energies smaller than the barrier height (left panel), the stripes in T^m_{st} are much more pronounced, especially in the limit of small energies (high coupling strengths) $E/g_0 \to 0$. Then the two polaritonic waves inside the barrier have antiparallel wavenumbers $\pm g_0/\sqrt{v_o v_m} = \pm q_{st}$ and interfere in such a way, that the wave function simplifies to $\psi^b \propto \cos(q_{st} x) g_0 \left|o\right\rangle + i v_o q_{st} \sin(q_{st} x) \left|m\right\rangle$. In this way, in a semiclassical perspective, the barrier acts as a kind of Fabry-Pérot interferometer accomodating standing optical and mechanical waves respectively. If the optical (mechanical) wave interferes constructively with itself, the transmission becomes purely photonic (phononic), $T^m_{st} = 0$ ($T^m_{st} = 1$), where the resonance condition is $wg_0 = \sqrt{v_o v_m} n\pi/2 \simeq 0.5n$ with n even (odd) natural number.

An oscillating barrier may cause inelastic scattering by excitation of states with energies shifted by multiples of the oscillation frequency, $E_n = E + n\Omega$. In addition to

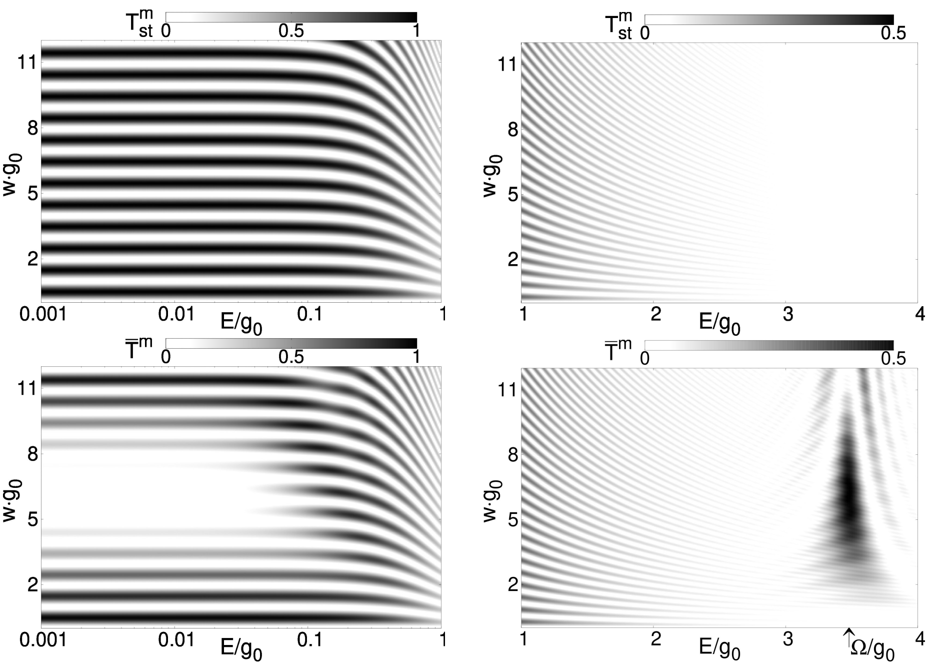

Fig. 1. Transmission probability of the phonon in the E/g_0-wg_0 plane for a static barrier ($g_1 = 0$; top panels) and for an oscillating barrier ($g_1 = 0.073\Omega$, $g_0 = 0.287\Omega$; $\Omega/g_0 \approx 3.48$; bottom panels). The transmission probability of the photon is $T^o_{st} = 1 - T^m_{st}$ ($\overline{T}^o = 1 - \overline{T}^m$).

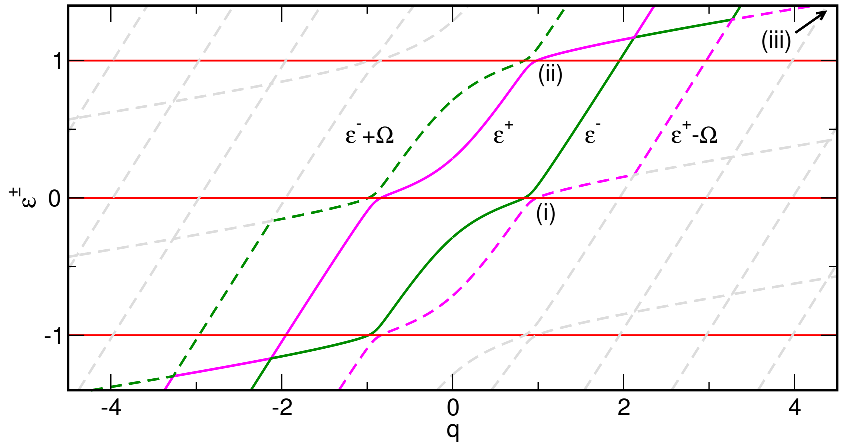

Fig. 2. (Color online) Floquet quasienergies $\varepsilon^{\pm}$ as a function of wavenumber q for the parameter values of Fig. 1, lower panels. The quasienergies are defined in such a way that they coincide with the energy dispersion of the static case for $q \to 0$. Avoided crossings occur between $\varepsilon^{\pm}$ and $\varepsilon^{\mp} \pm \Omega$ (further quasienergy bands are marked in grey).

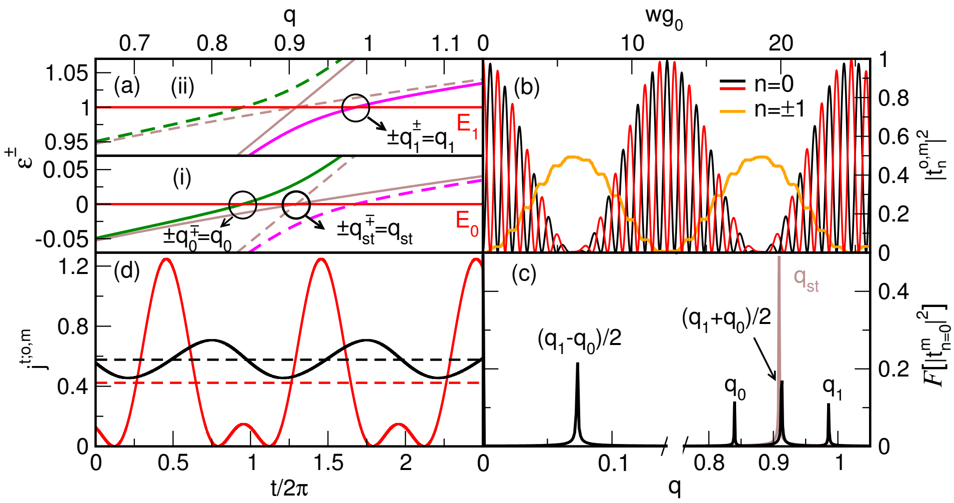

Fig. 3. (Color online) Scattering characteristics for photon energy $E \simeq 0$. (a) Quasienergies $\varepsilon^{\pm}$ as a function of q for the cases (i) and (ii) of Fig. 2. Drawn in are the energies of the central band E_0 and the first sideband E_1 (red lines). Marked are wavenumbers $q = q_{0,1}$, for which $\varepsilon^{\pm}(q) = E_{0,1}$. For comparison the two polariton branches of the dispersion of the static case, $E^{\mp}(q)$ (solid) and $E^{\pm}(q) \mp \Omega$ (dashed), are shown (brown) with wavenumber q_{st}. Avoided crossings appear in the vicinity of points, where the two static polariton branches cross each other. (b) Transmission probability for optical/mechanical central bands $n = 0$ (red/black) and first excited optical sideband $n = \pm 1$ (orange) as a function of wg_0 (here, $|t_n^m|^2$ is multiplied by v_m/v_o). (c) Fourier spectrum of $F[|t_{n=0}^m|^2](q)$ [for comparison the Fourier spectrum of T_{st}^m is included (brown line)]. (d) Time evolution of the optical/mechanical current density $j^{t;o,m}$ (red/black) and the corresponding time-averaged current density (dashed) at $x = w$ for $wg_0 = 2.346$ [crossing of red and orange lines (b)]. In all panels, $g_0 = 0.287\Omega$, $g_1 = 0.073\Omega$ (corresponding to $E/g_0 = 10^{-3}$ in Fig. 1).

the central band, sidebands now yield a significant contribution to the transmission of polaritons. The number of sidebands involved in the tunneling process is mainly determined by the ratio g_1/Ω. Even for weak couplings g_1 (high oscillation frequencies Ω), i.e., in the antiadiabatic limit $g_1/\Omega \ll 1$, the transmission pattern of T^m_{st} is modified by a few sidebands only, see Fig. 1 (lower panels). At very low photon energies, $E/g_0 \ll 1$, for certain widths of the barrier the transmission becomes purely photonic. By contrast, at photon energies close to resonance, $E \sim \Omega$ (in Fig. 1 at $E/g_0 \approx 3.48$), the transmission of phonons may be significantly increased.

To elucidate the underlying mechanism, Fig. 2 shows the quasienergies obtained from Floquet theory as a function of q for the parameters used in Fig. 1. Due to the optical and mechanical degrees of freedom, the quasienergies are two-fold degenerate. This leads to avoided crossings, appearing at energies $E = 0$ and $E = \pm\Omega$ for the considered value of g_0, which are the reason for the drastic modification of the transmission pattern that becomes visible in the lower panels of Fig. 1. The avoided crossings are displayed in Fig. 3 (a) in more detail, together with the energy dispersion for the static case. We observe that the oscillating barrier influences the scattering process the greater the wavenumbers $q_{0,1}$ deviate from the static wavenumbers q_{st}. The difference is largest in the vicinity of the avoided crossings. As a result, for an incoming photon with energy $E \simeq 0$, the entire transmission by the optical and mechanical central bands is transferred to the first optical sidebands $n = \pm 1$ (periodically in wg_0); see Fig. 3 (b) and lower left panel in Fig. 1 at $E/g_0 = 10^{-3}$. Since the situation is symmetric for the given parameter values, the wavenumbers obtained from the two quasienergies $\varepsilon^{\pm}$ have equal magnitudes but are antiparallel to each other, cf. Fig. 3 (a). Consequently, the interference of the central band and the sideband leads to standing optical and mechanical waves of different frequency. This becomes visible in the Fourier transform $F[|t_0^m|^2](q)$, see Fig. 3 (c). The interference effects are also reflected in the periodic time-evolution of the probability current density shown in Fig. 3 (d). This is most strikingly demonstrated by the photonic current (red solid

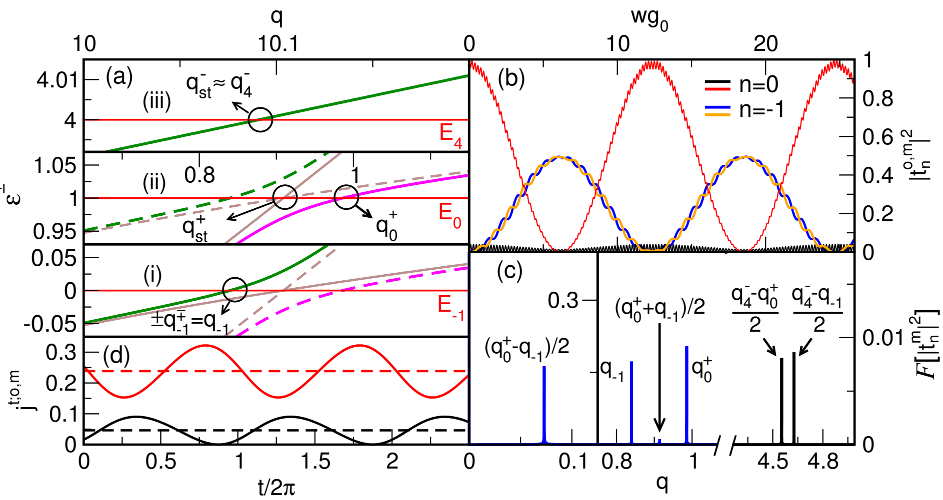

Fig. 4. (Color online) Scattering characteristics for photon energy $E = \Omega$. Notations are the same as in Fig. 3. Note that in panel (a) for case (iii), due to avoided crossings, the wavenumber q_4^- is obtained at E_4 (here, the static dispersion merges with the quasienergy). In panels (b) and (c), the blue lines correspond to the mechanical sideband $n = -1$. In panel (d) $wg_0 = 0.929$ [crossing of black and blue lines in panel (b)]. Again, $g_0 = 0.287\Omega$, $g_1 = 0.073\Omega$ with $E = \Omega$ (corresponding to $E/g_0 = 3.48$ in Fig. 1).

line), which disappears periodically because of destructive interference. The higher harmonic with frequency 2Ω is due to the interference of the sidebands $n = \pm 1$.

A similar scenario arises for a photon at resonance energy $E = \Omega$ (in Fig. 1 at $E/g_0 \approx 3.48$). Whereas for a static barrier, $g_1 = 0$, the transmission becomes almost purely photonic [cf. Fig. 1, upper right panel] a small perturbation $g_1 = 0.073\Omega$ is sufficient to excite the sideband $n = -1$ [see Fig. 4 (a)]. Again, interference of the central bands and the sidebands leads to periodic transmission probabilities as a function of wg_0, especially for the mechanical sideband, see Fig. 4 (b). The Fourier transformation of the mechanical mode depicted in Fig. 4 (c) reveals which wavenumbers are involved in the scattering process. Just as for the photon current in Fig. 3 (d), the interference of the mechanical side and central band leads to the suppression of the current density of the phonon periodically in time, see Fig. 4 (d).

Conclusions. In optomechanical Dirac materials scattering of plane photon waves by laser-induced oscillating planar barriers becomes inelastic. Finite transmission probabilites for the optical and mechanical sidebands lead to a suppression or revivial of light-sound interconversion for photon energies close to multiple integers of the oscillation frequency. Using parameter values of recent experiments [1,5], these effects will appear even for weak couplings with oscillation frequencies of about 0.5MHz. Therefore, our work could be of particular interest for future (quantum) optical applications, especially for the experimental realization of an interface between microwave photons and phonons using laser barriers. It would be desirable to extend this study to more realistic quantum-dot geometries. This will be the subject of future work.

References

1. M. Schmidt, V. Peano, F. Marquardt, New Journal of Physics **17**, 023025 (2015)
2. C. Wurl, H. Fehske, Scientific Reports **7**, 9811 (2017)
3. C. Schulz, R. L. Heinisch, H. Fehske, Phys. Rev. B **91**, 045130 (2015)
4. Jon H. Shirley, Jon H., Phys. Rev. **138**, B979–B987 (1965)
5. A. H. Safavi-Naeini, O. Painter, Opt. Express **18**, 14926–14943 (2010)

PHYSICAL REVIEW A **00**, 003800 (2018)

Floquet scattering of light and sound in Dirac optomechanics

C. Wurl* and H. Fehske†
Institut für Physik, Universität Greifswald, D-17487 Greifswald, Germany

(Received 23 August 2018; published xxxxxx)

The inelastic scattering and conversion process between photons and phonons by laser-driven quantum dots is analyzed for a honeycomb array of optomechanical cells. Using Floquet theory for an effective two-level system, we solve the related time-dependent scattering problem, beyond the standard rotating-wave approximation approach, for a plane Dirac-photon wave hitting a cylindrical oscillating barrier that couples the radiation field to the vibrational degrees of freedom. We demonstrate different scattering regimes and discuss the formation of polaritonic quasiparticles. We show that sideband-scattering becomes important when the energies of the sidebands are located in the vicinity of avoided crossings of the quasienergy bands. The interference of Floquet states belonging to different sidebands causes a mixing of long-wavelength (quantum) and short-wavelength (quasiclassical) behavior, making it possible to use the oscillating quantum dot as a kind of transistor for light and sound. We comment under which conditions the setup can be utilized to observe *zitterbewegung*.

DOI: 10.1103/PhysRevA.00.003800

I. INTRODUCTION

Optomechanical systems realizing the interaction between light and matter on the micro- and macroscale [1] enjoy continued interest since they allow for the study of fundamental questions concerning, e.g., the cooling of nanomechanical oscillators into the quantum ground state [2–4], nonlinear phenomena on the route from classical [5,6] to quantum behavior [7–9], and even entanglement [10,11] and (quantum) information processing [12–15]. Regarding the latter one, optomechanical crystals or arrays [16–19] have gained particular attention as they accommodate (strongly) coupled collective modes [20–22], and therefore can be utilized for the transport, storage, and transduction of photons and phonons [23–27].

A promising building block for hybrid photon-phonon signal processing architectures is provided by planar optomechanical metamaterials. Their optically tunable, polaritonlike band structure enables versatile and easy to implement applications of artificial optomechanical gauge fields [28–30] and topological phases of light and sound [31]. In this context, the emergence of Dirac physics was demonstrated for low-energy photons and phonons in "optomechanical graphene," that is, a honeycomb array of optomechanical cells [32]. In these systems ultrarelativistic transport phenomena such as Klein tunneling appear, because of the chiral nature of the quasiparticles and their Dirac-like band structure, just as for Dirac electrons in graphene. Moreover, the radiation pressure that induces the coupling between photons and phonons inside the optomechanical barrier can be easily tuned by the laser power and may cause the formation of (photon-phonon) polariton states mixing photonic and phononic contribution. Circular barriers are of special interest because they are easier to implement experimentally than infinite planar barriers and show a richer scattering behavior due to their finite size. In particular such optomechanical "quantum dots" may cause the spatial and temporal trapping, Veselago lensing, a depletion of Klein tunneling, and angle-dependent interconversion of photons and phonons [33].

Since transport of Dirac quasiparticles is extremely energy-sensitive, external time-dependent fields may produce interesting effects. This has been demonstrated for the photon-assisted transport in graphene-based nanostructures [34], where planar and circular electromagnetic potentials, oscillating with frequency Ω, give rise to inelastic scattering processes by exchanging energy quanta $n\hbar\Omega$ with the oscillating field. Thereby, the excitation into and interference between sideband states may cause the suppression of (Klein) tunneling, Floquet-Fano resonances, as well as highly anisotropic angle-resolved transmission and emission of the quasiparticles [35–40]. Also the relevance to *zitterbewegung* (ZB) has been addressed within the Tien-Gordon setup [41].

As stressed already, inside the optomechanical barrier polaritonic quasiparticles will form. They can be treated effectively as two-level systems. Then, modulating the coupling strength in a time-periodic way, the system mimics a two-level system driven by a linear polarized laser field. Within Floquet theory, it was shown that such systems exhibit strongly enhanced transmission probabilities between the two levels whenever avoided crossings occur in the quasienergy bands [42–44]. This immediately raises the question how Floquet-driven barriers affect the two-level scattering process in optomechanical metamaterials. For planar oscillating barriers we found that the finite transmission probabilities for the sidebands might suppress or revive the light-sound interconversion when the energy of the incident photon is close to multiples of the oscillation frequency [45].

Motivated by these findings, in the present paper we study the inelastic scattering and conversion process between photons and phonons triggered by periodically oscillating quantum dots, imprinted optically in optomechanical graphene.

*wurl@physik.uni-greifswald.de
†fehske@physik.uni-greifswald.de

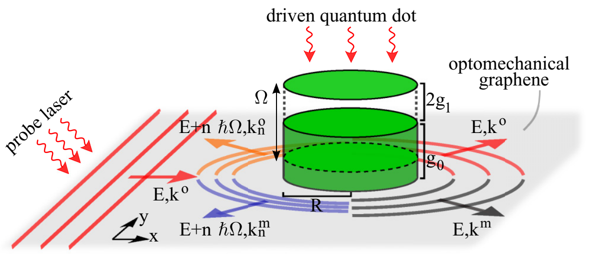

FIG. 1. Sketch of the scattering setup. Injected by a probe laser, an incident optical wave with energy $E > 0$ and wave vector $\boldsymbol{k}^o = k^o \boldsymbol{e}_x$ hits a laser-driven quantum dot of radius R. Inside the dot, the photon-phonon coupling is $g = g_0 - 2g_1 \cos(\Omega t)$. As a result, reflected optical and mechanical waves appear with wave vectors $\boldsymbol{k}^{o/m}$ ($\boldsymbol{k}_{n=0} \equiv \boldsymbol{k}$), in the central band with energy E, and in the sidebands with energies $E_n = E + n\hbar\Omega$, where $n = \pm 1, \pm 2, \ldots$. The reflected waves are directed away from the dot and carry an angular momentum. Since the dot allows for the conversion between light and sound, mechanical waves appear outside the dot even though the coupling vanishes here. Note that the figure is not true to scale and, since $v_o > v_m$, the photon-phonon wave vectors $k_n^{o/m} = |E_n|/\hbar v_{o/m}$ are not equal in magnitude.

Figure 1 illustrates the setup under consideration. The paper is organized as follows. Section II presents our model and outlines the theoretical approach, based on Floquet theory for an effective two-level system. The solution of the related time-dependent scattering problem is explicitly given. A more detailed presentation of the (numerical) implementation of our Floquet approach can be found in the appendix. In Sec. III, after briefly recapitulating previous findings for the static quantum dot, we discuss the numerical results obtained for the oscillating quantum dot in the whole range of system parameters. The relevance for observing ZB is also considered. Our main conclusions can be found in Sec. IV.

II. THEORETICAL APPROACH

A. Model

In optomechanical graphene, driven by a laser with frequency $\omega_{\rm las}$, co-localized cavity photon (eigenfrequency ω_o) and phonon (eigenfrequency ω_m) modes interact via radiation pressure. For sufficiently low energies and barrier potentials that are smooth on the scale of the lattice constant but sharp on the scale of the de Broglie wavelength (i.e., the size of the dot is much bigger than the lattice spacing in the optomechanical array), the continuum approximation applies [46]. Then the system can be described by the optomechanical Dirac-Weyl Hamiltonian [32],

$$H = \left(\overline{v} + \tfrac{1}{2}\delta v\, \tau_z\right)\boldsymbol{\sigma} \cdot \boldsymbol{k} - g(\boldsymbol{r}, t)\tau_x. \tag{1}$$

In Eq. (1), the model Hamiltonian is written in units of $\hbar$, after rescaling $H \to H - \hbar\omega_m$. Here, $\overline{v} = (v_o + v_m)/2$, $\delta v = v_o - v_m$, with $v_{o/m}$ as the Fermi velocity of the optical or mechanical mode, $\boldsymbol{\tau}$ and $\boldsymbol{\sigma}$ are Pauli spin matrices, $\boldsymbol{k}$ ($\boldsymbol{r}$) gives the wave vector (position vector) of the Dirac wave, and $g(\boldsymbol{r}, t)$ parametrizes the time-dependent photon-phonon coupling strength. On the other hand, when the laser continuously drives a certain region of the honeycomb lattice, a quantum barrier with time-independent coupling strength g_0 is created.

We note that the above single-valley Hamiltonian is obtained after linearizing the dynamics around the steady-state solution and taking advantage of the rotating-wave approximation (RWA) in the red detuned moderate-driving regime, $\Delta = \omega_{\rm las} - \omega_o = -\omega_m$ [32]. To account for inelastic scattering, we assume the laser amplitude to be modulated with a frequency much smaller than the frequencies of both the laser and mechanical modes, $\Omega \ll \omega_{\rm las}, \omega_m$ (otherwise the RWA is not granted). Furthermore, Ω should be much smaller than the mechanical hopping in the array, i.e., $\Omega < 2v_m/3a$ with a as the lattice constant (otherwise the continuum approximation is not granted) [32]. Then, using polar coordinates, the photon-phonon coupling in the quantum dot region with radius R takes the form,

$$g(r, t) = [g_0 - 2g_1 \cos(\Omega t)]\Theta(R - r), \tag{2}$$

where $g_0 > 0$ and $g_1 < 0$, and $g_{0,1}$ are assumed to be constant. Furthermore, in order to ensure a laser amplitude greater than zero, $2|g_1| \leqslant g_0$. In what follows, for the sake of simplicity, the potential barrier (2) is assumed to be infinitely sharp. Numerical studies have shown that a more realistic steep but rounded barrier will influence the results little (due to the small Umklapp scattering) [32].

At this point we should mention that the Hamiltonian (1), derived for the linear regime within the RWA, takes into account dissipation effects in an effective way [1,32]. Accordingly, the quasiparticles described by the model (1) propagate as undamped optical and mechanical excitations on the honeycomb lattice. As shown in Ref. [32] the main effect of dissipation would be the decay of the field amplitudes. For the same reason, the barrier is described by the optomechanical coupling strength g (being proportional to the laser amplitude) and not by the single-photon coupling rate.

Inside the quantum dot, where the photon-phonon coupling is finite, the polariton quasiparticle states are superpositions of optical and mechanical eigenstates of τ_z. Given the time-periodic coupling (2), the polariton states can be treated as periodically driven two-level systems. A similar approach is widely used in quantum optics (Rabi model), e.g., in order to model atoms or superconducting qubits driven by a semiclassical, linearly polarized laser field (see Ref. [47] and references cited therein). There it is convenient to obtain the time-dependent solutions within the RWA, which is justified for laser frequencies close to the transition frequency between the two energy levels of the state. In view of solving the scattering problem, however, the RWA cannot be applied because the wave number k, which enters the transition frequency between the two polariton states, $\delta v k/2$ in (1), changes as a result of inelastic scattering processes. Therefore we make use of the Floquet formalism to find the time-dependent solutions of our scattering problem. The Floquet formalism is described, e.g., in Refs. [44,47,48]; for its application to two-level systems see Refs. [42,43,49].

B. Formulation of the Floquet scattering problem

Treating the inelastic scattering problem we look for solutions $|\psi(t)\rangle$ of the time-dependent Dirac equation $i(\partial/\partial t)|\psi(t)\rangle = H|\psi(t)\rangle$. Since the Hamiltonian is time periodic, according to Floquet's theorem [50], we write the time-dependent solution as $|\psi(t)\rangle = \mathrm{e}^{-i\varepsilon t}|\varepsilon(t)\rangle$ with quasienergy ε and the time-periodic Floquet state $|\varepsilon(t)\rangle = |\varepsilon(t+T)\rangle$, where $T = 2\pi/\Omega$. For constructing the latter we use the eigensolutions in the absence of the oscillating barrier [32,33], which are given as $|\tau\rangle\,|\sigma,\boldsymbol{k}\rangle$. Here, $|\sigma,\boldsymbol{k}\rangle$ is the eigenvector of the single-particle Dirac-Weyl Hamiltonian $H = \boldsymbol{\sigma k}$ with eigenvalue $\sigma|\boldsymbol{k}|$ and sublattice pseudospin $\sigma = \pm 1$ (in this notation σ acts as a band index). The polariton state is formed according to $|\tau\rangle = \mathcal{N}^\tau(g_0\,|o\rangle + \gamma^\tau\,|m\rangle)$, where $\tau = \pm 1$ denotes the polariton pseudospin, and $|o/m\rangle$ are the bare optical and mechanical eigenstates of τ_z (the factors $\mathcal{N}^\tau$ and γ^τ are given in the appendix). Expanding the Floquet state in a Fourier series,

$$|\varepsilon(t)\rangle = \sum_p \sum_{\tau=\pm} c_p^\tau\,|\tau\rangle\,|\sigma,\boldsymbol{k}\rangle\,e^{ip\Omega t}, \qquad p \in \mathbb{Z}, \tag{3}$$

the two polariton states with $\tau = \pm 1$ have to be superimposed because of the optomechanical coupling in τ space. Inserting the ansatz (3) into the time-dependent Dirac equation yields the Floquet eigenvalue equation (FEE) $\mathcal{F}\boldsymbol{c} = \varepsilon\boldsymbol{c}$, where $\boldsymbol{c}$ is the vector containing the Fourier coefficients c_p^τ, and $\mathcal{F}$ is the Floquet matrix having eigenvalues ε. The Floquet matrix and the FEE in component form are given in the appendix; see Eq. (A5) and Eq. (A1), respectively. In general, an analytical solution of the FEE does not exist [47]. This is in contrast to the scattering of graphene electrons by time-periodic gate-defined potential barriers, for which the diagonal potential in sublattice space allows one to integrate the Dirac equation [34,36,40,41]. We therefore determine the solutions of the FEE numerically; see appendix.

Let us take another look at the Floquet-scattering setup depicted in Fig. 1. Since the oscillating quantum dot gives (takes) energy to (away from) photons and phonons in the form of multiple integers of the oscillation frequency, $E_n = E + n\Omega$ ($n \in \mathbb{Z}$), the scattering is inelastic. This implies that the wave functions have to be expressed as superpositions of states with energies E_n. This is certainly unproblematic outside the dot, where the coupling is zero and we can use the unperturbed eigensolutions. The transmitted wave inside the dot, however, is composed of Floquet states according to Eq. (3). On that account the wave numbers $q_n^{(\pm)}$ and the Fourier coefficients $c_{p,n}^{\tau,(\pm)}$ at each energy $E_n = \varepsilon^{(\pm)}$ have to be determined by numerical diagonalization of the Floquet matrix $\mathcal{F}$. Note that the index $(\pm)$ appears because the quasienergies are twofold degenerate owing to the polariton pseudospin τ.

C. Solution of the Floquet scattering problem

For this purpose, we expand the plane wave state of the incoming photon in polar coordinates,

$$\begin{aligned}|\psi^{in}\rangle &= \frac{1}{\sqrt{2}}\begin{pmatrix}1\\1\end{pmatrix}e^{ik^o x}\,|o\rangle\,e^{-iEt}\\ &= \sum_{n,l}\delta_{n0}\,\phi_{n,l}^{(1)}(k_n^o r)\,|o\rangle\,e^{-iE_n t},\end{aligned} \tag{4}$$

where $l \in \mathbb{Z}$ is the quantum number referring to the angular momentum. The reflected (scattered) wave consists of optical and mechanical modes, $|\psi^r\rangle = |\psi^{r;o}\rangle + |\psi^{r;m}\rangle$ (cf. Fig. 1), with

$$|\psi^{r;o/m}\rangle = \sum_{n,l}\sqrt{\frac{v_o}{v_{o/m}}}\,r_{n,l}^{o/m}\,\phi_{n,l}^{(3)}\big(k_n^{o/m} r\big)\,|o/m\rangle\,e^{-iE_n t}. \tag{5}$$

Here, $r_{n,l}^{o/m}$ are the optical and mechanical reflection coefficients. According to Eq. (3), the transmitted wave $|\psi^t\rangle = |\psi^{t;(+)}\rangle + |\psi^{t;(-)}\rangle$ reads

$$|\psi^{t;(\pm)}\rangle = \sum_{n,l} t_{n,l}^{(\pm)}\phi_{n,l}^{(1)}\big(q_n^{(\pm)}r\big)\sum_p\sum_{\tau=\pm} c_{p,n}^{\tau,(\pm)}\,|\tau\rangle_n^{(\pm)}\,e^{-iE_{n-p}t}, \tag{6}$$

where $t_{n,l}^{(\pm)}$ are the transmission coefficients. The Fourier coefficients and wave numbers used in Eq. (6) are extracted from the Floquet approach outlined in the appendix. For the wave functions (4)–(6) we have used the eigenfunctions $\langle\boldsymbol{r}|\sigma,\boldsymbol{k}\rangle$ of the Dirac-Weyl Hamiltonian [40,51,52],

$$\phi_{n,l}^{(1,3)}(k_n r) = \frac{1}{\sqrt{2}}i^{l+1}\begin{pmatrix}-i\,\mathcal{Z}_l^{(1,3)}(k_n r)e^{il\varphi}\\ \sigma_n\mathcal{Z}_{l+1}^{(1,3)}(k_n r)e^{i(l+1)\varphi}\end{pmatrix}, \tag{7}$$

where $\mathcal{Z}^{(1)} = J_l$ and $\mathcal{Z}^{(3)} = H_l$ denotes the Bessel function and Hankel function, respectively. To ensure that the group velocity of the reflected wave is directed away from the quantum dot (as it should be for an outgoing wave), the sign of the energy determines which kind of Hankel function is used: $H_l = J_l + i\sigma_n^{\mathrm{out}}Y_l$ (Y_l is the Neumann function). Here, $\sigma_n^{\mathrm{out}} = \mathrm{sgn}(E_n)$ is the "band index" outside the quantum dot. Its presence in the Hankel function ensures that the refractive indices are negative for negative energies, meaning that the wave vector is directed opposite the propagation direction of the particle. For the transmitted wave inside the dot, $\sigma_n^{\mathrm{ins}} = \pm 1$ for $E_n \gtrless \pm g_0$, and $\sigma_n^{\mathrm{ins}(\pm)} = \pm 1$ for $-g_0 \leqslant E_n \leqslant g_0$. Matching the wave functions at $r = R$ yields the equations for the transmission coefficients:

$$\delta_{p0}W_{p,l}^o = \sum_n\sum_{\tau=\pm} t_{n,l}^{(\tau)} f_{n-p,n}^{(\tau)} X_{n,p,l}^{o,(\tau)}, \tag{8a}$$

$$0 = \sum_n\sum_{\tau=\pm} t_{n,l}^{(\tau)} h_{n-p,n}^{(\tau)} X_{n,p,l}^{m,(\tau)}. \tag{8b}$$

The reflection coefficients can be obtained from

$$r_{p,l}^o = \sum_n\sum_{\tau=\pm} t_{n,l}^{(\tau)} f_{n-p,n}^{(\tau)}\frac{\mathcal{Z}_l^{(1)}\big(q_n^{(\tau)}R\big)}{\mathcal{Z}_l^{(3)}\big(k_p^o R\big)} - \delta_{p0}\frac{\mathcal{Z}_l^{(1)}\big(k_p^o R\big)}{\mathcal{Z}_l^{(3)}\big(k_p^o R\big)}, \tag{9a}$$

$$r_{p,l}^m = \sum_n\sum_{\tau=\pm} t_{n,l}^{(\tau)} h_{n-p,n}^{(\tau)}\frac{\mathcal{Z}_l^{(1)}\big(q_n^{(\tau)}R\big)}{\mathcal{Z}_l^{(3)}\big(k_p^m R\big)}. \tag{9b}$$

Here, we have used the abbreviations,

$$W_{p,l}^o = \mathcal{Z}_l^{(1)}\big(k_p^o R\big)\mathcal{Z}_{l+1}^{(3)}\big(k_p^o R\big) - \mathcal{Z}_{l+1}^{(1)}\big(k_p^o R\big)\mathcal{Z}_l^{(3)}\big(k_p^o R\big), \tag{10a}$$

$$\begin{aligned}X_{n,p,l}^{o/m,(\tau)} &= \sigma_p^{\mathrm{out}}\mathcal{Z}_l^{(1)}\big(q_n^{(\tau)}R\big)\mathcal{Z}_{l+1}^{(3)}\big(k_p^{o/m}R\big)\\ &\quad - \sigma_n^{\mathrm{ins}(\tau)}\mathcal{Z}_{l+1}^{(1)}\big(q_n^{(\tau)}R\big)\mathcal{Z}_l^{(3)}\big(k_p^{o/m}R\big),\end{aligned} \tag{10b}$$

and

$$f^{(\tau)}_{n-p,n} = \sum_{\tau'} c^{\tau',(\tau)}_{n-p,n} \mathcal{N}^{\tau',(\tau)}_n g_0, \tag{11a}$$

$$h^{(\tau)}_{n-p,n} = \sum_{\tau'} c^{\tau',(\tau)}_{n-p,n} \mathcal{N}^{\tau',(\tau)}_n \gamma^{\tau',(\tau)}_n. \tag{11b}$$

When solving the infinite-dimensional coupled linear system (8) numerically, we raise the dimension of the coefficient (scattering) matrix until convergence is reached. This is most challenging for large g_1 or small Ω, since the dimension of the scattering matrix is mainly determined by the ratio $|g_1|/\Omega$ (cf. appendix).

The inelastic scattering and conversion process between photons and phonons is characterized by the scattering efficiency $Q^{o/m}(r,t)$, that is, the scattering cross section divided by the geometric cross section. It consists of a time-averaged part,

$$\overline{Q}^{o/m} = \sum_n \sum_{l=0}^{\infty} \overline{Q}^{o/m}_{n,l} = \sum_n \sum_{l=0}^{\infty} \frac{4}{k^{o/m}_n R} \left| r^{o/m}_{n,l} \right|^2, \tag{12}$$

and a time-dependent part (to simplify the notation, we omit the index out in σ^{out}_n),

$$\tilde{Q}^{o/m}(r,t) = \sum_{n<n'} \sum_{l=0}^{\infty} (-1)^l \frac{4}{\sqrt{k^{o/m}_n k^{o/m}_{n'}} R} \times 2\mathrm{Re}\left\{ \left(r^{o/m}_{n',l}\right)^* r^{o/m}_{n,l}\, i^{\frac{1}{2}(\sigma_{n'}-\sigma_n)}\, e^{i(n-n')\Omega\vartheta^{o/m}} \right\}. \tag{13}$$

Here, $\vartheta^{o/m} = r/v_{o/m} - t$ denotes the time-retarded phase factor. In Eqs. (12) and (13), and hereafter, $l \geqslant 0$. The quantities $\overline{Q}^{o/m}_{n,l}$ in Eq. (12) represent the scattering contributions of the partial wave l and the sideband n. In the far field, the scattering efficiency is obtained from the radial component of the current density of the reflected wave, $(1/2R) \int j^{r;o/m}_r(r,t) r d\varphi$ [33,40,51,52]

$$\begin{aligned} j^{r;o/m}_r(r,t) = {} & \sum_{n,n'} \sum_{l,l'} \frac{4 v_o}{\pi \sqrt{k^{o/m}_n k^{o/m}_{n'}}\, r} \left(r^{o/m}_{n',l'}\right)^* r^{o/m}_{n,l} \\ & \times i^{l-l'} i^{\frac{1}{2}(\sigma_{n'}-\sigma_n)} i^{(l+l')\mathrm{sgn}(\sigma_{n'}-\sigma_n)+(l'-l)\mathrm{sgn}(\sigma_{n'}+\sigma_n)} \\ & \times \{\cos[(l+l'+1)\varphi] \\ & + \cos[(l-l')\varphi]\} e^{i(n-n')\Omega\vartheta^{o/m}}, \end{aligned} \tag{14}$$

which characterizes the angular scattering. In the near field, the scattering is further specified by the probability density $\rho = \langle\psi|\psi\rangle$, with $|\psi\rangle = |\psi^{in}\rangle + |\psi^r\rangle$ outside and $|\psi\rangle = |\psi^t\rangle$ inside the quantum dot. Note that in the far field, the optical or mechanical part of the probability density of the reflected wave $\langle\psi^r|\psi^r\rangle$ becomes equal to the current density (14) except for a constant factor $v_{o/m}$. Furthermore, defining the scattering efficiency by the cross section, only the incident current of the photon was used, since no phonon incident currents exist (cf. Fig. 1). Therefore, the scattering efficiency of the phonon Q^m can be understood as an interconversion rate between photons and phonons, which we can define as Q^m/Q^o.

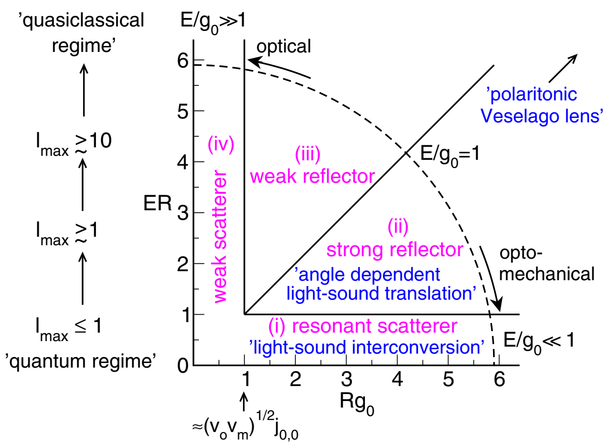

FIG. 2. Different scattering regimes for the static quantum dot in dependence on the strength parameter Rg_0 and the size parameter ER. The latter determines the maximum angular momentum $l_{\max}$ being possible in the scattering. The energy-coupling ratio E/g_0 switches between the optomechanical ($E/g_0 \ll 1$) and the pure optical regime ($E/g_0 \gg 1$), where the optomechanical (optical) regime is characterized by the interconversion rate $Q^m/Q^o \sim 1$ ($\ll 1$). Depending on these parameter ratios the static dot acts as a (i) resonant scatterer in the quantum regime, (ii) strong reflector, (iii) weak reflector, or (iv) weak scatterer. On the axis of abscissae the first resonance point derived from the resonance condition (15) with $l=0$ is marked.

III. NUMERICAL RESULTS

Since the scattering problem worked out in the preceding section is invariant under the transformation $[E, g_{0,1}, \Omega, R^{-1}] \rightarrow \gamma[E, g_{0,1}, \Omega, R^{-1}]$ with $\gamma \in \mathbb{R}$, we rescale the equations of motion such that $\Omega = 1$ [45]. We set $v_o = 10 v_m$ and furthermore employ units such that $v_o = \hbar = 1$ [32,33,45]. Then, the rescaled variables are dimensionless and related to the unscaled variables (marked by ˆ) according to $E = \hat{E}/(\hbar\Omega)$, $g_{0,1} = \hat{g}_{0,1}/\Omega$, $R = \hat{R}\Omega/v_o$, $k = \hat{k}v_o/\Omega$. The phase factor is measured in units of Ω, $\vartheta^{o/m} = \hat{\vartheta}^{o/m}\Omega$. According to the experimental parameters given in Ref. [17] the effects discussed in this paper should be observable for oscillation frequencies $\Omega \sim 0.5$ MHz $\ll \omega_{\text{las}}$, where we have assumed a laser-enhanced optomechanical coupling strength $\hat{g}_0 \sim 0.1$ MHz with $2|\hat{g}_1| \lesssim \hat{g}_0$. Then, without violating the continuum approximation, the energies of the photon and the phonon are in the order of $\hbar\omega_m$ (microwaves) with excitation energies $n\Omega \sim$ MHz $\ll \omega_m$ for the sidebands. The typical size of the quantum dot radius is $100a$ with lattice constant $a \sim 50\ \mu$m. Using these parameters the photon tunneling rate J between two sites [32] has to be made small by design: $J = 2v_o/3a \sim 10^{-2}\omega_m$.

A. Static quantum dot

The scattering problem of the static dot ($g_1 = 0$) has been analyzed in previous work [33]. Depending on the strength parameter Rg_0 and the size parameter ER, different scattering regimes occur. They can be characterized by the scattering efficiency; see Fig. 2. This schematic figure is taken as a starting point, helping us to classify the different parameter regimes and expected physical phenomena in the theoretical discussion below.

Comparing the scattering regimes of our optomechanical quantum dot (Fig. 2) with those of electrons in graphene scattered by gate-defined quantum dots (cf. Fig. 3 in Ref. [53]), strong similarities could be identified, which perhaps is not surprising in view of the close relation between both Hamiltonians. The most crucial difference is the nondiagonal optomechanical coupling, which allows the quantum dot to translate light into sound. The interconversion rate Q^m/Q^o is determined by the energy-coupling ratio E/g_0 (see Fig. 3 in [33]) and discriminates between the optomechanical and purely optical regimes (dashed line in Fig. 2). For $E/g_0 \ll 1$, i.e., in the resonant scattering (quantum) regime, the size parameter is small for not too large radii ($ER \ll 1$), so the excitation of the first partial waves leads to sharp resonances in the scattering efficiency of the photon, and of the phonon accordingly. The resonance condition is

$$Rg_0 = \sqrt{v_o v_m}\, j_{l,i}, \tag{15}$$

where $j_{l,i}$ denotes the ith zero of the Bessel function J_l with $i = 0, 1, 2, \ldots$ (the onset of the resonant scattering regime is marked by an arrow in Fig. 2). Resonances are featured by quasibound states in the quantum dot and preferred scattering directions in the far field (cf. Fig. 4 in [33]). Increasing E/g_0 the phonon is hardly scattered and the scattering becomes weaker. In the limit $E/g_0 \gg 1$, the scattering becomes purely photonic because $v_o \ll v_m$. At such high photon energies the scattering of the phonons disappears since the corresponding refractive index is almost one. At the same time more and more partial waves will be excited, which leads to a richer angular distribution of the radiation characteristics and the possibility of Fano resonances (cf. Figs. 5 and 6 in [33]). At very large size parameters, $ER \gg 1$, the wavelengths will be much smaller than the radius of the quantum dot and the quasiclassical regime is entered. There, for $E/g_0 < 1$, the quantum dot may act as a polaritonic Veselago lens with negative refractive indices, focusing the light beam in forward direction.

B. Oscillating quantum dot

As already mentioned above, an oscillating quantum dot causes inelastic scattering via sideband excitations $E_n = E + n\Omega$ for both photons and phonons. Hence, besides the angular momentum l, the sideband-energy quantum number n becomes important. Accordingly the scattering regimes are no longer determined by ER and E/g_0, but by effective size parameters $E_n R$ and effective energy-coupling ratios E_n/g_0. The number of sidebands involved in the scattering is mainly determined by the ratio $|g_1|/\Omega$. This means, discussing the physical behavior of our setup, an additional parameter comes into play. To avoid that the sideband-excitation energies become too large and the continuum approximation is no longer justified possibly, in particular for the phonon with $v_m \ll v_o$, we restrict ourselves to values of g_0 and $|g_1|/2$ smaller than $\Omega/2$.

Before analyzing the scattering problem in detail, we want to make a general remark concerning our Floquet state approach. In the main, scattering is determined by the refractive indices, that is to say by the different wave numbers inside and outside the scattering region. If the wave numbers inside and outside the quantum dot are the same, scattering disappears. The other way around, strong scattering takes place for large differences between the wave numbers belonging to the static and nonstatic cases. Clearly the deviation is greater the larger the value of the coupling $|g_1|$. Furthermore, inspecting the quasienergies as a function of the wave number $\varepsilon(q)$, one finds the most significant deviations close to the avoided crossings (see Fig. 12 in the appendix). Such avoided crossings appear when two energy bands of the static case with different value of τ, and maybe shifted by Ω, cross each other. For $g_0 \leqslant \Omega/2$, these crossing energies (CE) are

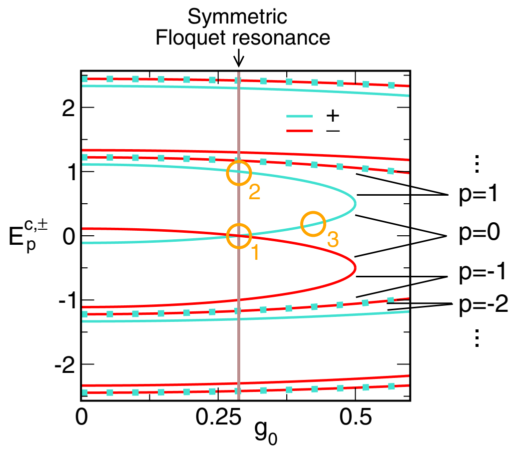

FIG. 3. Crossing energies (CE) according to Eq. (16). Note that in some cases CE with different p coincide (such situation is marked by points). Symmetric Floquet-resonant scattering occurs at $g_0 = \Omega\sqrt{v_o v_m}/(v_o + v_m) \simeq 0.287\Omega$. Circles designate particular energy-coupling ratios: (1) $E/g_0 = 10^{-4}$ ($E \simeq 0$), (2) $E/g_0 \simeq 3.48$ ($E = 10^{-3} g_0 + 1\Omega \simeq \Omega$), and (3) $E/g_0 \simeq 0.31$ ($E = 0.123\Omega$ at $g_0 = 0.394\Omega$). They correspond to different scattering regimes of the static dot in Fig. 2: (1) → (i), (2) → (iii), (3) → (ii).

$$E_p^{c,\pm} = \pm \frac{p'}{|p'|}\frac{\bar{v}}{\delta v}\sqrt{(p'\Omega)^2 - 4g_0^2} \pm \frac{\Omega}{4}[1 + (-1)^{p'+1}], \tag{16}$$

with $p' = p$ for $\pm p \geqslant 1$ and $p' = p \mp 1$ for $\pm p \leqslant 0$, where $p \in \mathbb{Z}$. Again, the polariton degree of freedom of the CE is marked by the index $\pm$. Figure 3 shows the CE depending on g_0. Since the influence of the oscillating barrier on the scattering is greatest for $E \sim E_p^{c,\pm}$, the further discussion follows these cases marked in Fig. 3, and the subsections are numbered accordingly.

1. *Symmetric Floquet-resonant scattering close by* $E \simeq 0$

For $g_0 = \Omega\sqrt{v_o v_m}/(v_o + v_m)$ and an incident photon energy close to the neutrality point, $E \simeq 0$ [case (1) in Fig. 3], the static dot is a resonant scatterer (quantum regime) which makes light-sound conversion possible [regime (i) in Fig. 2]. Since the CE with $p = \pm 1$ are shifted by $\pm\Omega$ with respect to the $p = 0$ CE and the energies E_n are also shifted by multiples of Ω among themselves, we call the scattering

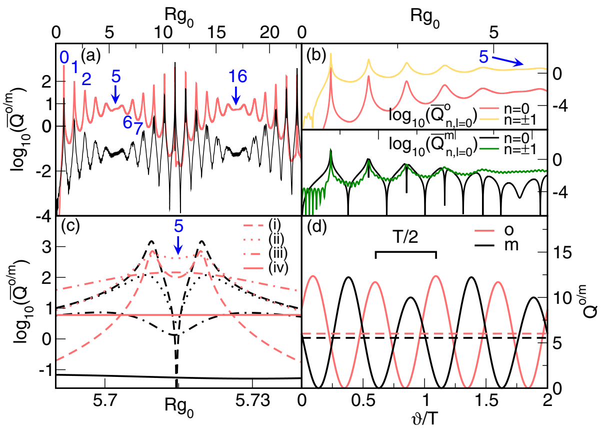

FIG. 4. Scattering efficiency at weak coupling, $|g_1| \ll \Omega$. To realize symmetric Floquet resonance for $E \simeq 0$ [case (1) in Fig. 3] we set $E = 10^{-4} g_0 \simeq 0$, $g_0 = \Omega\sqrt{v_o v_m}/(v_o + v_m) \simeq 0.287\Omega$, and $|g_1| = 0.02\Omega$ [except for (c)]. (a) Time-averaged scattering efficiency of the photon (red/gray) and the phonon (black), with resonance points $i = 0, 1, \ldots$ of the static quantum dot for $l = 0$ according to Eq. (15) (blue numbers). (b) Different contributions to the scattering efficiency of (a). (c) Enlarged scattering efficiency close to $i = 5$ for (i) $g_1 = 0$, (ii) $|g_1| = 2 \times 10^{-3}\Omega$, (iii) $|g_1| = 5 \times 10^{-3}\Omega$, and (iv) $|g_1| = 0.02\Omega$. (d) Time-averaged scattering efficiency (dashed) and time evolution of the scattering efficiency at $i = 5$, corresponding to case (iv) in (c) (here Q_m is multiplied by a factor of 100).

"Floquet resonant." We find that different CE with $p = 0$ cross at $E = 0$, which entails antiparallel wave vectors of equal magnitudes inside the dot (see Fig. 12 in the appendix). In principle, the same argumentation applies to the sideband energies $E_{\pm n}$, which is why we call this situation "symmetric."

Weak photon-phonon coupling. Figure 4 contrasts the (time-averaged) scattering efficiency of the photon and the phonon at weak couplings, i.e., in the (antiadiabatic) limit $2|g_1| \ll \Omega$. Obviously, the scattering efficiency of the static dot, with its resonances of the lowest partial wave $l = 0$, is retained to a certain extent [see Fig. 4(a)]. The resonances of the static dot can be related to minima in the scattering efficiency ($i = 6, 7, \ldots$). Most notably, at certain points ($i = 5, 16, \ldots$) the scattering is off resonant, with the result that light-sound interconversion is strongly suppressed ($\overline{Q}^m/\overline{Q}^o \ll 1$). Although not shown here, the positions of off-resonances are moving closer together, and towards smaller values of Rg_0, if g_1 is increased. This can be ascribed to a Fabry-Pérot interference between waves with different wave numbers inside the dot [45].

Figure 4(b) gives the individual contributions to the total scattering efficiency depicted in Fig. 4(a). Whereas in the static case the scattering is determined by the central band $n = 0$, for finite values of g_1 the sidebands $n = \pm 1$ are involved [sidebands with $|n| > 1$ (not shown) play a minor role only]. Due to the symmetry of the problem for $E \to 0$, the $n = \pm 1$ sideband contributions are equal in magnitude; $|r^{o/m}_{n=1,l}| \simeq |r^{o/m}_{n=-1,l}|$. We find that for these sidebands only the lowest partial wave with $l = 0$ is excited, although the effective size parameter might suggest the opposite: $E_{n=\pm 1} R \simeq \pm\Omega R \gg 1$. We will come back to that later. We further observe that the sidebands have large impact on the scattering, even though the coupling is weak. This applies in particular to the off-resonance situation $i = 5$, where the scattering is dominated by the sidebands for both photons and phonons. Apparently the occurrence of off-resonances featured by weak scattering efficiency are a direct consequence of the presence of sidebands. Since the effective energy-coupling ratio of the central band $E_{n=0}/g_0 \simeq 0$ and the sidebands $|E_{n=\pm 1}|/g_0 \simeq 3.48$ lie within different scattering regimes (cf. Fig. 2), their interplay may lead to a partial transition from the resonant scattering regime to the weak reflection regime [(i)–(iii) in Fig. 2], accompanied by a suppression and revival of light-sound interconversion.

To monitor how the scattering resonance of the static dot gradually dissolves and is replaced by an off-resonance, Fig. 4(c) displays the time-averaged scattering efficiency in the vicinity of resonance point $i = 5$ for different values of g_1. The resonance of the static dot [case (i)] is widely weakened for a small perturbation already [cases (ii) and (iii)], particularly for the mechanical mode. We note that the scattering resonance is characterized by two resonance peaks, occurring symmetrically about the resonance point [33]. At even larger values of g_1 the resonance almost vanishes and the scattering becomes weak and purely photonic [case (iv)].

In Fig. 4(d) the time-dependent scattering efficiency is depicted at the off-resonance ($i = 5$). According to Eq. (13), the sideband ($n = \pm 1$) interference entails a periodic time dependence of the scattering efficiency with frequency 2Ω. As a result the quantum dot switches between purely photonic and phononic emission. In a certain sense, this time-periodic oscillation is related to ZB (but see the discussion below) [41].

In Fig. 5 the time-retarded and periodic emission of light and sound by the oscillating quantum dot is illustrated by means of the probability density at $t = 0$ (top) and the time-dependent far-field current density according to Eq. (14) at $r = R$ (bottom) for parameters of Fig. 4(d). The time periodicity of the scattering efficiency displayed in Fig. 4(d) is due to the constructive and destructive interference of the reflected wave functions for the sidebands $n = \pm 1$ and gives reason to the ring structure with wavelength $\lambda_{o/m} = \pi v_{o/m}/\Omega$ in the probability density. For the photon density the incoming wave function covers this periodicity farther away from the dot where the wavelength is twice as large. Inside the dot the probability density is significantly enhanced, for both photons and phonons, which can be related to the excitation of the $l = 0$ mode [33]. Obviously, the dot captures the incident photon and partly converts it into phonons, and emits both particle waves (periodically in time) predominantly in forward direction afterwards. In the far field, this gives rise to a time-periodic current density. The absence of backscattering at $\varphi = \pi$, related to Klein tunneling, is caused by the conservation of helicity at perpendicular incidence [32,33] and is observed for time-dependent planar barriers as well [45].

Moderate photon-phonon coupling. Figure 6 shows the contributions to the time-averaged scattering efficiency of the photon in this case, where $2|g_1| \gtrsim 0.1\Omega$. Again only the $l = 0$ mode is noticeably excited. We find that scattering is still dominated by the sidebands with $n = \pm 1$; the contributions

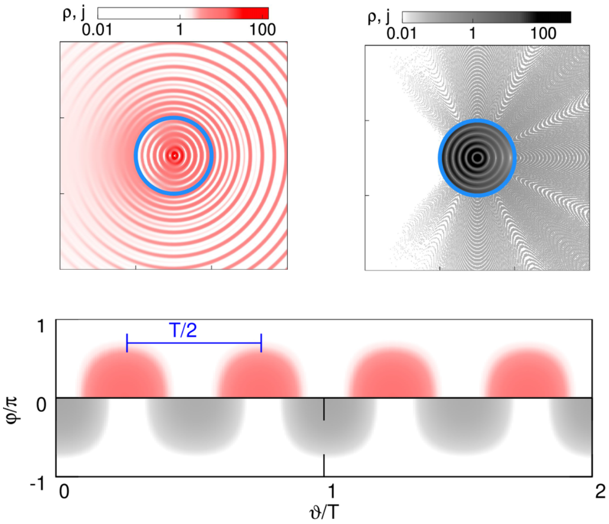

FIG. 5. Time-retarded scattering characteristics for the same parameter values as used in Fig. 4(d). Shown are the optical (red, top left) and mechanical (black, top right) parts of the probability density $\rho = \langle\psi|\psi\rangle$ inside and outside the quantum dot (marked by the blue circle) at $t = 0$, as well as the angle-resolved time evolution of the far-field current density j according to Eq. (14) (bottom) at $r = R$. For reasons of symmetry the angle dependence of the optical (mechanical) mode is given only for $\varphi \geqslant 0$ ($\varphi \leqslant 0$). Note that the ring structure occurring in the photon probability density also exists in the phonon density, but is hard to resolve due to the small wavelength of the phonon wave ($v_m = v_o/10$) (the additional structures in the phonon density arise due to undesirable aliasing effects).

of the sidebands $n = \pm 2$ are rather small and are comparable with those of the central band $n = 0$; see Fig. 6(a). Sideband contributions with $|n| > 2$ are negligible. The situation does not change much for the relatively large coupling used in Fig. 6(b). The minor significance of sidebands with $|n| > 1$ is obvious by looking at the CE in Fig. 3: Since the sideband energies $E_n = E + n\Omega \simeq n\Omega$ do not match any CE for $n > 1$, these sidebands become important only at very large g_1, when the influence of the closest CE is large enough. Figure 6 furthermore shows that off-resonances are still present and get

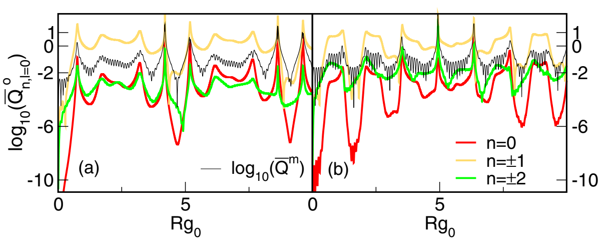

FIG. 6. Scattering contributions $\overline{Q}^{o}_{n,l=0}$ [colored (thicker) lines] at moderate couplings $|g_1| = 0.05\Omega$ (a) and $|g_1| = 0.14\Omega$ (b). Other parameter values are the same as in Fig. 4 for the symmetric Floquet-resonant situation with $E \simeq 0$ [case (1) in Fig. 3]. In addition, the time-averaged scattering efficiency of the phonon is depicted [black (thin) line].

closer for the higher coupling. This is again due to interference of waves with different wave numbers inside the dot. Hence the concomitant suppression of the light-sound interconversion at the off-resonances ($\overline{Q}^{m}/\overline{Q}^{o} \ll 1$) takes place also in the weak resonant reflection regime.

Relation to zitterbewegung. In a nutshell, ZB means the rapid and tiny fluctuations of the expectation value of the particle position (velocity) about the average path due to interference of positive and negative energy states. Although the effect has never been observed for a free electron due to the largeness of its rest energy, gapless metamaterials as (optomechanical) graphene with its Dirac-like quasiparticles provide a promising platform to observe ZB [41,54–57]. Let us briefly discuss the conditions under which ZB might be observable in our setup (for the moment, we set $v_{o/m} = 1$).

In the absence of an oscillating barrier, $g = 0$, ZB may show up in the expectation value of the velocity operator $\boldsymbol{v} = \boldsymbol{\sigma}$. Consider a general wave packet for the optical or the mechanical mode, respectively, given at $t = 0$ as the superposition of plane wave states with positive ($\sigma = +1$) and negative energy states ($\sigma = -1$): $|\psi\rangle = (1/\sqrt{2})\sum_\sigma \int a^\sigma(k,\varphi)\,|\sigma,\boldsymbol{k}\rangle\, d^2\boldsymbol{k}$. Here, $a^\sigma(k,\varphi)$ is the probability amplitude in k space. Straightforward calculation in the Heisenberg picture yields $\langle\boldsymbol{v}\rangle(t) = \langle\boldsymbol{v}\rangle_{av} + \langle\boldsymbol{v}\rangle_{\rm ZB}(t)$ where $\langle\boldsymbol{v}\rangle_{av} = \boldsymbol{e}_r \frac{1}{2}\sum_\sigma \sigma \int d^2\boldsymbol{k}|a^\sigma(\boldsymbol{k})|^2$ is the average velocity of a free, ultrarelativistic particle in polar coordinates and

$$\langle\boldsymbol{v}\rangle_{\rm ZB}(t) = -\boldsymbol{e}_\varphi \mathrm{Re}\bigg\{\int d^2\boldsymbol{k}\,[a^+(k,\varphi)]^* a^-(k,\varphi) \times [\sin(2kt) - i\cos(2kt)]\bigg\} \tag{17}$$

represents the ZB term. Equation (17) clearly shows that the interference of states with positive and negative energy is a condition for the occurrence of ZB. In addition, since the velocity operator $\boldsymbol{\sigma}$ does not act in k space $\langle\sigma',\boldsymbol{k}'|\boldsymbol{\sigma}|\sigma,\boldsymbol{k}\rangle \sim \delta(\boldsymbol{k}-\boldsymbol{k}')$, for observing ZB, states with different helicity have to be superimposed, i.e., the propagation directions of the states with positive and negative energy must be antiparallel.

Our results suggest that the setup considered here represents a realistic opportunity to observe ZB in optomechanics. Looking at the reflected wave function (5), the energetic condition for ZB can be quite simply fulfilled in the case of a symmetric Floquet resonance for photon energies at the neutrality point [see Fig. 4(b)]. Here, sideband states with positive ($E_{n=+1} \simeq +\Omega$) and negative ($E_{n=-1} \simeq -\Omega$) energy can be symmetrically excited for both the photon and the phonon, whereby the central-band state ($E \simeq 0$) fortunately is de-excited. The resulting ZB frequency of 2Ω can be made small by tuning the optomechanical coupling via the laser power ($\Omega \sim g \sim 1$ MHz by our estimates), which should be advantageous in view of an experimental implementation, just as the simple optical readout.

We argue that the other condition can easily be fulfilled by a setup where two optomechanical barriers (circular or planar) hit by photon waves from opposite directions, generated by the probe laser after passing a beam splitter. Then, in the space between the two barriers, where the reflected waves of either barrier interfere, ZB should be able to form (this is not the case for only one barrier, where the reflected waves

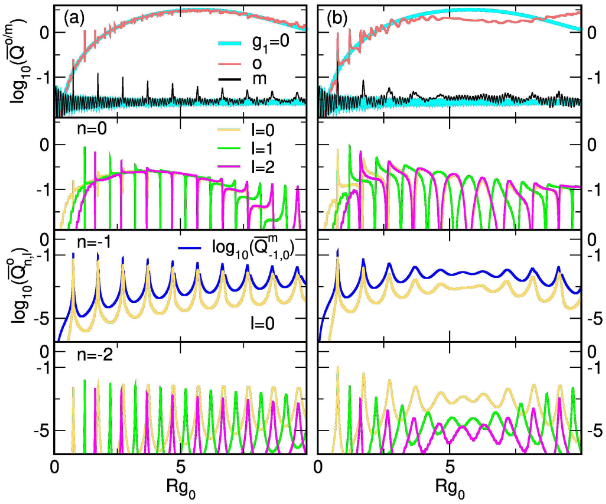

FIG. 7. Time-averaged scattering efficiency (top panel) of the photon [red (gray)] and the phonon (black) and optical scattering contributions of different partial waves (lower panels) at weak couplings, where $|g_1| = 5\times10^{-3}\Omega$ in (a) and $|g_1| = 0.02\Omega$ in (b). In the top panels the scattering efficiencies of the static dot are included [turquoise (thicker) line]. The scattering contribution of the phonon for the sideband $n=-1$ with $l=0$ is denoted by the blue line. To realize a symmetric Floquet resonance at $E \simeq \Omega$ [case (2) in Fig. 3], we choose $E = 10^{-3}g_0 + \Omega$, $g_0 = \Omega\sqrt{v_o v_m}/(v_o + v_m) \simeq 0.287\Omega$.

have the same helicity). A detailed analytical and numerical analysis of a suchlike extended (much more complicated) scattering problem is beyond the scope of the present work and is therefore postponed to a forthcoming study.

2. Symmetric Floquet-resonant scattering close by $E \simeq \Omega$

Next we investigate the scattering of a photon with energy $E \simeq \Omega$, according to case (2) in Fig. 3. Since the energy-coupling ratio $E/g_0 \simeq 3.48$, the static quantum dot now acts as a weak reflector with almost no light-sound interconversion [regime (iii) in Fig. 2]. As before, the scattering by the oscillating dot is Floquet-resonant and the situation is, in some sense, symmetric as the energies with $n = 0, -1, -2$ match the CE perfectly and the wave numbers obtained from $E_{\pm n}$ have equal magnitudes. Since $E \neq 0$ the sideband contributions are no longer symmetric with respect to $n \to -n$.

In Fig. 7 the time-averaged scattering efficiency of the photon and the phonon is depicted together with the scattering contributions of the photon for two (weak) couplings ($2|g_1| \ll \Omega$). The scattering is determined by the central band and the sidebands $n = -1, -2$; other sidebands play no role as their energies do not lie in the range of the CE (cf. Fig. 3). For the mechanical mode only the $n = -1$ contribution is shown because this is the only one that modifies the scattering efficiency substantially. Note that the size parameter ER takes on large values very quickly, which is why exclusively the contributions of the first partial waves were considered.

While the scattering efficiency essentially follows those of the static dot, it features some very sharp resonances [see Fig. 7(a)]. The central band contribution $n = 0$ indicates that

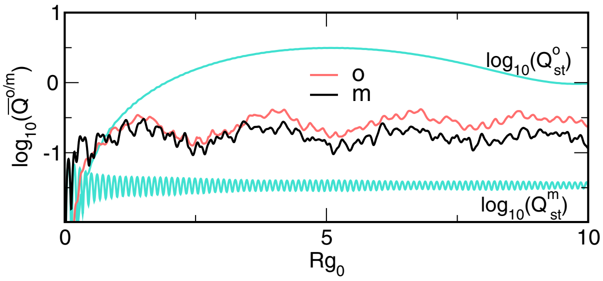

FIG. 8. Time-averaged scattering efficiency of the photon [red (gray)] and the phonon (black) slightly away from the symmetric Floquet resonance at $E = 0.928\Omega$, $g_0 = 0.3\Omega$, and $|g_1| = 0.1\Omega$. For comparison, the corresponding scattering efficiencies of the static dot are shown (turquoise).

these spikes originate from resonances of the partial waves (15) as they will also occur for a static quantum dot at zero photon energy in the resonant scattering regime. Not surprisingly, the resonant scattering regime is also reflected in the sideband contribution $n = -1$, where the effective energy-coupling ratio $E_{n=-1}/g_0 \simeq 0$. Here, only the lowest partial wave $l = 0$ is resonant, while higher partial waves are not excited due to the smallness of the effective size parameter, $E_{n=-1}R \ll 1$. The situation changes for the sideband $n = -2$, where the effective size parameter becomes large again, $E_{n=-2}R \gg 1$.

Increasing the coupling strength in the weak-coupling regime, the resonances broaden [compare Figs. 7(b) and 7(a)], and especially the low-frequency part in the functional dependence of $\overline{Q}(Rg_0)$ markedly deviates from that of the static dot. Both effects can be attributed to larger deviations of the Floquet wave numbers from those of the static problem when g_1 is growing. Again off-resonances occur, which becomes particularly clear for the $n = -1$ sideband contribution [see Fig. 7(b)]. This signal is very similar to that one obtained in Fig. 4(b), where the same value of g_1 was used. The reason is that the effective energy-coupling ratio of the sideband is equal to that of a photon with energy at the neutrality point, $E_{n=-1}/g_0 \simeq 0$. This means that not only for $E \simeq 0$ but also for $E \simeq \Omega$ the interplay between sideband and central band excitations causes a partial transition from the weak reflector regime to the resonant scattering regime [from (iii) to (i) in Fig. 2], leading to the formation of a photon-dominated weak resonant scattering regime.

The scattering efficiency at moderate coupling strengths, slightly away from the symmetric Floquet resonance condition, reveals another interesting result. Figure 8 shows that in this case the scattering is no longer photon dominated (different from Fig. 7). So while the static dot acts as a weak reflector for photons with almost no light-sound interconversion, the scattering efficiency of the phonon now becomes comparable with that in the weak scattering regime.

3. Floquet-resonant scattering without symmetry

Finally, we discuss the scattering by the oscillating quantum dot for a situation without symmetry. For that we assume $E \simeq 0.12\Omega$ and $g_0 \simeq 0.39\Omega$, according to case (3) in Fig. 3.

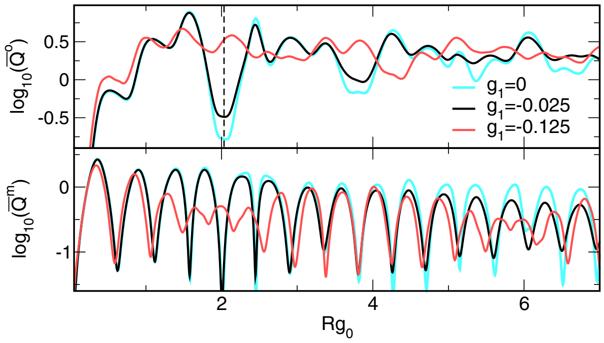

FIG. 9. Time-averaged scattering efficiency at Floquet resonance without symmetry [case (3) in Fig. 3]. Here $E \simeq 0.12\Omega$ and $g_0 \simeq 0.39\Omega$.

Then the energy-coupling ratio $E/g_0 \simeq 0.31$, and the static dot acts as a strong reflector with angle-dependent light-sound interconversion [regime (ii) in Fig. 2]. The scattering is again Floquet-resonant.

Figure 9 displays the time-averaged scattering efficiency of the photon and the phonon for weak and moderate coupling strength. Since the size parameter $ER \simeq 1$, the scattering efficiency of the static dot features resonances of the first partial waves, showing up as broad peaks. The oscillating dot weakens the resonances in the scattering efficiency of the photon as well as the light-sound interconversion rate. This effect becomes more pronounced at higher coupling strengths, and is accompanied by off-resonances for the phonon.

Figure 10(a) gives the (relevant) photon contributions to the scattering efficiency at weak coupling. The phononic contributions are not shown because the phonon scattering efficiency is determined by the central band only. The sideband $n = -1$ has a significant influence on the scattering efficiency as $E_{n=-1}$ matches the CE (cf. Fig. 3). Since the corresponding effective energy-coupling ratio $|E_{n=-1}|/g_0 \simeq 2.3$, the interference of states of the sideband and the central band leads to the hybridization of the weak and the strong reflector regime of the static dot [regimes (iii) and (ii) in Fig. 2], which gives the explanation for the weakening of resonances and of the light-sound interconversion rate in Fig. 9. We further observe, that only the first partial waves are excited for the sideband, although the effective size parameter is significantly larger, $|E_{n=-1}|R > E_{n=0}R$. The same effect occurs for the case of symmetric Floquet-resonant scattering at $E \simeq 0$ in

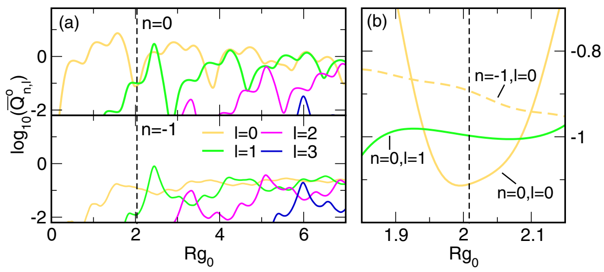

FIG. 10. (a) Scattering contributions to $\overline{Q}^o$ given in Fig. 9 for $|g_1| = 0.025\Omega$. (b) Enlarged area near $Rg_0 = 2$.

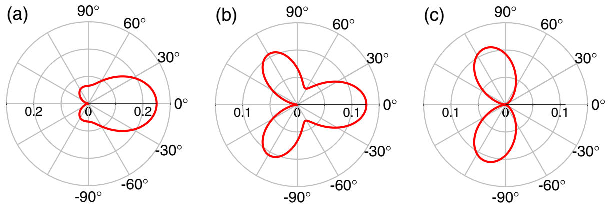

FIG. 11. Polar plot of the current density of the optical reflected wave in the far field according to Eq. (14) at the time $t/2\pi = 0.61$ (a), $t/2\pi = 1.2$ (b), and $t/2\pi = 1.33$ (c) for $r = R$. Parameter values are the same as in Fig. 10 with $Rg_0 \simeq 2$ (dashed line).

Fig. 4. It seems that the size parameter ER determines the maximum number of partial waves $l^{\max}$ which are involved in the scattering, whereas the effective size parameter $E_{n\neq 0}R$ determines the maximum number of partial waves for the sidebands with the constraint $l^{\max}_{n\neq 0} \leqslant l^{\max}$ (this applies also to the Floquet scattering problem in graphene [40]). This is reasonable, since the scattered waves with their effective size parameters merely represent the system's response, whereas the incident wave and its interaction with the quantum dot represent the initial condition of scattering.

Figure 10(b) enlarges the area of Fig. 10(a) where the scattering contributions of different angular momentum l and different energy n are of comparable magnitude. While the angular momentum defines the angle dependence of the radiation, the energy determines their time dependence [cf. Eq. (14)]. Interference has a lasting effect on the (angle- and time-dependent) radiation characteristics. This is illustrated in Fig. 11. At different points in time the interference causes either (a) forward scattering due to the $l = 0$ mode, (b) scattering in several directions due to the $l = 1$ mode, or (c) the absence of forward scattering (Fano resonance) due to the interference of the $l = 0$ and $l = 1$ modes [33]. In this way, the oscillating quantum dot might act as a time-dependent photon transistor.

IV. CONCLUSIONS

The main goal of this work was to examine the time-dependent scattering of twofold degenerate Dirac-Weyl quasiparticles by laser-driven quantum dots in optomechanical graphene. The setup considered models the propagation and interconversion of light and sound on a honeycomb array of optomechanical cells, structured by circular, oscillating (photon-phonon-coupling) barriers.

As our investigations have shown, the temporal modulation (Ω) of the photon-phonon coupling in the quantum dot region (R) tremendously influences the quasiparticle transport. Here, unlike the energy-conserving case of a static quantum dot where the scattering is essentially determined by the ratio between the energy of the incident photon wave and the coupling strength of the barrier, inelastic scattering gives rise to the excitation of sideband states with energies $E_n = E + n\hbar\Omega$. Their interference causes a mixing of long-wavelength (quantum) and short-wavelength (quasiclassical) regimes. The number of sidebands involved is greater the larger (smaller) the amplitude (frequency) of the barrier oscillation. This affects also the effective size parameters $E_n R$, which determine the angular momentum contributions involved in the scattering process. The consequence is a time-periodic, strongly angle-dependent emission of light and sound (with Fano resonances), analogous to electron transport through driven graphene quantum dots. In this way, the optomechanical quantum dot acts as a time-dependent converter for photons and phonons.

Analyzing the underlying, effective two-level system within Floquet theory, it was shown that avoided crossings in the quasienergy band structure are of particular importance. More specifically, when the (sideband) energy lies in the vicinity of an avoided crossing (Floquet resonance), the influence of the barrier is most prominent since the wave numbers determining the scattering process most deviate from those of the static dot. Then even a small oscillation amplitude may significantly affect the scattering, up to the point where the light-sound interconversion is suppressed and revived in the course of interference of waves with different wave numbers.

The results presented in this work should have impact on both fundamental problems such as the observation of *zitterbewegung* and potential applications based on quantum-optical, laser-driven optomechanical metamaterials being suitable for the transport, storage, and transduction of photons and phonons. In this context, a more realistic description of optomechanical systems beyond the continuum approximation, which ideally involves wave-packet dynamics and dissipation, is highly desirable, as well as more in-depth studies about the role of time-dependent (synthetically generated) magnetic fields [31].

ACKNOWLEDGMENT

The authors would like to thank K. Rasek for valuable discussions.

APPENDIX: IMPLEMENTATION OF THE FLOQUET APPROACH

Inserting the Floquet state (3) into the time-dependent Dirac equation yields the Floquet eigenvalue equation:

$$\sum_p \sum_{\tau=\pm} \Big\{ c_p^\tau \big(E^{\tau,\sigma} + p\Omega\big) |\tau\rangle\, \delta_{pp'} + g_1 \sum_{\tau'=\pm} c_p^\tau \alpha_{\tau'}^\tau\, |\tau'\rangle \left(\delta_{p+1,p'} + \delta_{p-1,p'}\right) \Big\} = \varepsilon \sum_p \sum_{\tau=\pm} c_p^\tau\, |\tau\rangle\, \delta_{pp'}, \quad p' \in \mathbb{Z}, \tag{A1}$$

where

$$E^\tau = \overline{v}\sigma q + \sigma\tau \sqrt{g_0^2 + \delta v^2 q^2/4} \tag{A2}$$

is the energy dispersion of the time-independent problem for wave number q, and

$$\alpha_+^\tau = \frac{\mathcal{N}^\tau}{\mathcal{N}^+} \frac{g_0^2 - \gamma^\tau\gamma^+}{g_0(\gamma^+ - \gamma^-)} = -\tau\alpha_-^{-\tau}, \tag{A3}$$

with the normalization factor,

$$\mathcal{N}^\tau = 1/\sqrt{g_0^2 + (\gamma^\tau)^2}, \quad \gamma^\tau = v_o\sigma q - E^\tau. \tag{A4}$$

Based on Eq. (A1) we define the vector of Fourier components, $\boldsymbol{c} = (\dots, c_{-1}^+, c_{-1}^-, c_0^+, c_0^-, c_1^+, c_1^-, \dots)^{\mathrm{T}}$, and the (Hermitian) Floquet matrix,

$$\mathcal{F} = \begin{pmatrix} \ddots & & & & & & & \\ & E_{-1}^+ & 0 & g_1\alpha_+^+ & g_1\alpha_+^- & 0 & 0 & \\ & 0 & E_{-1}^- & g_1\alpha_-^+ & g_1\alpha_-^- & 0 & 0 & \\ & g_1\alpha_+^+ & g_1\alpha_+^- & E^+ & 0 & g_1\alpha_+^+ & g_1\alpha_+^- & \\ & g_1\alpha_-^+ & g_1\alpha_-^- & 0 & E^- & g_1\alpha_-^+ & g_1\alpha_-^- & \\ & 0 & 0 & g_1\alpha_+^+ & g_1\alpha_+^- & E_{+1}^+ & 0 & \\ & 0 & 0 & g_1\alpha_-^+ & g_1\alpha_-^- & 0 & E_{+1}^- & \\ & & & & & & & \ddots \end{pmatrix}, \tag{A5}$$

for $E_n^\tau = E^\tau + n\Omega$. We fix $\Omega = 1$, which is justified due to the scale invariance of the scattering problem. The quasienergies ε in $\mathcal{F}\boldsymbol{c} = \varepsilon\boldsymbol{c}$ are obtained as the eigenvalues of the Floquet matrix (A5) and depend on the two barrier parameters g_0, g_1, as well as on wave number q. The pseudospin projection $\sigma = \pm 1$ leads only to a change in the sign of the quasienergies and is determined by the sign of the wave number. As a consequence of the polariton degree of freedom $\tau = \pm 1$, the static dispersion (A2) is twofold degenerate. Accordingly, the quasienergies are twofold degenerate, too, which is reflected in the block-diagonal form of $\mathcal{F}$ and is marked by the index $(\pm)$ hereinafter. Diagonalization yields a pair of quasienergies $\varepsilon^{(\pm)}(q)$ with Fourier vectors $\boldsymbol{c}^{(\pm)}(q)$ for each q. Other pairs of quasienergies $\varepsilon^{(\pm)}(q) + n\Omega$ are also eigensolutions of Eq. (A5), but in principle they all contain the same information about the time dependence.

According to Eq. (6), the eigensolutions of $\mathcal{F}$ are needed to construct the transmitted wave function inside the dot. Since

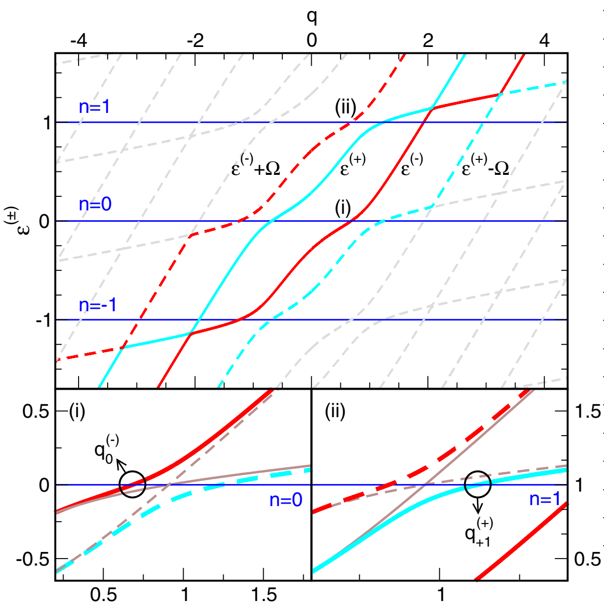

FIG. 12. Quasienergies $\varepsilon^{(\pm)} + n\Omega$, $n \in \mathbb{Z}$, obtained as eigenvalues of the Floquet matrix (A5) for $|g_1| = 0.14\Omega$ as a function of the wave number q (using $\sigma = \pm 1$ for positive and negative values of q). Inserted are also the energies $E_n = E + n\Omega$ of the central band $n = 0$ and the sidebands $n = \pm 1$ (blue horizontal lines) for $E = 0$ and static coupling $g_0 = 0.287\Omega$, corresponding to the case of symmetric Floquet resonance close by $E \simeq 0$ (see discussion in Sec. III B 1 of the main text). The proper pair of quasienergies $\varepsilon^{(\pm)}$ (solid lines) that has to be used for the scattering problem is that which coincides with the dispersion of the static case at $q \to 0$. The wave numbers used for the scattering problem are determined by the zeros of $E_n - \varepsilon^{(\pm)}(q)$ and are marked exemplary for the cases $n = 0, 1$ in the lower panels (i) and (ii). For comparison the polariton branches of the energy dispersion of the static case, $E^{\mp}(q)$ (solid) and $E^{\pm}(q) \mp \Omega$ (dashed), are shown (brown thin lines). Since $E = 0$, the wave numbers reveal the symmetry $q_{-n}^{(\pm)} = -q_n^{(\mp)}$.

the oscillating barrier shifts the energy E of the incoming wave, $E_n = E + n\Omega$, the quasienergies are fixed: $\varepsilon^{(\pm)}(q) = E_n$. The zeros of $\varepsilon^{(\pm)}(q) - E_n$ yield the wave numbers $q_n^{(\pm)}$, and hence the Fourier vectors $\boldsymbol{c}_n^{(\pm)}$ can be calculated. Doing this it makes sense to connect the considered pair of quasienergies with the energy dispersion in the static case for $q \to 0$: $\varepsilon^{(\pm)}(q \to 0) = E^{\pm}(q \to 0)$. We note that when using the Floquet approach the specific geometry of the barrier only enters the scattering matrix via Eqs. (8) and (9) (e.g., the results for a planar barrier are given in [45]).

Figure 12 dislays the highly symmetric situation that evolves in the numerical work for the Floquet resonance at photon energy $E \simeq 0$ discussed in the main text. By tracking the quasienergies in dependence of q, the condition $\varepsilon^{(\pm)}(q) = E_n$ defines the wave numbers $q_n^{(\pm)}$ (and Fourier vectors) that have to be used for the barrier wave function (crossings of the blue horizontal lines with the quasienergies); see panels (i) and (ii) for $n = 0, 1$. Deviations of the wave numbers q from those of the dispersion of the static case (obtained from crossings of the horizontal lines with the brown thin lines in lower panels of Fig. 12) arise due to the avoided crossings. Obviously, these deviations are largest in the vicinity of the points where the two polariton branches of the static dispersion cross each other. The corresponding crossing energies are given by Eq. (16). Of course, the influence of the oscillating barrier on the scattering is most prominent for energies E_n near a crossing energy. There even small couplings $|g_1| \ll \Omega$ significantly modify the scattering (cf. Figs. 3, 6, and 8).

We finally note that at larger $|q|$ values the quasienergies are less affected by the barrier; for $|q| \gg 1$ the quasienergy and the dispersion of free quasiparticles merge. This can be used to implement truncation criteria for the number of sidebands $n_{\max}$ which will have to be considered in the numerical work. Taking into account that $2|g_1| \leqslant g_0$, we found that $\dim\mathcal{F} \simeq 2 + 4(x - 1)$ with $x = 2(1 + 10 \times 4|g_1|)$ serves as a good estimate for numerical convergence of the quasienergies $\varepsilon^{(\pm)}$ as well as for those of the scattering coefficients. Then the maximum number of sidebands used in the numerics should be at least $n_{\max} = x/2$, i.e., $n_{\max} \simeq 1 + 10 \times 4|g_1|$.

[1] M. Aspelmeyer, T. J. Kippenberg, and F. Marquardt, Rev. Mod. Phys. **86**, 1391 (2014).
[2] J. Chan, T. P. M. Alegre, A. H. Safavi-Naeini, J. T. Hill, A. Krause, S. Gröblacher, M. Aspelmeyer, and O. Painter, Nature (London) **478**, 89 (2011).
[3] J. D. Teufel, T. Donner, D. Li, J. W. Harlow, M. S. Allman, K. Cicak, A. J. Sirois, J. D. Whittaker, K. W. Lehnert, and R. W. Simmonds, Nature (London) **475**, 359 (2011).
[4] M. Frimmer, J. Gieseler, and L. Novotny, Phys. Rev. Lett. **117**, 163601 (2016).
[5] F. Marquardt, J. G. E. Harris, and S. M. Girvin, Phys. Rev. Lett. **96**, 103901 (2006).
[6] C. Wurl, A. Alvermann, and H. Fehske, Phys. Rev. A **94**, 063860 (2016).
[7] L. Bakemeier, A. Alvermann, and H. Fehske, Phys. Rev. Lett. **114**, 013601 (2015).
[8] J. Qian, A. A. Clerk, K. Hammerer, and F. Marquardt, Phys. Rev. Lett. **109**, 253601 (2012).
[9] C. Schulz, A. Alvermann, L. Bakemeier, and H. Fehske, Europhys. Lett. **113**, 64002 (2016).
[10] D. Vitali, S. Gigan, A. Ferreira, H. R. Böhm, P. Tombesi, A. Guerreiro, V. Vedral, A. Zeilinger, and M. Aspelmeyer, Phys. Rev. Lett. **98**, 030405 (2007).
[11] R. Ghobadi, S. Kumar, B. Pepper, D. Bouwmeester, A. I. Lvovsky, and C. Simon, Phys. Rev. Lett. **112**, 080503 (2014).
[12] Y.-D. Wang and A. A. Clerk, Phys. Rev. Lett. **108**, 153603 (2012).
[13] J. T. Hill, A. H. Safavi-Naeini, J. Chan, and O. Painter, Nat. Commun. **3**, 1196 (2012).
[14] T. A. Palomaki, J. W. Harlow, J. D. Teufel, R. W. Simmonds, and K. W. Lehnert, Nature (London) **495**, 210 (2013).
[15] M. J. Weaver, F. Buters, F. Luna, H. Eerkens, K. Heeck, S. de Man, and D. Bouwmeester, Nat. Commun. **8**, 824 (2017).

[16] M. Eichenfield, J. Chan, R. M. Camacho, K. J. Vahala, and O. Painter, Nature (London) **462**, 78 (2009).
[17] A. H. Safavi-Naeini and O. Painter, Opt. Express **18**, 14926 (2010).
[18] A. H. Safavi-Naeini, T. P. M. Alegre, M. Winger, and O. Painter, Appl. Phys. Lett. **97**, 181106 (2010).
[19] A. H. Safavi-Naeini, J. T. Hill, S. Meenehan, J. Chan, S. Gröblacher, and O. Painter, Phys. Rev. Lett. **112**, 153603 (2014).
[20] G. Heinrich, M. Ludwig, J. Qian, B. Kubala, and F. Marquardt, Phys. Rev. Lett. **107**, 043603 (2011).
[21] A. Xuereb, C. Genes, and A. Dantan, Phys. Rev. Lett. **109**, 223601 (2012).
[22] M. Ludwig and F. Marquardt, Phys. Rev. Lett. **111**, 073603 (2013).
[23] D. E. Chang, A. H. Safavi-Naeini, M. Hafezi, and O. Painter, New J. Phys. **13**, 023003 (2011).
[24] A. H. Safavi-Naeini and O. Painter, New J. Phys. **13**, 013017 (2011).
[25] M. Schmidt, M. Ludwig, and F. Marquardt, New J. Phys. **14**, 125005 (2012).
[26] W. Chen and A. A. Clerk, Phys. Rev. A **89**, 033854 (2014).
[27] K. Fang, M. H. Matheny, X. Luan, and O. Painter, Nat. Photon. **10**, 489 (2016).
[28] M. Schmidt, S. Kessler, V. Peano, O. Painter, and F. Marquardt, Optica **2**, 635 (2015).
[29] S. Walter and F. Marquardt, New J. Phys. **18**, 113029 (2016).
[30] M. Aidelsburger, S. Nascimbene, and N. Goldman, C. R. Phys. **19**, 394 (2018).
[31] V. Peano, C. Brendel, M. Schmidt, and F. Marquardt, Phys. Rev. X **5**, 031011 (2015).
[32] M. Schmidt, V. Peano, and F. Marquardt, New J. Phys. **17**, 023025 (2015).
[33] C. Wurl and H. Fehske, Sci. Rep. **7**, 9811 (2017).
[34] G. Platero and R. Aguado, Phys. Rep. **395**, 1 (2004).
[35] M. V. Fistul and K. B. Efetov, Phys. Rev. Lett. **98**, 256803 (2007).
[36] M. A. Zeb, K. Sabeeh, and M. Tahir, Phys. Rev. B **78**, 165420 (2008).
[37] W.-T. Lu, S.-J. Wang, W. Li, Y.-L. Wang, C.-Z. Ye, and H. Jiang, J. Appl. Phys. **111**, 103717 (2012).
[38] C. Sinha and R. Biswas, Appl. Phys. Lett. **100**, 183107 (2012).
[39] R. Biswas and C. Sinha, J. Appl. Phys. **114**, 183706 (2013).
[40] C. Schulz, R. L. Heinisch, and H. Fehske, Phys. Rev. B **91**, 045130 (2015).
[41] B. Trauzettel, Y. M. Blanter, and A. F. Morpurgo, Phys. Rev. B **75**, 035305 (2007).
[42] J. H. Shirley, Phys. Rev. **138**, B979 (1965).
[43] S.-K. Son, S. Han, and Shih-I. Chu, Phys. Rev. A **79**, 032301 (2009).
[44] T. Bilitewski and N. R. Cooper, Phys. Rev. A **91**, 033601 (2015).
[45] C. Wurl and H. Fehske, arXiv:1811.11604.
[46] P. Rakich and F. Marquardt, New J. Phys. **20**, 045005 (2018).
[47] M. Grifoni and P. Hänggi, Phys. Rep. **304**, 229 (1998).
[48] S.-I. Chu and D. A. Telnov, Phys. Rep. **390**, 1 (2004).
[49] C. Deng, F. Shen, S. Ashhab, and A. Lupascu, Phys. Rev. A **94**, 032323 (2016).
[50] G. Floquet, Ann. Scient. Ec. Norm. Sup. **12**, 47 (1883).
[51] R. L. Heinisch, F. X. Bronold, and H. Fehske, Phys. Rev. B **87**, 155409 (2013).
[52] C. Schulz, R. L. Heinisch, and H. Fehske, Quantum Matter **4**, 346 (2015).
[53] J.-S. Wu and M. M. Fogler, Phys. Rev. B **90**, 235402 (2014).
[54] M. I. Katsnelson, Eur. Phys. J. B **51**, 157 (2006).
[55] J. C. Martinez, M. B. A. Jalil, and S. G. Tan, Appl. Phys. Lett. **97**, 062111 (2010).
[56] W. Zawadzki and T. M. Rusin, J. Phys.: Condens. Matter **23**, 143201 (2011).
[57] T. García, N. A. Cordero, and E. Romera, Phys. Rev. B **89**, 075416 (2014).

Bibliography

[1] M. Aspelmeyer, T. J. Kippenberg, and F. Marquardt, *Rev. Mod. Phys.* **86**, 1391 (2014).

[2] C. K. Law, *Phys. Rev. A* **51**, 2537 (1995).

[3] H. K. Cheung and C. K. Law, *Phys. Rev. A* **84**, 023812 (2011).

[4] T. J. Kippenberg and K. J. Vahala, *Science* **321**, 1172 (2008).

[5] I. C. Percival, *Journal of Physics A: Mathematical and General* **27**, 1003 (1994).

[6] M. Rigo and N. Gisin, *Quantum and Semiclassical Optics: Journal of the European Optical Society Part B* **8**, 255 (1996).

[7] I. C. Percival and W. T. Strunz, *Journal of Physics A: Mathematical and General* **31**, 1815 (1998).

[8] C. W. Gardiner and P. Zoller, *Quantum Noise*, Springer, Berlin, 2004.

[9] F. Marquardt and S. M. Girvin, *Physics* **2**, 40 (2009).

[10] P. Meystre, *Annalen der Physik* **525**, 215 (2012).

[11] J. B. Hertzberg, T. Rocheleau, T. Ndukum, M. Savva, A. A. Clerk, and K. C. Schwab, *Nature Physics* **6**, 213 (2009).

[12] M. R. Vanner, J. Hofer, G. D. Cole, and M. Aspelmeyer, *Nature Communications* **4**, 2295 (2013).

[13] J. Suh, A. J. Weinstein, C. U. Lei, E. E. Wollman, S. K. Steinke, P. Meystre, A. A. Clerk, and K. C. Schwab, *Science* **344**, 1262 (2014).

[14] J. Chan, T. P. M. Alegre, A. H. Safavi-Naeini, J. T. Hill, A. Krause, S. Grblacher, M. Aspelmeyer, and O. Painter, *Nature* **478**, 89 (2011).

[15] J. D. Teufel, T. Donner, D. Li, J. W. Harlow, M. S. Allman, K. Cicak, A. J. Sirois, J. D. Whittaker, K. W. Lehnert, and R. W. Simmonds, *Nature* **475**, 359 (2011).

[16] M. Frimmer, J. Gieseler, and L. Novotny, *Phys. Rev. Lett.* **117**, 163601 (2016).

[17] D. Vitali, S. Gigan, A. Ferreira, H. R. Böhm, P. Tombesi, A. Guerreiro, V. Vedral, A. Zeilinger, and M. Aspelmeyer, *Phys. Rev. Lett.* **98**, 030405 (2007).

[18] M. Ludwig, K. Hammerer, and F. Marquardt, *Phys. Rev. A* **82**, 012333 (2010).

[19] R. Ghobadi, S. Kumar, B. Pepper, D. Bouwmeester, A. I. Lvovsky, and C. Simon, *Phys. Rev. Lett.* **112**, 080503 (2014).

[20] D. W. C. Brooks, T. Botter, S. Schreppler, T. P. Purdy, N. Brahms, and D. M. Stamper-Kurn, *Nature* **488**, 476 (2012).

[21] A. H. Safavi-Naeini, S. Grblacher, J. T. Hill, J. Chan, M. Aspelmeyer, and O. Painter, *Nature* **500**, 185 (2013).

[22] T. P. Purdy, P.-L. Yu, R. W. Peterson, N. S. Kampel, and C. A. Regal, *Phys. Rev. X* **3**, 031012 (2013).

[23] M. Asjad and D. Vitali, *Journal of Physics B: Atomic, Molecular and Optical Physics* **47**, 045502 (2014).

[24] T.-S. Yin, X.-Y. Lü, L.-L. Zheng, M. Wang, S. Li, and Y. Wu, *Phys. Rev. A* **95**, 053861 (2017).

[25] H. Rokhsari, T. J. Kippenberg, T. Carmon, and K. J. Vahala, *Opt. Express* **13**, 5293 (2005).

[26] T. J. Kippenberg, H. Rokhsari, T. Carmon, A. Scherer, and K. J. Vahala, *Phys. Rev. Lett.* **95**, 033901 (2005).

[27] T. Carmon, H. Rokhsari, L. Yang, T. J. Kippenberg, and K. J. Vahala, *Phys. Rev. Lett.* **94**, 223902 (2005).

[28] F. Marquardt, J. G. E. Harris, and S. M. Girvin, *Phys. Rev. Lett.* **96**, 103901 (2006).

[29] T. Carmon, M. C. Cross, and K. J. Vahala, *Phys. Rev. Lett.* **98**, 167203 (2007).

[30] M. Ludwig, B. Kubala, and F. Marquardt, *New Journal of Physics* **10**, 095013 (2008).

[31] J. Qian, A. A. Clerk, K. Hammerer, and F. Marquardt, *Phys. Rev. Lett.* **109**, 253601 (2012).

[32] L. Bakemeier, A. Alvermann, and H. Fehske, *Phys. Rev. Lett.* **114**, 013601 (2015).

[33] G. Heinrich, J. G. E. Harris, and F. Marquardt, *Phys. Rev. A* **81**, 011801 (2010).

[34] J. Larson and M. Horsdal, *Phys. Rev. A* **84**, 021804 (2011).

[35] H. Wu, G. Heinrich, and F. Marquardt, *New Journal of Physics* **15**, 123022 (2013).

[36] J. Mumford, D. H. J. O'Dell, and J. Larson, *Annalen der Physik* **527**, 115 (2015).

[37] X.-Y. Lü, H. Jing, J.-Y. Ma, and Y. Wu, *Phys. Rev. Lett.* **114**, 253601 (2015).

[38] J. Ruiz-Rivas, C. Navarrete-Benlloch, G. Patera, E. Roldán, and G. J. de Valcárcel, *Phys. Rev. A* **93**, 033850 (2016).

[39] H. Xu, U. Kemiktarak, J. Fan, S. Ragole, J. Lawall, and J. M. Taylor, *Nature Communications* **8**, 14481 (2017).

[40] Y.-D. Wang and A. A. Clerk, *Phys. Rev. Lett.* **108**, 153603 (2012).

[41] L. Tian, *Phys. Rev. Lett.* **108**, 153604 (2012).

[42] X. Zhou, F. Hocke, A. Schliesser, A. Marx, H. Huebl, R. Gross, and T. J. Kippenberg, *Nature Physics* **9**, 179 (2013).

[43] T. A. Palomaki, J. W. Harlow, J. D. Teufel, R. W. Simmonds, and K. W. Lehnert, *Nature* **495**, 210 (2013).

[44] R. Riedinger, S. Hong, R. A. Norte, J. A. Slater, J. Shang, A. G. Krause, V. Anant, M. Aspelmeyer, and S. Gröblacher, *Nature* **530**, 313 (2016).

[45] M. Eichenfield, J. Chan, R. M. Camacho, K. J. Vahala, and O. Painter, *Nature* **462**, 78 (2009).

[46] A. H. Safavi-Naeini and O. Painter, *Opt. Express* **18**, 14926 (2010).

[47] A. H. Safavi-Naeini, T. P. M. Alegre, M. Winger, and O. Painter, *Applied Physics Letters* **97**, 181106 (2010).

[48] A. H. Safavi-Naeini, J. T. Hill, S. Meenehan, J. Chan, S. Gröblacher, and O. Painter, *Phys. Rev. Lett.* **112**, 153603 (2014).

[49] J. T. Hill, A. H. Safavi-Naeini, J. Chan, and O. Painter, *Nature Communications* **3**, 1196 (2012).

[50] M. Bhattacharya, H. Uys, and P. Meystre, *Phys. Rev. A* **77**, 033819 (2008).

[51] A. H. Safavi-Naeini and O. Painter, *New Journal of Physics* **13**, 013017 (2011).

[52] D. E. Chang, A. H. Safavi-Naeini, M. Hafezi, and O. Painter, *New Journal of Physics* **13**, 023003 (2011).

[53] G. Heinrich, M. Ludwig, J. Qian, B. Kubala, and F. Marquardt, *Phys. Rev. Lett.* **107**, 043603 (2011).

[54] M. Schmidt, M. Ludwig, and F. Marquardt, *New Journal of Physics* **14**, 125005 (2012).

[55] A. Xuereb, C. Genes, and A. Dantan, *Phys. Rev. Lett.* **109**, 223601 (2012).

[56] M. Ludwig and F. Marquardt, *Phys. Rev. Lett.* **111**, 073603 (2013).

[57] W. Chen and A. A. Clerk, *Phys. Rev. A* **89**, 033854 (2014).

[58] M. Zhang, S. Shah, J. Cardenas, and M. Lipson, *Phys. Rev. Lett.* **115**, 163902 (2015).

[59] K. Fang, M. H. Matheny, X. Luan, and O. Painter, *Nature Photonics* **10**, 489 (2016).

[60] M. J. Weaver, F. Buters, F. Luna, H. Eerkens, K. Heeck, S. de Man, and D. Bouwmeester, *Nature Communications* **8**, 824 (2017).

[61] M. Schmidt, S. Kessler, V. Peano, O. Painter, and F. Marquardt, *Optica* **2**, 635 (2015).

[62] S. Walter and F. Marquardt, *New Journal of Physics* **18**, 113029 (2016).

[63] M. Aidelsburger, S. Nascimbene, and N. Goldman, *arXiv:1710.00851v1 [cond-mat.mes-hall]* (2017).

[64] V. Peano, C. Brendel, M. Schmidt, and F. Marquardt, *Phys. Rev. X* **5**, 031011 (2015).

[65] M. Schmidt, V. Peano, and F. Marquardt, *New Journal of Physics* **17**, 023025 (2015).

[66] G. Platero and R. Aguado, *Physics Reports* **395**, 1 (2004).

[67] M. I. Katsnelson, *EPJB* **51**, 157 (2006).

[68] B. Trauzettel, Y. M. Blanter, and A. F. Morpurgo, *Phys. Rev. B* **75**, 035305 (2007).

[69] J. C. Martinez, M. B. A. Jalil, and S. G. Tan, *Applied Physics Letters* **97**, 062111 (2010).

[70] W. Zawadzki and T. M. Rusin, *Journal of Physics: Condensed Matter* **23**, 143201 (2011).

[71] T. García, N. A. Cordero, and E. Romera, *Phys. Rev. B* **89**, 075416 (2014).

[72] R. L. Heinisch, F. X. Bronold, and H. Fehske, *Phys. Rev. B* **87**, 155409 (2013).

[73] J.-S. Wu and M. M. Fogler, *Phys. Rev. B* **90**, 235402 (2014).

[74] C. Schulz, R. L. Heinisch, and H. Fehske, *Quantum Matter* **4**, 346 (2015).

[75] C. Schulz, R. L. Heinisch, and H. Fehske, *Phys. Rev. B* **91**, 045130 (2015).

[76] M. V. Fistul and K. B. Efetov, *Phys. Rev. Lett.* **98**, 256803 (2007).

[77] M. A. Zeb, K. Sabeeh, and M. Tahir, *Phys. Rev. B* **78**, 165420 (2008).

[78] W.-T. Lu, S.-J. Wang, W. Li, Y.-L. Wang, C.-Z. Ye, and H. Jiang, *Journal of Applied Physics* **111**, 103717 (2012).

[79] C. Sinha and R. Biswas, *Applied Physics Letters* **100**, 183107 (2012).

[80] R. Biswas and C. Sinha, *Journal of Applied Physics* **114**, 183706 (2013).

[81] A. M. Jayich, J. C. Sankey, B. M. Zwickl, C. Yang, J. D. Thompson, S. M. Girvin, A. A. Clerk, F. Marquardt, and J. G. E. Harris, *New Journal of Physics* **10**, 095008 (2008).

[82] M. Ludwig, A. H. Safavi-Naeini, O. Painter, and F. Marquardt, *Phys. Rev. Lett.* **109**, 063601 (2012).

[83] J. D. Thompson, B. M. Zwickl, A. M. Jayich, F. Marquardt, S. M. Girvin, and J. G. E. Harris, *Nature* **452**, 72 (2008).

[84] H. J. Carmichael, *Statistical Methods in Quantum Optics 1*, Springer, 1999.

[85] P. Ehrenfest, *Z. Physik* **45**, 455 (1927).

[86] N. Gisin and I. C. Percival, *Journal of Physics A: Mathematical and General* **25**, 5677 (1992).

[87] R. Schack, T. A. Brun, and I. C. Percival, *Journal of Physics A: Mathematical and General* **28**, 5401 (1995).

[88] R. Schack and T. A. Brun, *Computer Physics Communications* **102**, 210 (1997).

[89] W. P. Schleich, *Quantum Optics in Phase Space*, Wiley-VCH, New York, 2001.

[90] W. T. Strunz and I. C. Percival, *Journal of Physics A: Mathematical and General* **31**, 1801 (1998).

[91] P. Rakich and F. Marquardt, *New Journal of Physics* **20**, 045005 (2018).

[92] U. Fano, *Phys. Rev.* **124**, 1866 (1961).

[93] G. Floquet, *Annales scientifiques de l'cole Normale Suprieure* **12**, 47 (1883).

[94] J. H. Shirley, *Phys. Rev.* **138**, B979 (1965).

[95] M. Grifoni and P. Hnggi, *Physics Reports* **304**, 229 (1998).

[96] S.-I. Chu and D. A. Telnov, *Physics Reports* **390**, 1 (2004).

[97] S.-K. Son, S. Han, and S.-I. Chu, *Phys. Rev. A* **79**, 032301 (2009).

[98] T. Bilitewski and N. R. Cooper, *Phys. Rev. A* **91**, 033601 (2015).

[99] C. Deng, F. Shen, S. Ashhab, and A. Lupascu, *Phys. Rev. A* **94**, 032323 (2016).

[100] G. Wang, Y.-C. Lai, and C. Grebogi, *Scientific Reports* **6**, 35381 (2015).

Scientific Contributions

Publications

(a) *Electron flow in circular graphene quantum dots*, C. Schulz, R. L. Heinisch, H. Fehske, *Quantum Matter* **4**, 346 (2015). Copyright (2015) by American Scientific Publishers.

(b) *Scattering of two-dimensional Dirac fermions on gate-defined oscillating quantum dots*, C. Schulz, R. L. Heinisch, and H. Fehske, *Phys. Rev. B* **91**, 045130 (2015). Copyright (2015) by the American Physical Society.

(c) *Optomechanical multistability in the quantum regime*, C. Schulz, A. Alvermann, L. Bakemeier, and H. Fehske, *Europhys. Lett.* **113**, 64002 (2016). Copyright (2016) by EPLA.

(d) *Symmetry-breaking oscillations in membrane optomechanics*, C. Wurl, A. Alvermann, and H. Fehske, *Phys. Rev. A* **94**, 063860 (2016). Copyright (2016) by the American Physical Society.

(e) *Light-sound interconversion in optomechanical Dirac materials*, C. Wurl, and H. Fehske, *Scientific Reports* **7**, 9811 (2017). Open access.

(f) *Transport and Quantum Coherence in Graphene Rings: Aharonov-Bohm Oscillations, Klein Tunneling, and Particle Localization*, A. Filusch, C. Wurl, A. Pieper, and H. Fehske, *Journal of Low Temperature Physics* **191**, 259 (2017). Copyright (2017) by Springer Nature Switzerland AG.

(g) *Time-periodic Klein tunneling through optomechanical Dirac barriers*, C. Wurl, and H. Fehske, *arXiv:1811.11604* (2018). Accepted for publication in *European Journal of Physics: Special Topics* (Proceedings FQMT17).

(h) *Floquet scattering of light and sound in Dirac optomechanics*, C. Wurl and H. Fehske, *arXiv:1809.10043v2* (2018). Accepted for publication in *Phys. Rev. A*.

Conferences and Workshops

(a) *Scattering of two-dimensional Dirac fermions on gate-defined oscillating quantum dots*, C. Schulz, R. L. Heinisch, and H. Fehske, poster at the DPG Spring Meeting, Berlin, 2015

(b) *Nonlinear Dynamics and Quantum Multistability of optomechanical systems*, C. Wurl, A. Alvermann, L. Bakemeier, and H. Fehske, poster at the workshop on 'Quantum Dynamics: From Algorithms to Applications', Greifswald, 2016

(c) *Nonlinear Dynamics and Quantum Multistability of optomechanical systems*, C. Wurl, A. Alvermann, L. Bakemeier, and H. Fehske, poster at the workshop on 'Simulating Quantum Processes and Devices', Bad Honnef, 2016

(d) *Nonlinear Dynamics and Quantum Multistability of optomechanical systems* and *Light-sound interconversion in optomechanical Dirac materials*, C. Wurl, and H. Fehske, posters at the 'Abschlusskolloquium SFB 652', Rostock, 2017

(e) *Light-sound interconversion in optomechanical Dirac materials*, C. Wurl, and H. Fehske, talk at the PhD-seminar, Rostock, 29.06.2017

Acknowledgement

I would like to thank all the people who have supported and encouraged me over the past four years. I extend my gratitude to Prof. Dr. Fehske for his guidance and advice. Also, I would like to thank Dr. Andreas Alvermann for his mentoring in the first two years, and I also thank Dr. Lutz Bakemeier for his feedback on various aspects of this project. Furthermore, many thanks goes to Dr. Bernd Zenker, Mathias Pamperin, Lars Lewerentz, and Kristopher Rasek, who were always understanding and helpful.
However, my biggest thanks goes to my family, especially to my dear wife Marie Wurl, who tirelessly strengthens and supports me, no matter how difficult the situation.